Formation of metallic overlayers on quasicrystal surfaces

Thesis submitted in accordance with the requirements of
the University of Liverpool for the degree of Doctor in Philosophy

by

Lisa Wearing

August 1, 2008

Contents

Acknowledgements

The preparation of this thesis would not have been possible, had it not been for the help and support of many people at the Surface Science Research Center. During this time, I have had the pleasure of working with many exceptional experimentalists including, Dr Julian Ledieu, Dr Lydie Leung and Dr Joe Smerdon. Their dedication gave me the motivation and patience required to work with UHV systems in particular STM. Dr Sam Haq and John Ledward, among others, for the continual help and advice.

During my time at surface science, I have had the fortune of meeting many good friends, whom I'll continue to stay friends with for a good time to come. Thank you for all the great nights out and laughs guys. I'll miss it all.

I would like to thank Prof Ronan McGrath, for the opportunity to undertake my PhD. During which, I have had plenty of travel opportunities and met many great people. Thank you, for all the help and guidance. It has been a pleasure to work with the group.

But most of all, I have to thank my parents and my family, after all without you, none of this would be possible. Thank you for all your help and support and for believing in me. Thank you Mum, for everything, especially all the advice you have given me, including the persistent advice about exams! At the time i didn't appreciate it, though i now know you probably did me a big favour. Thank you Dad, for all the lifts (especially from nights out), it was all part of the learning process! Thank you Shell, for being a great sister. Thank you Christopher, for all the laughs, mostly at my expense. Still, plenty of time to get you back. Thank you Cara and Claire, for being great friends.

At this point I have to mention the influence of my Grandparents, especially that of my Grandad. From spending evenings peering through a telescope to watching documentaries together, his interest in science inspired me to carry on learning.

I must also mention the Complex Metallic Alloy (CMA) network of excellence, who have provided me with many opportunities to attend summer schools, conferences and meetings, during which time I have had the pleasure of meeting

many people and traveling to many places.

Last, but not least, I would like to thank Phil, for all your love and support, its been fun!

Abstract

The main aim of this study is to explore the fundamentals of aperiodicity through the deposition of a single elemental aperiodic overlayer onto a quasicrystal surface. The main difficulty with understanding the effects of aperiodicity on the quasicrystal structure arises due to the chemical complexity associated with the surface, as such structures are only observed in metallic alloys containing two or more elements.

The formation of a single element quasicrystalline structure has been achieved through the deposition of Pb on *i*-Al-Pd-Mn and *d*-Al-Ni-Co (results of the latter not included). This includes an initial study of the effects of aperiodicity on the electronic properties of the surface and the conclusion that the formation of a pseudogap at the Fermi level is due to the aperiodicity of the quasicrystalline structure and not the chemical complexity of the system.

The effects of aperiodicity on the magnetic properties of such a system are not yet known, in particular for a single magnetic species which is ordered aperiodically. For this reason Fe was deposited onto two different quasicrystalline surfaces. They show the formation of such a quasiperiodic magnetic film was not observed, the Fe was in fact aligned periodically along the high symmetry axes of the substrates. This result, along with other work in the same field provides some guidance as to which atoms have the greatest chance of ordering aperiodically.

Most of the research within the field involves thin film deposition in ultra high vacuum. This is a costly technique, and if films on quasicrystal surfaces were one day to be exploited by industry then production would be severely limited. It is for this reason that the electrochemical deposition of Cu onto Al-Pd-Mn has been studied. This work provides the starting point for further study into the electrochemical deposition on to the quasicrystal surface and comparison to those studies in Ultra Hight Vacuum (UHV).

Chapter 1

Introduction

1.1 The discovery of quasicrystals

Up until the discovery of quasicrystals it was though that only 2, 3, 4 and 6 fold atomic arrangements could produce a discrete diffraction pattern. A long range atomic structure possessing other symmetries was deemed forbidden by the crystallographic community.

Quasicrystals were discovered in April 1982 by Dan Shechtman on sabbatical at the National Bureau of Standards in Washington D.C. The aim of his research was to produce new materials with enhanced mechanical properties by increasing the solubility of metals in aluminium alloys. By introducing manganese into the metal matrix and locking in the composition by rapidly cooling the liquid alloy, he was keen to learn how much manganese could be incorporated. Using Transmission Electron Microscopy (TEM) to identify the structures of different phases in the Al-Mn system he observed a ten-fold diffraction pattern when using a composition of 75% of Al and 25 % of Mn. This suggested a well ordered atomic arrangement able to produce constructive interference, yet not produced by a crystal as no translational order was present. By rotating the sample he observed many Bragg peaks which he recognised to be the rotational symmetry elements of the icosahedral group. Dan Schechtman published these results in 1984 [1] which caused much controversy in the world of crystallography. Linus Pauling, a Nobel Laureate and well-known chemist dismissed the findings as caused by multiply-twinned cubic crystals [2]. As the field opened up and more thermodynamically stable quasicrystals were discovered their reality became indisputable.

1.2 A brief history of the surface science of quasicrystals

Since the discovery of the first aluminum based quasicrystal, hundreds of quasicrystals have been found. The first known quasicrystals were meta-sable, formed through rapid quenching. This resulted in the formation of single grain samples a few microns in size therefore making it impossible to test physical properties and allow for structural characterisation. The formation of stable quasicrystals made it possible to prepare single grains of macroscopic scale the first of which was discovered by Dubost *et al* [3]. As a result of careful research into the phase equilibria and the optimal conditions of sample preparation there has been continued improvement over time and it is now possible to produce large, defect free single grains in many phases. Such samples can be grown up to 10 cm long, allowing for many bulk and surface studies to be performed, enhancing our knowledge of quasicrystals and aperiodicity.

Many different types of quasicrystals have been formed, about 80 % of which contain Al, accompanying either a simple metal (i.e. Al-Mg-Zn) or a transition metal (i.e. Al-Pd). The remaining 20 % are either rare-earth based (i.e. Pd-U-Si) or are comprised of transition elements (i.e. Fe-Ti). The structure of these quasicrystals varies; it been found that 82 % of the known quasicrystals are icosahedral, 16 % decagonal and the remaining 2 % either orthorhombic or dodecahedral [4].

Surface science requires that samples are large in size, of high quality and contain low-vapour-pressure elements. As a result the characterisation of only a hand-full of quasicrystal phases in UHV conditions has been possible [4]. This is in part to do with the difficulty in producing some phases as the conditions and quality of growth are limited by the vagaries of the phase equilibrium. There is also a variation in the amount of effort that has gone into the growth and characterisation of individual phase. Presently the phases suitable for use in UHV include *i*-Al-Pd-Mn, *i*-Al-Cu-Fe, *i*-Al-Pd-Re, *d*-Al-Co-Ni, *d*-Al-Co-Cu, and *i*-Ag-In-Yb (see ref [4] and references therein).

The main aim of many surface science studies, has been to confirm the aperiodic arrangement of surface atoms and to use this as a basis to explore the use of such a surface as a template for the deposition and development of a single element quasicrystalline film. This would allow an insight in to the growth kinetics behind aperiodicity.

The study of adsorbates on quasicrystal surfaces required the development of the preparation conditions to enable the study of clean, bulk terminated surfaces.

This work paved the way for adsorption studies on such surfaces motivated by the prospect of forming ordered nanoscale systems, offering the prospect of new physics and chemistry. The group at Liverpool (Ledieu, Cox, Smerdon, Reid, Banks, McGrath), equipped with samples provided by Ames lab, has systematically investigated the surface order of quasicrystals as a function of several controllable parameters: the pre-polishing of the surface prior to the insertion into vacuum, the sputtering conditions, annealing temperature and time. A similar study was preformed by Jenks *et al* [5]. Refinements were made to the preparation of quasicrystals surfaces in particular that of the icosahedral Al-Pd-Mn quasicrystal and the decagonal Al-Ni-Co quasicrystal (in collaboration with Ferralis and Diehl, Penn State [6]). Progress was only enhanced by the many national and international collaborations within the quasicrystal field, an account of which has been written by McGrath et al [7]. Such collaborations have lead to many significant advances in the field. One such advance was made after the high resolution STM imaging of Al-Pd-Mn. Ledieu superimposed a tiling on to a high resolution image which Papadopolos recognised to be identical to a tiling inherent in the Kratz-Gratias-Elser geometric model of the bulk material [8]. This step was key to identifying features in the STM data, with the atomic resolution provided by the geometric model, leading to the general consensus that this surface is in fact bulk terminated. Furthermore the ability to prepare surfaces of such relative perfection has created a solid foundation for the use of these surfaces as templates for the adsorption of other species.

1.3 Order

1.3.1 Periodic order

In a regular crystal atoms are positioned as an infinite arrangement of periodically spaced point, each of which can be defined using translations. The position of any point with respect to any other point in this lattice and the origin is given by

$$\mathbf{r} = a_1\boldsymbol{i} + a_2\boldsymbol{j} + a_3\boldsymbol{k} \tag{1.1}$$

where a_1, a_2 and a_3 are integer numbers and $\boldsymbol{i}$, $\boldsymbol{j}$ and $\boldsymbol{k}$ are unit vectors. This maps the atomic positions in three dimensional space. To keep things simple we shall restrict ourselves to two dimensions, and consider the unit cell to have sides (a_1,a_2). The area depicted by these vectors are unique for a given lattice. For a periodic lattice this unit cell forms the basic building block of the structure,

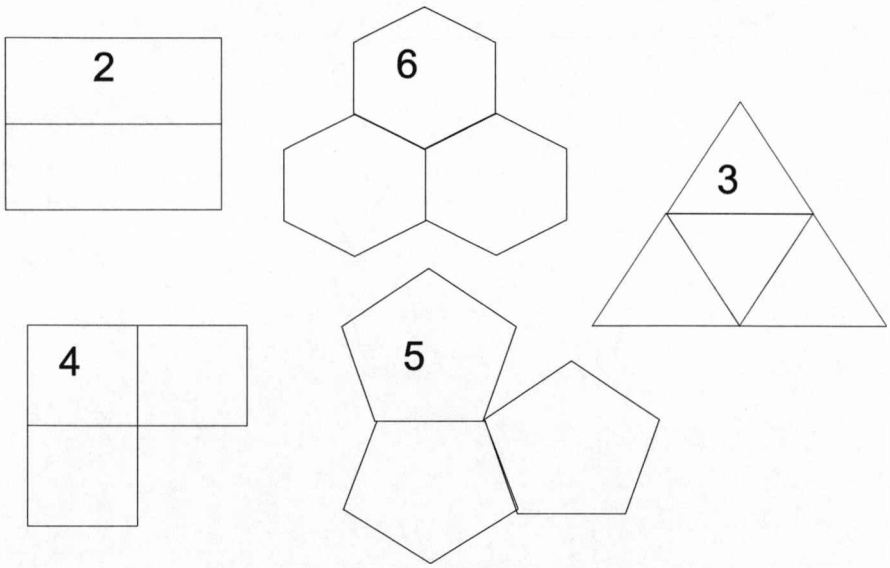

Figure 1.1: Only 2-,3-,4- and 6-fold symmetries can tile a plane.

shapes with 2-, 3-, 4- and 6-fold symmetries fit together to form a regular array, with no voids or overlapping. Shapes with 5-fold symmetries however do not fit together to form such a tiling, as illustrated in Fig. 1.1.

This notion can be extended to three dimensions. The Platonic solids are five regular polyhedra which have identical faces, shown in Fig. 1.2. They were named after the Greek philosopher Plato, who put forward an atomic theory that suggested these shapes made up the fundamental components of the physical universe. Those which have 2-,3-,4- and 6-fold symmetries which allow for periodicity are the tetrahedron, cube and octahedron, and can fill space with no voids. For the icosahedron (containing 20 triangular faces, five around each vertex) and dodecahedron (containing 12 pentagonal faces, three round each vertex) this is not possible. Although twenty tetrahedra can be joined together to form a near complete icosahedron, the dihedral angle of the tetrahedron is slightly too small to close the 2π angle around the edge of icosahedron.

This limitation implies the growth of the icosahedral structure is restricted with monatomic particles. This problem can be overcome by using two types of facet (formed using at least two different atoms) to form a 5-fold structure, examples of which are the icosadodecahedron and the triacontahedron, illustrated in Fig. 1.3.

1.3.2 Aperiodic order

In 1973, prior to the discovery of quasicrystals, Roger Penrose discovered that an aperiodic tiling could be formed by fitting two different types of rhombi to-

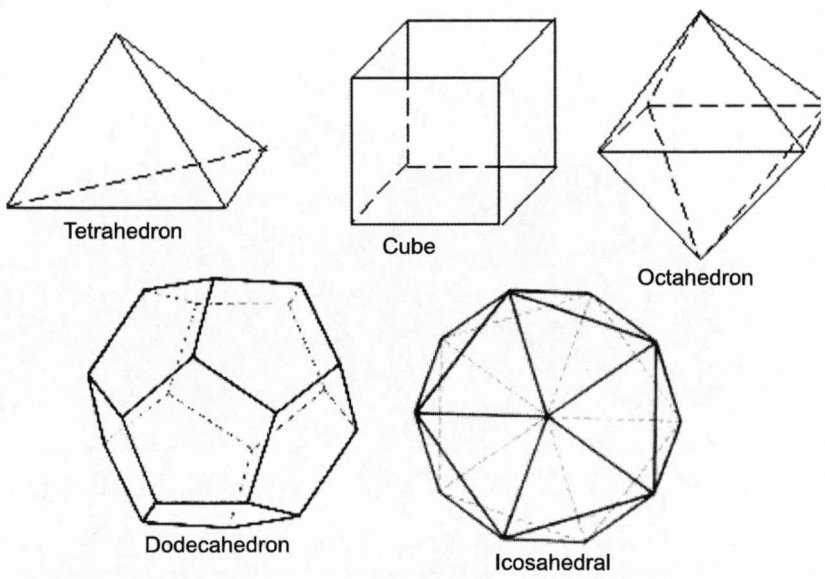

Figure 1.2: Plato's five regular polyhedral containing identical faces.

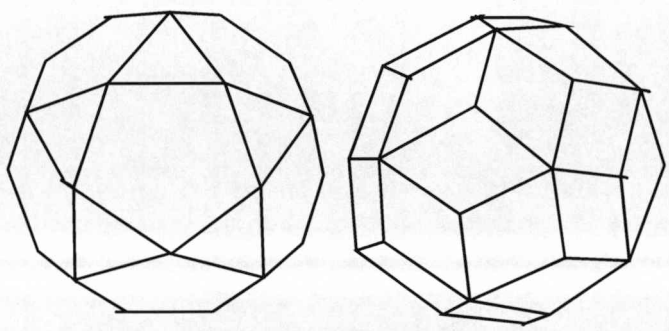

Figure 1.3: Two polyhedra exhibiting 5-fold symmetries, formed from two facets.

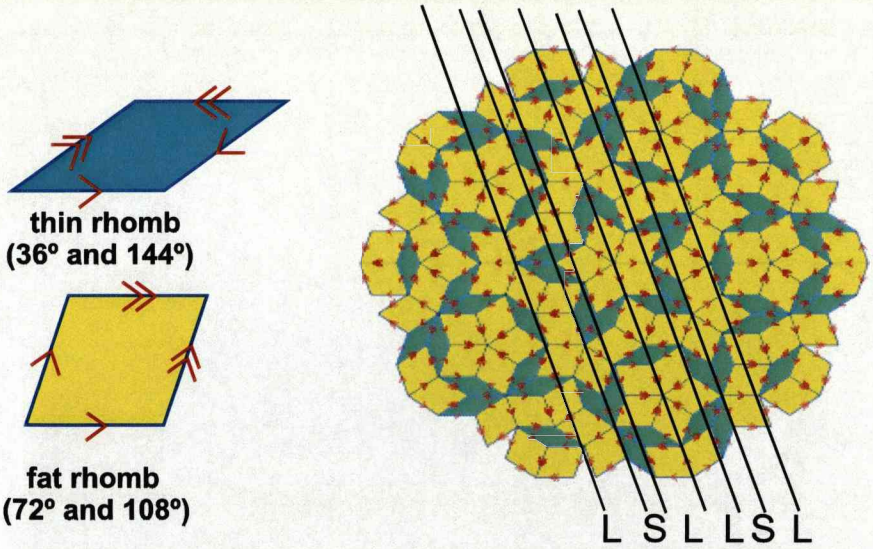

Figure 1.4: The Penrose tiling, formed using fat and thin rhombi placed together using matching rules.

gether, one fat, one thin, by applying certain matching rules. This formed a tiling possessing no periodic order. No part of the tiling can be repeated at regular intervals, while long-range order is observed through the Fibonacci sequence, illustrated in Fig. 1.4.

The sequence of parallel lines which can be drawn connecting the edges of parallel rhombi, form a set of lines with either a long or short space between, mirroring part of the Fibonacci sequence. The sequence was first studied by Leonardo of Pisa (nicknamed Fibonacci), who considered the growth of a rabbit population. The Fibonacci sequence can be formed by adding the last two consecutive numbers in the sequence, i.e. 1, 1, 2, 3, 5, 8, 13, 21, ... just as in the case of the virtual rabbit population. The rules are; in the first month there are just one pair of rabbits, new born pairs become fertile from their second month onwards and on each month every fertile pair produces a new pair of rabbits. A Fibonacci sequence is built up, illustrated in Fig. 1.5. In terms of the Penrose tiling the long and short segments of the sequence can be built up by substituting LS with L and L with S also shown in Fig. 1.5. Small segments of the sequence may reoccur, but not periodically. The sequence extends infinitely without repeating.

The Fibonacci sequence, and the golden mean (also know as τ) are intricately related to aperiodicity: they are the 'signature' of aperiodicity. τ has a value given by

$$\tau = (1 + \sqrt{5})/2 = 1.618 \tag{1.2}$$

It is also the ratio between the length (l) and width (w) of the golden rectangle

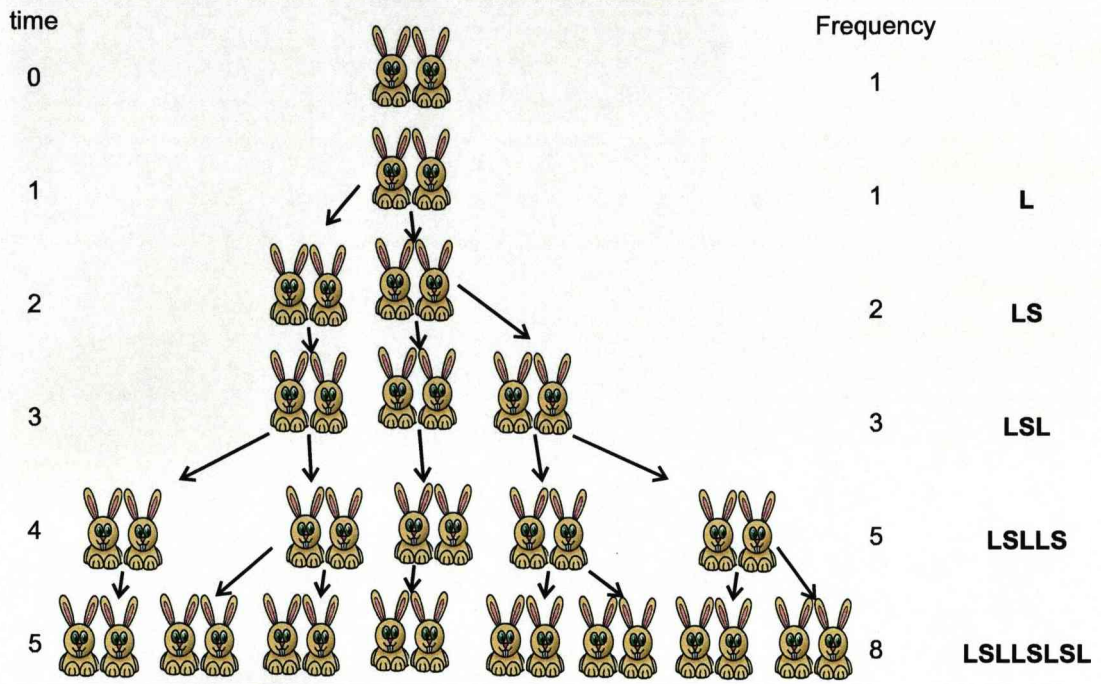

Figure 1.5: Fibonacci's Rabbits population increases over time according to the Fibonacci sequence. Along-side is a Fibonacci sequence built up using the substitution rule L $\leftrightarrow$ LS, S $\leftrightarrow$ L.

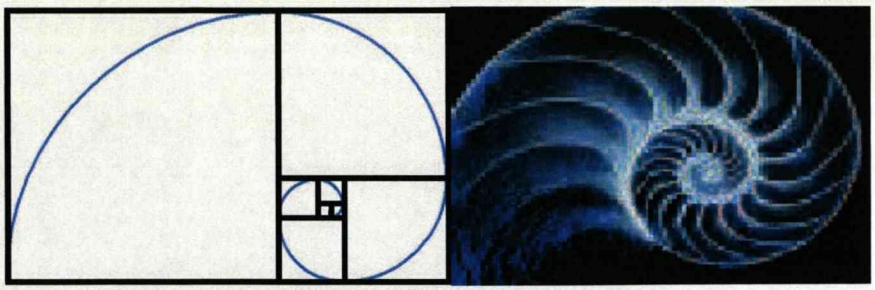

Figure 1.6: Left; golden rectangle, Right; Seashell shape follows the Fibonacci sequence.

illustrated in Fig.1.6, and is therefore a root of the quadratic equation;

$$x^2 - x - 1 = 0 \tag{1.3}$$

Fig. 1.6 shows the golden rectangle, which can be built up based on considerations of the Fibonacci sequence; the edge length of the square added to build up the rectangle equals the sum of the previous two edge length of the squares in the sequence. As the terms in the sequence grow, the ratio between the length and width of the rectangle gets increasingly closer to the actual value of τ, and becomes more 'golden', hence the name the golden rectangle and golden mean. The Fibonacci sequence also describes curves often seen in nature. If a curve is drawn through the outer edges of the square, it makes a prefect spiral. Such curves are observed in nature in the spiral patterns of pinecones, sunflowers, broccoli, seashells and galaxies and in the way the petal formations in flowers evolve. This is an aesthetically pleasing ratio and as a result is used quite often in art and music.

The golden ratio is also seen in pentagons, which explains why this number is observed in the quasicrystalline arrangement of atoms (due to the 5-fold symmetries) and the self-similar nature of quasicrystals, where part of the structure is repeated on a different length scale. This is highlighted in Fig. 1.7. τ is observed by joining up the vertices of a pentagon to produce an even smaller inverted pentagon at its center. The edge length of the different-sized pentagons and the areas divided up by the lines are related by τ.

According to equation 1.3, as illustrated in Fig. 1.7;

$$\tau^{-1} + \tau^{-2} = 1 \tag{1.4}$$

$$\tau = 1 + \tau^{-1} \tag{1.5}$$

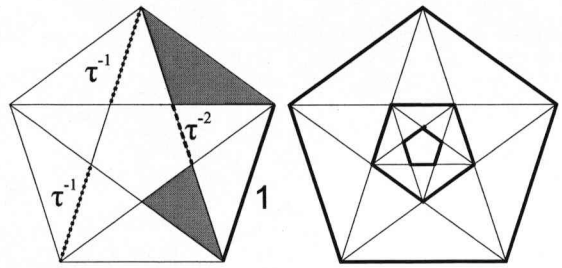

Figure 1.7: A pentagon dissected to produce a smaller pentagon.

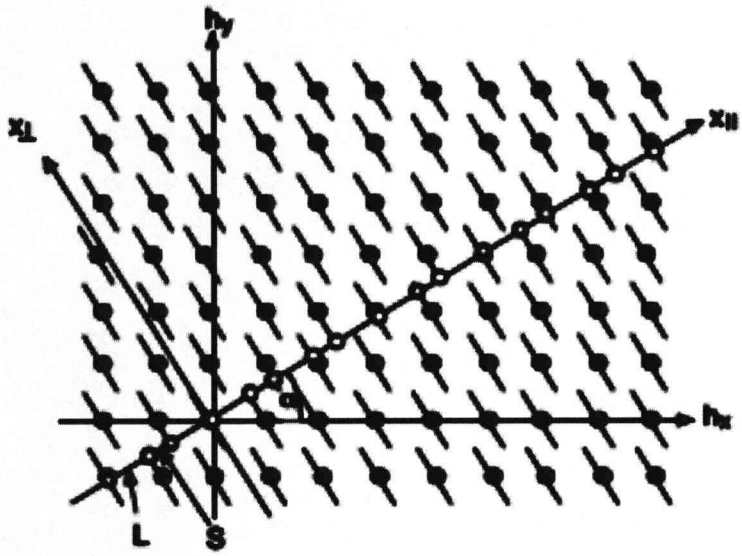

Figure 1.8: Construction of a one dimensional aperiodic array of points via a two dimensional hyper-lattice. Reprint from [9].

This self-similar nature is also observed in the aperiodic Penrose tiling. The golden ratio can therefore be used to identify aperiodicity as this is synonymous with five 5-fold symmetry.

The formation of an aperiodic array of atoms can also be described by considering a higher dimensional space construction (known as a hyperlattice), illustrated in Fig. 1.8. A two dimensional hyperlattice has been defined; h_x represents physical space, h_y orthogonal space. The Fibonacci sequence can be generated by slicing through a periodic array of atoms at an angle with an irrational tangent. For this example it has been chosen to be the inverse of the golden mean. The atomic positions in real space are located where this line cuts through the objects. By using a periodic array of atoms in six dimensional space, the structure of a three dimensional aperiodic arrangement of atoms in real space can be described, as observed in the icosahedral quasicrystal structure.

1.4 Magnetism and quasicrystals

1.4.1 Review

At the atomic scale the magnetic moment has three sources. The first is the orbital motion of electrons around the nucleus, termed the orbital dipole magnetic moment. The second, much stronger form of magnetism is known as spin. This arises from a quantum mechanical property of the electrons, known as the spin magnetic moment. Pairs of electrons with spin up and spin down orientations cancel each other out. According to the Pauli exclusion principle no two electrons can occupy the same quantum state at the same time. The result is that electrons occupy different quantum states of a shell, which when full results in a net moment of zero. Atoms with fully complete shells of electrons tend to have no magnetic moment. Atoms with incomplete shells of electrons have a magnetic moment, the strength of which depends on the number of unpaired electrons.

For many electron atoms the pairing of electrons is determined by the vector sum of the orbital and spin angular momentum of the individual electrons. The total angular momentum J is expressed as

$$\mathbf{J} = \mathbf{L} + \mathbf{S} \tag{1.6}$$

The last source of magnet moment is the change in orbital moment induced by an applied magnetic field. A system of many atoms will always respond in the present of an external magnetic field. For localised electrons this response will be in the alignment of the magnetic moments along the external magnetic field. The reason for this is to reduce energy within the system.

As the strength of the applied magnetic field increases, the orientation of the magnetic moments changes from random to complete alignment when a particular saturating field is reached. The alignment of these moments to an external magnetic field may vary for different materials. The type of magnetism observed maybe defined by the magnetic susceptibility. The magnetic susceptibility per unit volume is defined as

$$\chi = \frac{M}{B} \tag{1.7}$$

where B is the macroscopic magnetic field intensity and M the magnetisation, which is defined as the magnetic moment per unit volume.

Substances with negative magnetic susceptibility are called diamagnetic. Substances with positive magnetic susceptibility are called paramagnetic. Diamagnetism is associated with the tendency of electrical charges partially to shield

the interior of a body from an applied magnetic field. The external magnetic field induces (diamagnetic) current which acts to form an internal magnetic field opposing the external field. Paramagnetism is associated with the total angular momentum of the system, which is the sum of the spin and orbital angular momentum, as shown in Eqn. 1.6.

A ferromagnet has a spontaneous magnetic moment-a magnetic moment even in zero applied magnetic field. The existence of a spontaneous moment suggests that electron spins and magnetic moments are arranged in a regular manor. In an antiferromagnet, the spins are ordered in an antiparallel arrangement with a zero net moment at temperatures below the ordering or Neel temperature [10]. The class of ferromagnetic materials includes Ni, Co and Fe. Part of the goal of this thesis is to investigate the effect of depositing atoms which are ferromagnetic in nature onto quasicrystal surfaces in the hope of forming an aperiodic magnetic overlayer. This would increase our understanding of aperiodicity and could lead to new physical phenomena.

1.4.2 Bulk magnetic properties of quasicrystals

Although magnetism in bulk quasicrystals has been studied extensively, strong magnetic effects are not observed. In icosahedral quasicrystals such as the *i*-$Al_{70}Pd_{21}Mn_9$, or decagonal quasicrystals such as *d*-$Al_{72.6}Ni_{10.5}Co_{16.9}$ [11], the magnetic elements are dispersed in a non-magnetic framework with a multiplicity of distances between the magnetic species which leads to very effective screening. This limits the possible magnetic interactions.

Many studies have been centered on the discovery of the rare-earth based quasicrystals, in the hope they provide an insight in to the magnetic effects of incorporated atoms with magnetic moments, in to the bulk quasicrystal structure. Sato *et al* [12] used neutron scattering experiments to study the magnetism of the *i*-$Zn_{60}Mg_{30}Ho_{10}$ system. Since Ho is a rare earth with localised 4f magnetic moments (or atomic spins), it provides the opportunity to study the magnetism on the quasiperiodic lattice. The study shows the magnetic susceptibility exhibits spin glass like behaviour, explaining the presence of short range magnetic order. No long-range magnetic order was detected. This is contrary to the results obtained by Benoit *et al* for the *i*-$R_8Mg_{42}Zn_{50}$ quasicrystal, where R is the rare earth Tb, Dy, Ho or Er [13]. The results show the presence of a long-range quasiperioidic antiferromagnetic structure. What is evident through both studies is that strong magnetic effects are not observed in any case. This may be due to the relatively low concentrations of the rare-earth atom in the substrate.

Much work has been done to measure the magnetic susceptibility of the

decagonal Al-Ni-Co quasicrystal, as this provides an opportunity to probe the magnetism across the periodic and aperiodic planes. Yamada *et al* [14] carried out measurements on the single grain *d*-$Al_{72}Ni_{12}Co_{16}$ quasicrystal. They found that the decagonal quasicrystal exhibits diamagnetic behaviour. The anisotropic susceptibility was found to be greatest along the c-axis (periodic axes) of the quasicrystal. This is in agrement with the dc magnetic measurements taken by Markert *et al* [15] of the single grain *d*-$Al_{70}Ni_{15}Co_{15}$ quasicrystal. This is in further agreement with the work of Jeglic *et al* [11]. Using NMR they also determined the Co to be in a nonmagnetic state.

Chapter 2

Quasicrystal surfaces and epitaxy

2.1 Introduction

In this chapter, the bulk and surface structure of the *i*-Al-Pd-Mn and *d*-Al-Ni-Co quasicrystals are introduced. A brief description of growth modes is then given, followed by review of previous works on epitaxy on quasicrystal surfaces.

2.2 Quasicrystal structure and surfaces

Quasicrystal structures can be of two types. Belonging to the first type are the axial quasicrystals. These exhibit 8-, 10- and 12-fold rotational symmetries. The structure consists of a periodic stacking of aperiodic planes. An example is the decagonal Al-Ni-Co quasicrystal. The second structure type is the icosahedral quasicrystal, which is aperiodic in three dimensions. The Al-Pd-Mn quasicrystal used in this study has icosahedral symmetry.

2.2.1 The bulk structure and 10-fold surface of *d*-Al-Ni-Co

The bulk structure of decagonal quasicrystals has been the subject of many studies, see reference [6] and references within. The structure of decagonal quasicrystals can be best described using stacks of 2D Penrose tilings.

The basic bulk structure of *d*-AlNiCo consists of a stack of near identical 5-fold symmetric planes. Clusters in successive planes are rotated by $\pi/5$. On the 10-fold surface a bulk terminated structure exists [16, 17], with a degree of

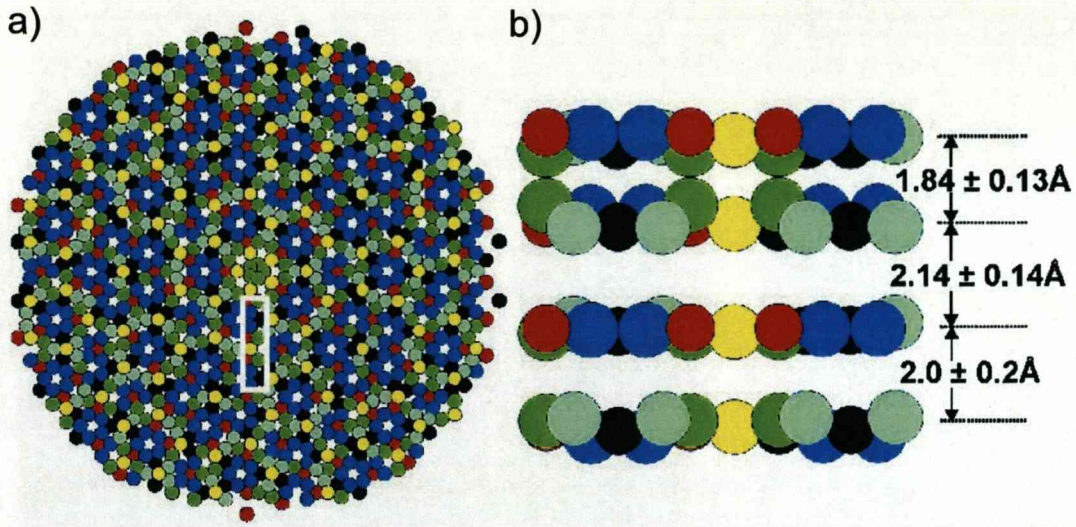

Figure 2.1: (a) The top view of one layer of atoms, having a diameter of roughly 90 $\mathring{A}$. The different shades of grey (or colour) correspond to the subgroups (or subplanes) used in the model listed in table 2.1. The atoms are in order of greyscale darkness first and color are; TM-2 (black), Al-2 (blue), TM-1 (red), Al-1 (green), Al-3 (cyan), and Al-4 (yellow). (b) Side view of the first four layers (viewing white box in (a) from left), surface relaxation and rumplings are exaggerated for clarity, its maximum amplitude is 0.1 $\mathring{A}$. Reprint from [6].

relaxation consistent with a non-close-packed metal surface. This is shown in Fig. 2.1. The model, illustrated in Fig. 2.1 and based on dynamic LEED I-V, high-resolution STM, shows the outermost layer spacing is contracted by 10 % relative to the bulk inter-layer spacing, while the second layer is expanded by 5 %. The contraction of the top layer is understood to be a response to charge smoothing present at metallic surfaces [18].

A small degree of intralayer rumpling is also observed of magnitude 0.1 - 0.2 $\dot{A}$. Rumpled atoms form a deca-prismatic columnar cluster and tend to be located towards the surface, away from the bulk relative to other atoms. The composition of the surface is essentially the same as the bulk [6]. Table 2.1 provides the key for the model shown in Fig. 2.2, separating the quasicrystal plane into subplanes. The transition metals (TM) are indistinguishable by LEED due to their similar size. This was later resolved using extended x-ray fine structure (EXAFS) where it was determined that TM-1 corresponds to Co and TM-2 to Ni [19]. This technique uses photons to probe the adsorption edges of the elements present, and can determine the atomic number, distance and coordinate number of the atoms surrounding the elements whose adsorption edge is being examined.

The STM image shown in Fig. 2.3 was processed using a Fourier filter to enhance the strongest Fourier components of the image in reciprocal space, followed

Group	Coordination	NN distance (Å)	No. atoms	% atoms
TM-1[a]	3	2.43	110	12
TM-2[a]	4 or 5	2.43	140	15
Al-1	1	2.24	165	17
Al-2	2	2.43	300	32
Al-3	3	2.43	145	15
Al-4	4 or 5	2.43	85	9

Table 2.1: Table identifying the subgroups present in the Fig. 2.1. [a]Although indistinguishable in LEED, TM-1 can be identified as Co and TM-2 as Ni, through EXAFS [19]. Reprint from ref. [6].

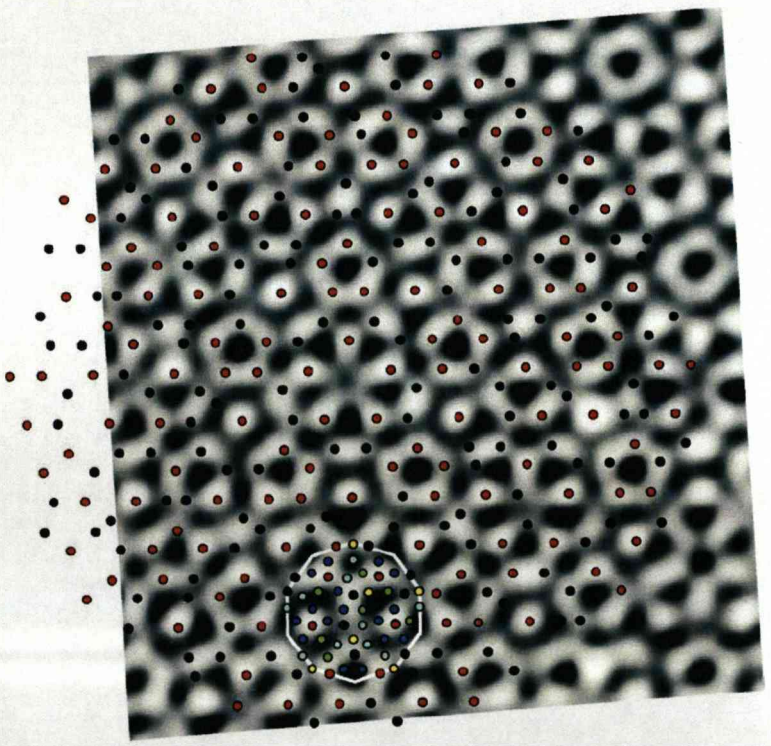

Figure 2.2: The atomic model (Table 2.1) superimposed on an enhanced STM image of Al-Ni-Co. Reprint from [6].

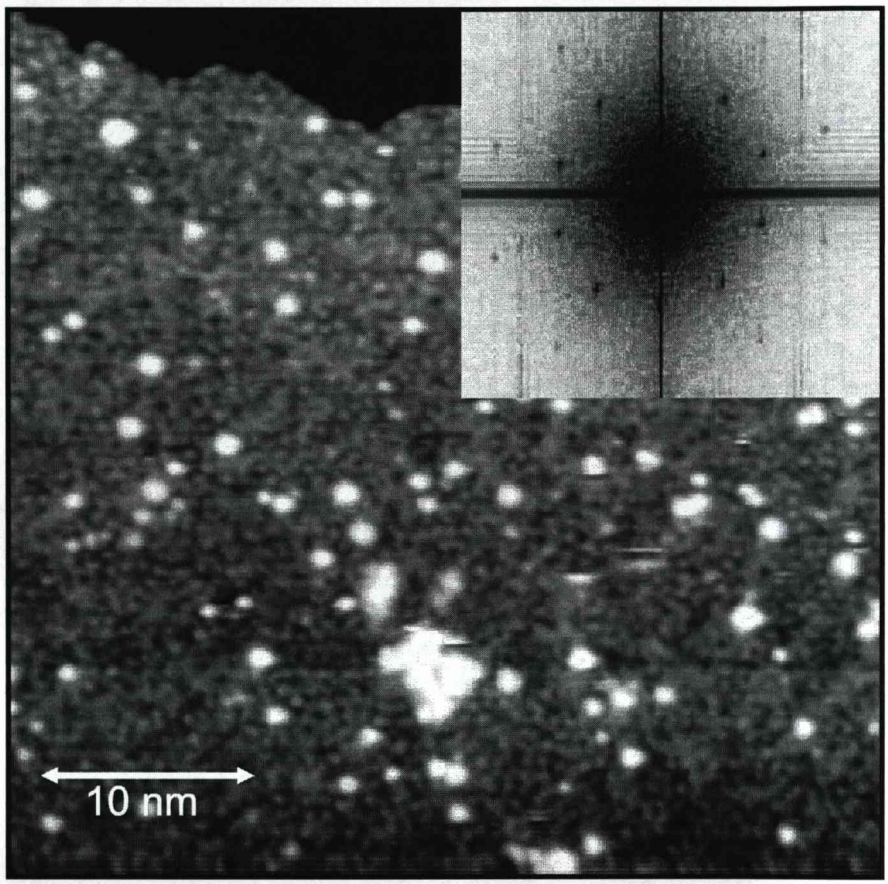

Figure 2.3: A 40 nm by 40 nm high resolution STM image of the clean 10-fold surface of Al-Ni-Co. Insert: FFT taken from (a). Taken by J.A. Smerdon, University of Liverpool.

by an inverse transformation to real space. The resultant high resolution image of the surface is shown. The model is superimposed. It can be seen that the brightest protrusions on the STM image are formed from a pentagonal arrangement of atoms with the Co (TM-1) atoms central to five Al atoms. It appears that the Ni (TM-2) atoms also produce a protrusion, yet not as pronounced. This is because the Co atom appears to glue pentagonal clusters together rather than form into such features. This shows atoms and protrusions can be grouped together to form pentagonal and decagonal features.

Figure 2.3 shows a high resolution STM image of the clean surface of Al-Ni-Co taken prior to dosing. Large flat terraces are formed by annealing to 800°C for long periods of up to 4 hours, followed by a 45 minute sputter. A total anneal time of around 20 hours is required to form such a surface. The inset in Fig. 2.3 shows a Fast Fourier Transform (FFT) taken from this STM image. The sharpness of the spots indicates a well ordered 10-fold substrate.

2.2.2 The bulk structure and 5-fold surface of *i*-Al-Pd-Mn

Unlike axial quasicrystals, where the atomic structure may be described using stacks of 2D Penrose tilings, icosahedral quasicrystals are aperiodic in three dimensions. Therefore it is much harder to determine atomic structure. Due to the complexity of modeling such a structure in three dimensions, the structure is best explained using 6D crystallography. By superimposing an extra 3D, the structure can be described using a 'periodic' 6D array, as described earlier in Section 1.3.2.

It has been observed that these structures comprise of one or more basic building blocks termed clusters. A cluster is a set of close atoms distributed on fully occupied high symmetry sites, which are typical of the structure and are found frequently within the structure. Clusters may overlap and are held together by glue atoms.

The basic building block of the icosahedral Al-Pd-Mn quasicrystal is the pseudo-MacKay icosahedron (PMI) cluster as illustrated in Fig. 2.4(b). Bergman clusters are also observed within the structure (Fig. 2.4(a)). These clusters are discussed in greater detail by Gratias *et al* [20]. The proportions of each type of building block are difficult to determine. The PMI cluster is termed the basic building block as this forms the atomic skeleton of the primitive 6D cubic icosahedral compounds. These large clusters comprise up to 102 atoms, which organise according to a hierarchical scheme, so that PMI condense into larger building blocks. These are themselves formed of PMI clusters which occupy the same positions as individual atoms in the previous step of the hierarchy [21]. The PMI clusters have a number of electrons which are shared between the atoms in the

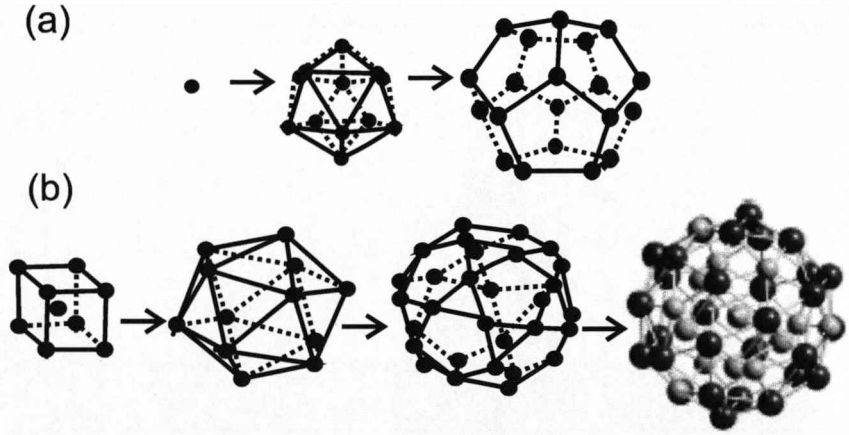

Figure 2.4: Structure components of the icosahedral quasicrystals (a) Bergman cluster and (b) PMI cluster[20].

cluster. This is close to a magic number, which satisfies the Shrödinger equation for a deep spherical well. As a result the clusters trap the electrons, enforcing localisation, stabilising the structure. Bergman units describe the structure of the face of the 6D cubic icosahedral compounds. These clusters are smaller in size and consist of 44 atoms.

The structure of Al-Pd-Mn can be described using the geometric model [22]. The geometric model consists of alternating Bergman and Mackay polytopes on the vertices of the 6D primitive tiling τ^{2F} [23].

The terraces orthogonal to 5-fold surface of Al-Pd-Mn have heights which follow a Fibonacci sequence, with a short height of 4.22 ± 0.26 $\mathring{A}$ and long height of 6.78 ± 0.24 $\mathring{A}$. It follows that the basic building blocks of the structure i.e. the Bergman and MacKay clusters order in such a way that when sliced form such a sequence in the step height. These clusters must be cut to form the regular motifs which can be identified on the surface through STM. The fine details of the surface structure can be interpreted in terms of bulk models [8], and density functional theory results allow detailed comparison with high resolution STM images [24]. It has been shown that the surface is bulk-terminated [8] with some degree of relaxation of the outermost layer [25].

Through high-resolution STM analysis and comparison of features observed with those in the geometric model, the dark pentagonal holes can be interpreted as dissected Bergman clusters [8]. The white flower can be interpreted as a truncated PMI cluster [26]. High resolution STM images of these features are shown along-side an atomic model of the surface, Fig. 2.5.

Each terrace has a different surface termination, which can be tiled with a P1 (Penrose type 1) tiling. Figure 2.5(d) shows features observed on the surface of

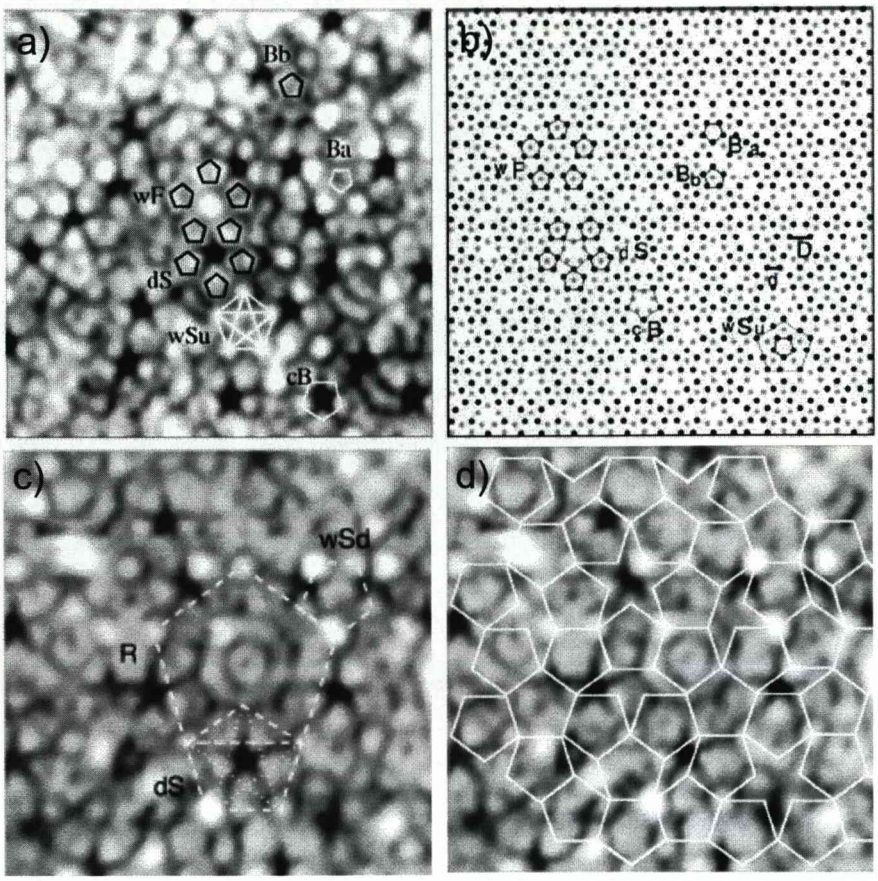

Figure 2.5: (a) 100 Å x 100 Å high resolution STM image of the 5-fold surface of Al-Pd-Mn, highlighting features such as dark stars (ds), white flower (wf), white star pointing upwards (wSu), the Bergman polytope below the surface (Bb), above the surface (Ba), and the Bergman polytope dissected by the terraces (cB); (b) The atomic model of the terrace in (a), the decreasing greyscale represents different planes in the model, for a true representation of the atomic positions consult [8]; (c) 75 Å x 75 Å high resolution STM image of the five-fold surface of Al-Pd-Mn, showing a different type of terrace to that observed in (a), highlighting features such as a ten-fold ring (R) and white star pointing downwards (wSd); (d) 75 Å x 75 Å segment of an STM image of the ringed terrace (c) with a superimposed exact path of the P1 tiling of edge length 7.8 Å. Reprint from [8].

Al-Pd-Mn, including ten-fold rings, dark stars and white flowers.

The flat surface is obtained through long annealing. If annealing isn't performed at sufficient temperatures or for a long enough period of time the surface has a high corrugation and appears to be made up of clusters. The longer annealing time allows for the dissection of the Bergman clusters, and the formation of a relatively flat surface. The protrusions on the flat surface have been interpreted as material which has not yet diffused to the step edge [8].

2.3 Growth modes

2.3.1 Motivation

The formation of thin films on surfaces has many applications. An example is the modification of tribological properties to improve wear resistance or reduce friction for mechanical properties. Other examples include improvement of magnetic properties for increasing data storage densities; and the enhancement of the properties of lenses and mirrors, where optical coatings filter out wavelengths of light to reduce unwanted reflections from surfaces or reflect all light to produce mirrored surfaces. A final example is to improve electronic properties for semiconductor devices and enable the development of new areas of research such as nanotechnology.

The study of thin film growth on quasicrystal surfaces offers the potential for new growth phenomena, as well as enhanced understanding of epitaxy and new insights into the interplay between periodicity, quasiperiodicity and physical properties.

2.3.2 Growth modes

Film growth can be categorised into three basic groups, shown in Fig. 3.2.2. The first is layer-by-layer growth (Frank-van der Merve) [27]. This occurs when the interaction between substrate and adsorbate atoms is stronger than between neighboring adsorbate atoms. Each new layer starts only after the completion of a full layer. The opposite case is island growth (Volmer-Weber) [27], where the interaction between the neighboring adsorbate atoms is greater than between the adsorbate and substrate atoms. This leads to the formation of multi-layered islands. The intermediate case is layer-plus-island growth (Stransky-Krastanov) where 3D island growth is observed after the formation of at least one complete monolayer.

A distinction between each of the growth modes can be made in terms of the surface or interface energy γ, this is expressed by Young's equation (Eqn. 2.1) which relates the contact angle of a droplet or film nucleus to the surface energy:

$$\cos\theta = \frac{\gamma_{sv} - \gamma_{sf}}{\gamma_{fv}} \tag{2.1}$$

where θ is the angle the droplet makes with the substrate, illustrated in Fig. 2.7 and the subscripts used to denote γ correspond to the interface between the substrate and film (sf), substrate and vapour (sv), and film and vapour (fv).

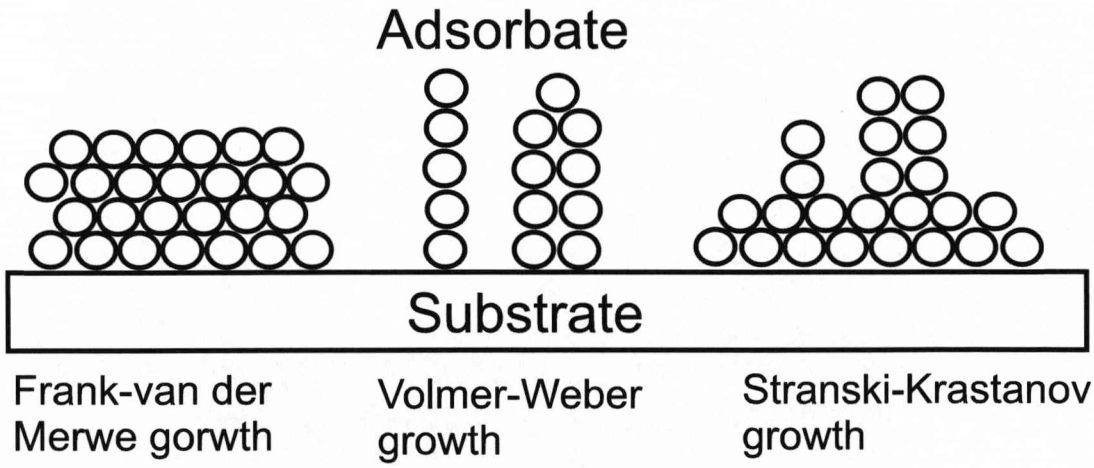

Figure 2.6: The three most basic growth modes: (a) Layer-by-layer growth, (b) Island growth and (c) Layer plus island growth.

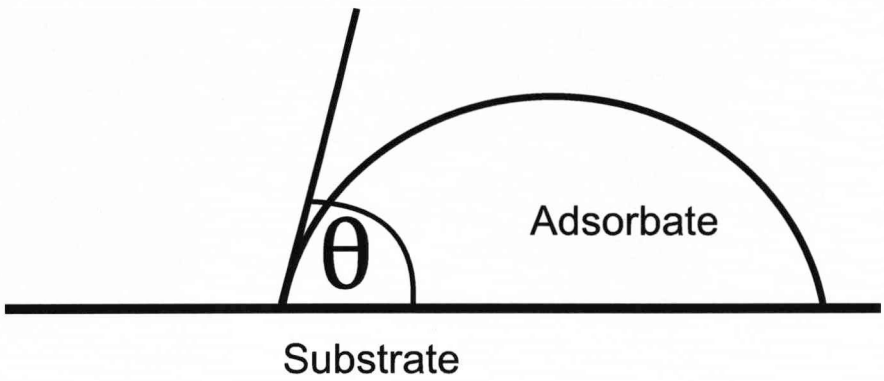

Figure 2.7: The angle depicted indicates the growth mode of the film.

For layer-by-layer growth $\theta = 0$ and so

$$\gamma_{sv} \geq \gamma_{sf} + \gamma_{fv} \tag{2.2}$$

For island growth $\theta > 0$ and so

$$\gamma_{sv} < \gamma_{sf} + \gamma_{fv} \tag{2.3}$$

Surface energy with in the system is kept to a minimum; adsorbates with low surface energies (in comparison to the substrate surface energy) will wet the surfaces of substrates and the resultant growth mode will be the formation of a complete layer. Adsorbates with a higher energy will form 3D islands (thus increasing surface area and lowering the overall energy of the system).

Other types of growth modes may also be observed, these include simultane-

ous multilayers, monolayer plus simultaneous multilayers and alloy or compound formation. For simultaneous multilayers to be observed the surface mobility of adsorbate atoms must be negligible; atoms impinging on the surface stick where they land. Alloy formation occurs when the adsorbate atoms react with the substrate atoms.

The prediction of the type of growth mode from energetic considerations is a complex one, as it is often easy to approximate the surface and adsorbate energies but difficulties arise when calculating the interfacial surface energy. This depends on the epitaxial relations between the two crystal lattices (the misfit) and the degree of strain.

2.4 Deposition on quasicrystal surfaces.

During the growth of epitaxial films three types of film structure may result. The first type is the formation of a crystalline film which bears no structural relationship to the substrate. The next is the formation of a crystalline film which is orientated with respect to the substrate; this is termed rotational epitaxy. The last and most interesting possibility is that of pseudomorphic growth, were the film grows with a structure commensurate with that of the substrate, in a manner dictated by the interaction with the surface. As a result the film may form a unique structure with interesting properties. Much work has been carried out in this area and the most interesting systems are discussed below.

2.4.1 Deposition of nonmagnetic elements

The pseudomorphic structure of the thin film can take three forms; it can arrange aperiodically in zero, one or two dimensions. This depends on the compatibility of the adsorbate atoms to conform to such an arrangement determined by the preferential adsorption sites. The factors which determine the ability to bond to these sites include the size of the atoms/molecules and the interfacial energy between the surface and film. This directly influences the site at which the molecules adhere to the surface by determining whether the atoms/molecules able to diffuse across the surface until they reach such a nucleation site.

Zero dimensional quasiperiodic ordering

The observation of such a zero-dimensional ordering was observed for C_{60} on the 5-fold surface of Al-Pd-Mn at low coverages (~0.065ML) [28]. It was observed that C_{60} binds to preferential high symmetry, pentagonal hollow sites. As a result a τ-scaling in the distance between C_{60} molecules was observed over short distances. Fig. 2.8 illustrates this relationship. It can be seen that [AB]=30±3Å, [AC]=50±3Å, [AD]=85±4Å and [AE]=141±5Å. The distances between the C_{60} molecules and binding sites are therefore related;

$$[AE] = \tau[AD] = \tau^2[AC] = \tau^3[AB] \tag{2.4}$$

$$[EH] = \tau[EG] = \tau^3[EF] \tag{2.5}$$

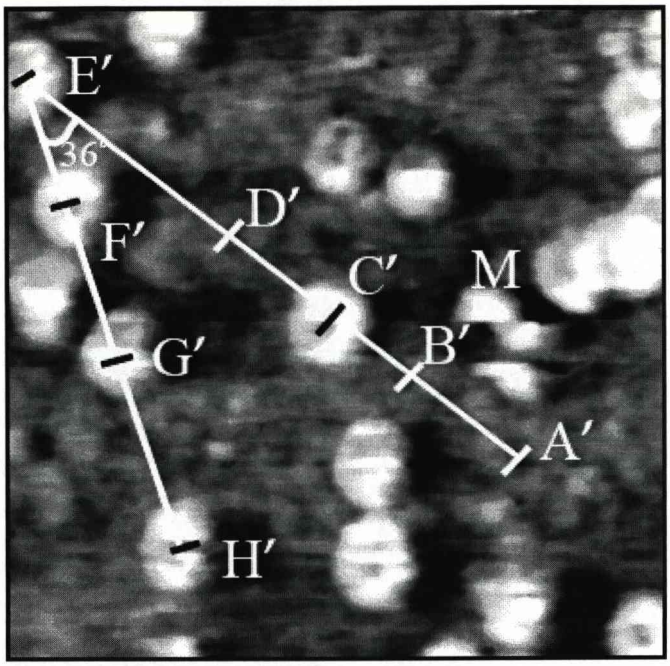

Figure 2.8: 150 $\AA$ by 150 $\AA$ STM image of 0.065 ML C_{60} on the 5-fold surface of Al-Pd-Mn, reprint from [28]

One dimensional quasiperiodic ordering

The formation of a pseudomorphic one dimensional aperiodic array was observed in the row structure of Cu on the 5-fold surface of Al-Pd-Mn [29, 30]. This structure was observed after the deposition of between 5 and 25 monolayers. Domains of Cu are formed which aligned along the 5-fold symmetry directions of the substrate. A row structure is present with in these domains. Atoms within the rows are spaced periodically, while the rows themselves are spaced according to a Fibonacci sequence as shown in Fig. 2.9. Low energy electron diffraction confirms the periodic intra-layer spaces (as streaks) and the aperiodic spacing of rows.

Two dimensional quasiperiodic ordering

The formation of two dimensional quasiperiodic clusters and arrays have been observed for the deposition of a number of films onto quasicrystal surfaces. The formation of pentagonal arrangements of atoms, or motifs, has been observed at submonolayer coverages for Si on the 10-fold surface of Al-Ni-Co and Al on the 5-fold surface of Al-Cu-Fe [31, 32]. Si adsorbed onto the five-fold surface of Al-Pd-Mn forms into a quasiperiodic array; the adsorbate atoms spread out across the surface [26]. The two different structures are illustrated in Fig. 2.10.

At coverages of 0.3 ML and below Si is found to order aperiodically on the

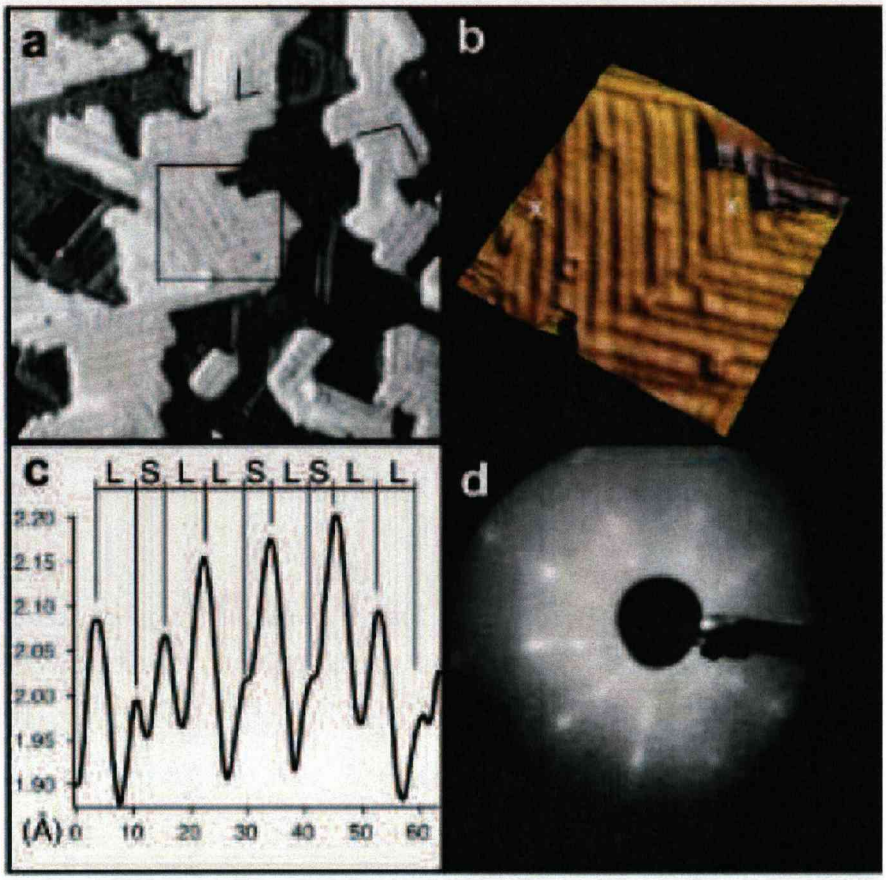

Figure 2.9: One dimensional pseudomorphic Cu film on the 5-fold surface of Al-Pd-Mn (a) 400 $\mathring{A}$ x 400 $\mathring{A}$ STM image taken at a coverage of 5.5 ML; (b) enlargement of domain in (b) 100 $\mathring{A}$ x 100 $\mathring{A}$; (c) Plot profile taken across domain, start and end points marked, illustrating the formation of a Fibonacci sequence; L = 7.3 $\pm$ 0.3 $\mathring{A}$ and S = 4.5 $\pm$ 0.2 $\mathring{A}$ and (d) LEED pattern taken at this coverage. The τ-scaled relationship between spots is due to the aperiodically spaced rows. The streaking corresponds to the periodically spaced atoms within rows. Reprint from [29].

10-fold surface of Al-Ni-Co [31]. The atoms adsorb as single atoms and in pentagonal clusters, consisting of a central atoms with five surrounding atoms. Two arrangements are observed each related by inversion symmetry. Both arrangements of pentagons are observed on the same terraces and have edge length 4.2 $\pm$ 0.2 $\AA$. This corresponds to the edge length of the pentagonal hollows observed in the substrate. Upon further deposition the local 5-fold order is destroyed.

A similar structure is also observed for Al deposited on the 5-fold surface of Al-Cu-Fe at a coverage of 0.04 ML [32]. The edge length of such clusters is 5.1 $\pm$ 0.2 $\AA$. A single Al atom diffuses across the surface until it drops into a hole at the center of an empty pentagonal hollow, where it becomes trapped. This central atom stabilises the adsorption of five more Al atoms around its periphery. Upon further deposition these clusters do not grow laterally, but vertically, destroying the aperiodicity of the film.

Si deposited on the 5-fold surface of Al-Pd-Mn forms an aperiodic array of atoms. These atoms do not form clusters but diffuse across the surface bonding as single atoms in the pentagon hollow sites [26]. The Si atoms are postulated to bond strongly to Mn atoms with considerable charge transfer. The formation of such clusters is therefore inhibited due to the repulsion of adatom-adatom interactions. At 0.25 ML a sharp FFT can be taken from the film. The sharpness of the spots decreases as the film growth proceeds to one monolayer.

For each of the systems discussed above a local 5-fold structure is observed at low coverages. As the coverage increases the atom-atom interaction becomes increasingly stronger until it exceeds that of the atom-substrate interaction. At this point the continuation of aperiodic growth ceases and the film grows with a structure dictated by the atom-atom interaction. It has been reported that in the following systems the atom-substrate interaction is strong enough to allow the formation of a truly aperiodic single element film.

The formation of a quasicrystalline single element film has been observed for Sn, Bi and Sb [33, 34]. At a coverage of one monolayer of Sn on the 5-fold surface of Al-Cu-Fe, held at an elevated temperature of between 300 to 350°C, the formation of an aperiodic film was observed through STM. A monatomic smooth film was formed which possessed both 5-fold elements and protrusions which adsorb in pentagon hollow sites. Bi and Sb monolayer aperiodic films are formed at an elevated temperature of 300°C on the 5-fold surface of Al-Pd-Mn and 10-fold surface of Al-Ni-Co [34]. These films were characterised using low energy electron diffraction and He atoms scattering. The results also show a highly ordered quasicrystalline monolayer.

These results provide hope that quasicrystals may allow the formation of an aperiodic monolayer or thin film composed of magnetic elements.

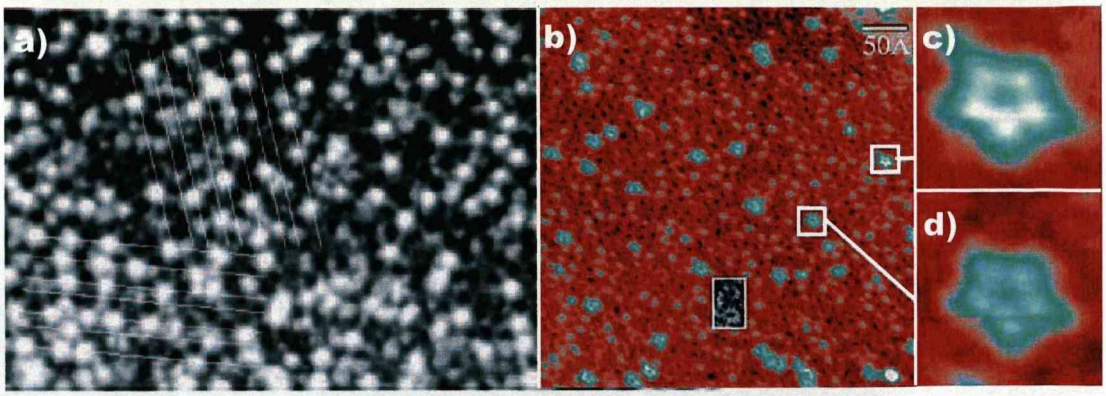

Figure 2.10: Pseudomorphic submonolayer deposition of (a) Si on the 5-fold surface of Al-Pd-Mn at 0.25 ML coverage, 302 Å by 218 Å STM image. Reprint from [26]; (b) Al on the 5-fold surface of Al-Cu-Fe at a coverage of 0.04 ML , 450 Å by 450 Å STM image; (c-d) enlargement of star features in (b). Reprint from [32].

2.4.2 Deposition of magnetic elements

There is currently great interest in the understanding of magnetism of ultra thin magnetic structures due to a wide range of industrial applications. One such application is known exchange bias, utilised in the magnetic recordings industry. One of the main themes of this thesis is the assessment of the possibility of the formation of magnetic aperiodic structures using quasicrystals as templates. The next subsection describes theoretical work and the one following reviews previous experimental work in this area.

Theoretical study of magnetic aperiodic system

Quasicrystals can be structurally ranked between periodic lattices and disordered materials. In a magnetically frustrated system the arrangement of dipole moments produces a net magnetic moment of zero. In highly ordered magnets frustration is uniform, in disorderd materials frustration is random. In quasicrystals the atoms have a coordinate number which changes from 3 to 7 and as a result the energy per magnetic moment varies. This variation in dipolar energy leads to an increase in the degree of frustration.

A theoretical study by Vedmedenko et al [35] using Monte Carlo simulations has been performed to find the equilibrium spin configurations of aperiodically arranged dipoles, illustrated in Fig. 2.11(a). Bar magnets are arranged at the vertices of a Penrose tiling and the results indicate the magnetic moments orientate into two structures; ordered decagonal rings, where moments are coplanar to the sides of the decagon and frustrated disordered spin-glass-like structures within the

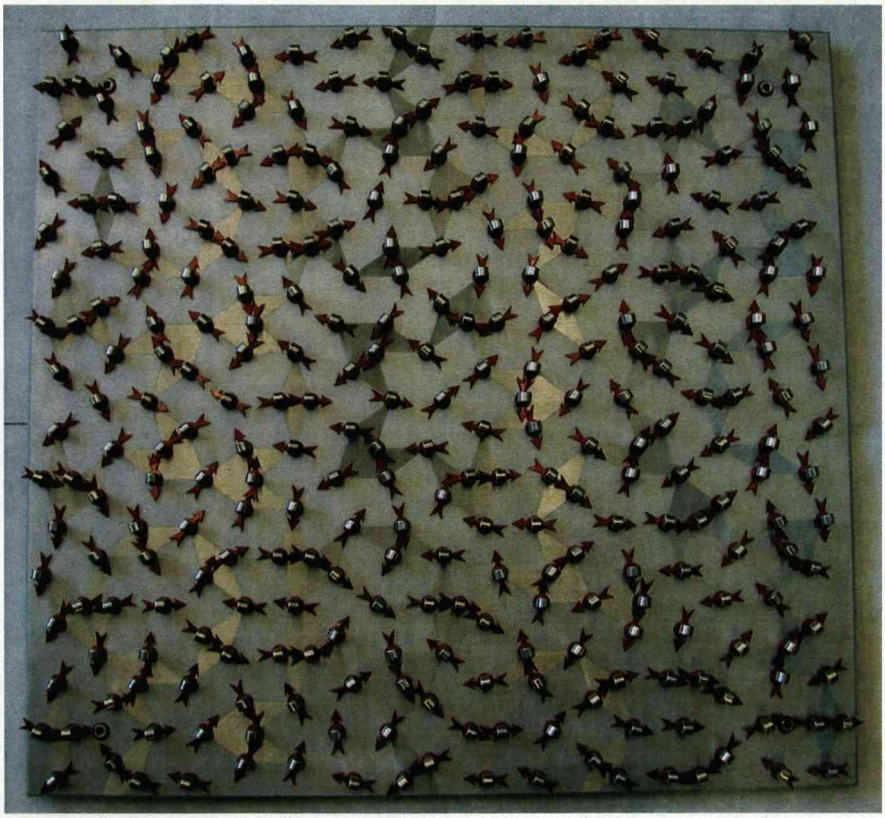

Figure 2.11: (a) Experimental model of bar magnets fixed onto the nodes of a Penrose tiling. Reprint from [35].

rings. Both arrangements result in a net moment of zero, hence the term magnetic frustration. These micromagnetic structures are unique as all frustrated system which have been investigated so far have either a continuous degenerate, periodic ground state, (i.e. spins on a honeycomb, a kagome (a two-dimensional lattice formed of corner sharing triangles) [36]) or a completely disordered one. Thus a magnetic system on a Penrose tiling belongs to a new class of frustrated system, where the degenerate ground state is aperiodic with the ordered decagon rings and disordered spin-glass like phase inside. If such a system could be produced using the dipole moments of individual atoms, this may result in the formation of a novel material with unique properties, which could be exploited by for example such as the magnetic recording industry. For this reason one of the main aims of the work covered in this thesis has been to investigate the formation of an aperiodic ferromagnetic film, in particular focusing on the deposition of the ferromagnetic element Fe on to quasicrystal surfaces.

The deposition of ferromagnetic elements onto quasicrystal surfaces

The results discussed earlier in Section 2.4.1 certainly provide hope that these substrates may allow the formation of an aperiodic monolayer or thin films of magnetic elements. Several adsorption studies using magnetic adsorbates have previously been carried out.

Weisskopf and coworkers have studied Ni [37] and Co [38] on the 5-fold surface of *i*-Al-Pd-Mn. In both cases they deduce the formation of crystalline domains of an alloy structure aligned along the principal directions of the substrate. In contrast, Smerdon *et al* [39] concluded that in the case of Co adsorbed on the 10-fold surface of *d*-Al-Ni-Co and the 5-fold surface of *i*-Al-Pd-Mn the Co forms rows which are quasiperiodically ordered, but that within the rows crystalline Co is observed. This is consistent with pseudomorphic growth, as observed for Cu adsorption on *i*-Al-Pd-Mn [29, 30, 40]. The discrepancy between these observations could be accounted by the different annealing temperatures used during the surface preparation of *i*-Al-Pd-Mn. High annealing temperatures of 900-1000 K ensure the formation of large atomically flat terraces [8]. In any case, such row structures, whilst of interest with regards to their epitaxy, will not allow the testing of the theoretical predictions of Vedmedenko [41, 42, 43] which consider perfect quasiperiodic systems.

Weisskopf and co-workers have also recently published a study of the adsorption of Fe on *i*-Al-Pd-Mn using secondary electron imaging (SEI), low energy electron diffraction (LEED), and Auger electron spectroscopy (AES) [44]. They find that, up to 4 MLE of Fe, the surface layers do not show structural or magnetic ordering. In this regime it was deduced that Fe atoms diffuse and intermix with the substrate. From 4-8 MLE, Al interdiffusion with the Fe overlayer was found to cause a structural transformation to five-fold domains of a cubic structure. For Fe overlayers greater than 8 MLE, pure Fe was found to grow in five domains having an orientational relationship with the substrate, with some tilting of the domains away from the surface normal.

2.5 Summary

In this chapter, previous work on quasicrystals and quasicrystal surfaces has been described. It is now understood that the the 5-fold surface of *i*-Al-Pd-Mn and the 10-fold surface of *d*-Al-Ni-Co are bulk terminated with some degree of relaxation of the outermost layers. The bulk structure of *d*-Al-Ni-Co can be understood in terms of the model proposed by Ferralis et al [6] and the bulk structure of *i*-Al-Pd-Mn through the geometric model [22]. It has also been possible to form

an overlayer composed of one element which conforms to the aperiodic ordering of the underlying substrate. The formation of a quasicrystalline single element film has has been observed for Sn, Bi and Sb [33, 34]. These results suggest that the formation of a single elemental film composed of a magnetic element may be possible. In the next chapter, surface science characterisation techniques are introduced; the experimental procedure discussed and the UHV chamber described.

Chapter 3

Experimental methods

Most of the experiments described in this thesis involve the characterisation of monolayer films deposited on clean quasicrystal surfaces. This involves the use of advanced surface science techniques in an ultra high vacuum (UHV) environment. In this chapter, these techniques are discussed in depth as well as the sample preparation procedure, thin film deposition and the experimental setup. The main surface science techniques include Auger electron spectroscopy, low energy electron diffraction and scanning tunneling microscopy.

3.1 Vacuum and sample considerations

3.1.1 UHV Considerations

To study the deposition of atoms onto surfaces experiments have to be performed in UHV conditions to keep the sample free from contamination. UHV is defined as the region of pressure between 10^{-7} and 10^{-12} mbar. To obtain such a pressure multi-stage pumping systems are required. A backing pump with dual functionality is required to obtain a medium pressure of 10^{-3} mbar and to assist a turbomolecular pump, which can achieve UHV. Baking of the system is also required to obtain such pressure, as this allows for the desorption of water and other gases from all internal surfaces which may potentially lead to contamination.

Three principal pressure regimes have to be considered in a vacuum chamber; the continuum, the transitional and the molecular flow regime. Continuum flow corresponds to systems with pressures above 10^{-2} mbar where the motion of gas can be compared to a fluid with either turbulent or viscous behaviour. Molecular flow is classed as below 10^{-3} mbar. In this regime the gas molecules are inde-

pendent of each other and non-interacting. The intermediate regime is known as the transitional, and is a mixture of the two types of flows described. The mean free path of the molecules in the system (the average distance traveled by the molecule before interaction with another molecule) varies dramatically with vacuum regime.

The results obtained in UHV were taken under a base pressure of approximately 1×10^{-11} mbar. At these pressures about 1 monolayer of residual gas adsorbs onto the surface every 8 hours. This equates to arrival rates of 3.8×10^{-10} molecules s^{-1}. At this pressure the mean free path between collisions of molecules of the residual gas is about 50,000 Km this avoids interference of probe particles with residue gas molecules. Only at these pressures is the sample kept clean for long enough to do the experiment.

3.1.2 Deposition and coverage estimation

STM experiments were performed in ultra high vacuum (UHV) using an Omicron variable temperature STM. Research grade high purity Fe was deposited from a rod source and Pb from a crucible, using an Omicron EFM-3 electron beam evaporator. The material to be deposited was placed under a filament and a bias is applied between them. Electrons from the filament are accelerated towards the rod or crucible causing sublimation. The desorbed atoms then condense on to the surface of the sample to form a thin film. The sample was kept at room temperature during deposition and measurements. The deposition rate was measured using STM images taken at submonolayer coverage. The coverage was determined using a density slice algorithm [45]. This method allows the user to apply hight limits to the STM image, this allows the percentage of material above the height limit to be calculated as a function of coverage. Post-monolayer coverage was calculated from deposition time. Hence the deposition rate and the coverages are quoted in units of monolayer equivalent (MLE). LEED was used to monitor surface cleanliness and order.

Auger measurements were performed using the same evaporator in a different vacuum system under a base pressure of 2×10^{-10} mbar. A Perkin Elmer double pass cylindrical mirror analyser was used to take the AES data. This system provides higher quality Auger spectra which was used to characterise the growth process as described later. The deposition rate in these AES experiments was determined using the calibrated source and adjusted for the different sample/source distances in both systems, assuming the deposition rate to be inversely related to the square of the distance from the tip of the evaporant rod to the substrate. The deposition rate (atoms/cm^2s) can be calculated using the following equation

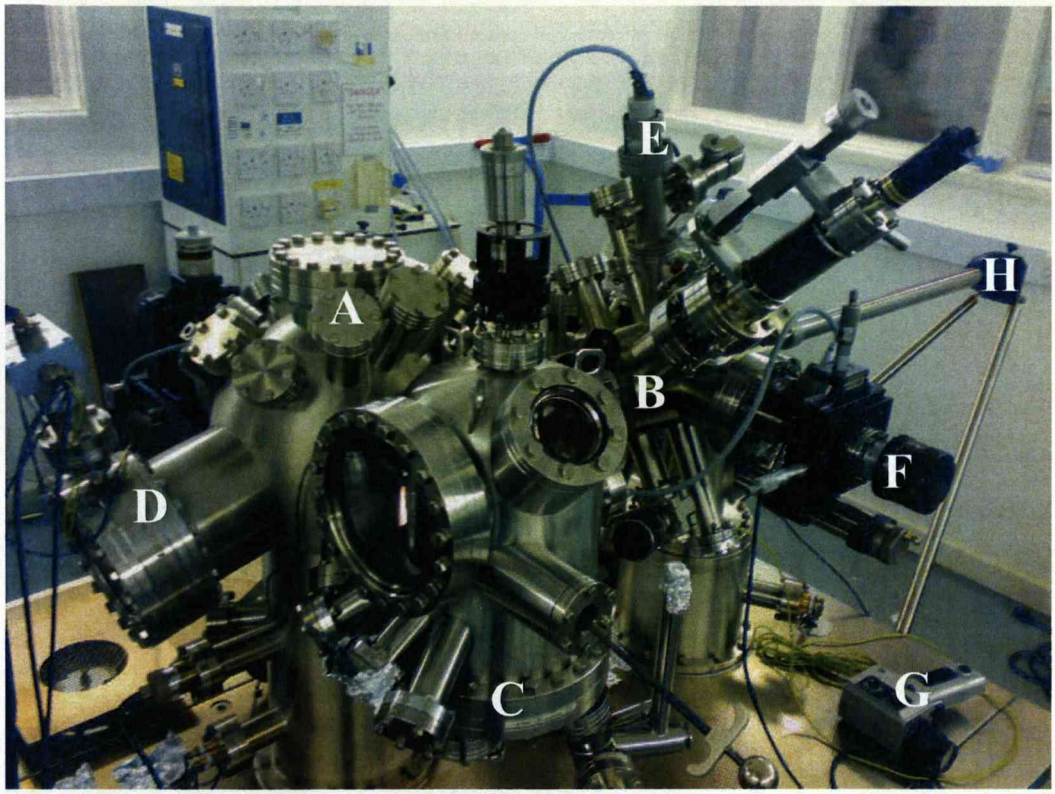

Figure 3.1: Omicron variable temperature STM system; (a) Analysis chamber; (b) Preparation chamber; (c) STM stage; (d) LEED/Auger optics; (e) Ion gun; (f) Manipulator, (g) Pyrometer and (h) Transfer arm.

[46][47];

$$D \simeq 8 \times 10^{24} \frac{pr^2}{L^2\sqrt{MT}} \tag{3.1}$$

where r is the radius of the evaporant bar, L the distance from the tip of the evaporant to the substrate, M the molecular weight of the sample (g), T the temperature of the evaprant (K) and p the vapor pressure (mbar).

3.1.3 Omicron VT-STM system

The Omicron variable temperature STM system pictured in Fig. 3.1 comprises two chambers and a loadlock. The loadlock allows for fast entry of samples and replacement tips into the chamber without having to break vacuum. The preparation chamber contains the equipment necessary to clean the sample and deposit material. This includes an ion gun used to sputter the surface, an electron beam heating facility to anneal the sample, a mass spectrometer to monitor the purity of the sputter gas and an electron beam evaporator used to deposit films.

The analysis chamber contains the apparatus necessary to characterise the surface and the growth of thin films on surfaces. These include an STM for structural characterisation, LEED to probe for atomic order, and use of LEED grids in retarding field mode as an basic AES analyser to determine the cleanliness of the surface (described in 3.2). The sample could be transferred between the different chambers via a transfer arm. This arm is controlled externally through the use of magnets.

3.1.4 SPA-LEED system

The Spot Profile Analysis Low Energy Electron Diffraction (SPA-LEED) system is comprised of one main chamber and a secondary chamber used for storage. The main chamber contains the necessary equipment to prepare samples, deposit films and characterise the surface and growth of thin films on surfaces, using an Omicron SPA-LEED system and Perkin Elmer double pass cylindrical mirror analyser (described in Section 3.2). The SPA-LEED system can be used to extract the width of the diffraction spots, which allows for defects and order within the sample to be analysed under different conditions. For the experiments described in this thesis the SPA-LEED system was used only as a standard LEED system to check for order prior to deposition. The sample was held on a vertical manipulator, moved using an external motor.

3.1.5 Sample production

Samples used in this thesis were produced at Ames laboratory. The Al-Pd-Mn sample was produced using the Bridgman method [48]. This method involves heating a crucible above its melting point then cooling it slowly from one end where a seed crystal is located. A single crystal material can be grown along the length of the container. The Al-Ni-Co sample was produced using the melt decantation method. This method involves adding all the elements present in the alloy to a crucible and heating to 1200°C. This melts the Al into which a small amount of Ni and Co dissolve. The dwell time at this temperature ensures a homogeneous mixture of the melt. The decagonal quasicrystal grows as the mixture is slowly cooled over 150 hours to a temperature of 1000°C. Prior to the growth a second crucible was held upside down above the mixture, partially filled with quartz wool. At 1000°C the crucibles were inverted and any excess Al decanted from the single grain sample.

3.1.6 Surface preparation

The Al-Pd-Mn sample was cut (spark-etched) perpendicular to a 5-fold axis, the Al-Ni-Co sample was cut (spark etched) perpendicular to the 10-fold axes. The samples were polished by hand prior to insertion into the UHV chamber using 6, 1 and 1/4 μm diamond paste. Polishing for 15 minutes per grade was necessary to produce a mirror-like surface. The sample was then placed in an alcohol solution and cleaned in an ultra sonic bath for 20 minutes to remove any remnants of the diamond paste and grease.

To obtain the flat terrace phase required for adsorption studies further cleaning under vacuum conditions is required. Sputtering is necessary to remove contaminates adsorbed onto the surface of the sample. The chamber is filled with a background pressure of Argon gas (99.99 % pure) to 3×10^{-6} mbar. Other inert gases, such as Neon can be used. The purity of the gas is determined using a mass spectrometer.

The ion gun ionises the argon atoms and accelerates them with a specific kinetic energy towards the surface. Bombardment of ions on the surface induces momentum transfer between the ions and the surface atoms, causing surface atoms to be ejected away from the sample. The depletion of surface atoms depends on the atomic mass of the elements present. For samples composed of more than one element the preferential depletion of one compound can be a complication. For the case of Al-Pd-Mn and Al-Ni-Co the lightest element Al is preferentially depleted; its surface concentration after sputtering is reduced with respect to its bulk concentration. To replenish the Al the sample has to be annealed to a temperature approximately two thirds of the melting temperature of the crystal for a total of 20 hours. For Al-Pd-Mn this temperature is 870K, 1070K for Al-Ni-Co. This is done in cycles of a 45 minute sputter followed by a 4 hour anneal (with the exception of the first sputter, this is generally 1.5 hours long). The main purpose of annealing is to the supply the crystal with enough energy for the atoms to rearrange into the most thermodynamically stable state. This allows for the Al deficiency at the surface after sputtering to be corrected for, and the surface to remain bulk terminated. Annealing at these temperatures also allows for the flat terrace phase of Al-Pd-Mn to be observed.

The preferential depletion also depends on the kinetic energy of the ions, controlled using the acceleration voltage and the angle of incidence of the ion beam, which is generally at a normal or grazing angle to the sample. The kinetic energy of ions used is between 1-3 KeV. The emission current from the gun is of the order of 15μA. This is directly related to the drain current. The drain current is a measure of the number of ions impinging on the sample and therefore an indicator of the efficiency of the sputtering procedure.

Figure 3.2: Al-Ni-Co sample mounted on a stainless steel plate.

3.1.7 Sample Mounting

The samples are mounted on a stainless steel or molybdenum plate using either pieces of wire or strips of tantalum foil, as shown in Fig. 3.2. Depending on the required anneal temperature the plate may also have a hole cut into its center to allow for direct heating of the sample, enabling higher annealing temperatures. The eyelet located at the top of the plate enables the sample to be transferred through to different chambers and into STM by the use of either a wobble stick or manipulator, controlled externally through a magnetic arm.

3.2 Auger Electron Spectroscopy

3.2.1 The Auger process

The Auger effect was first discovered by Lise Meitner [49, 50] and reported in the journal Zeitschrift für Physik in 1923, a few years before Pierre Auger made the same discovery [51], which was later named after him. The Auger effect arises from the emission of an electron from the core state, caused by a collision with an incident electron or an energetic photon. This core state can then be filled with an electron from an outer shell, which has an excess energy equivalent to the difference in binding energy between the outer and core state level. This excess energy can be removed by the emission of a photon (the technique used to obtain information about the surface from these photons is known as X-ray

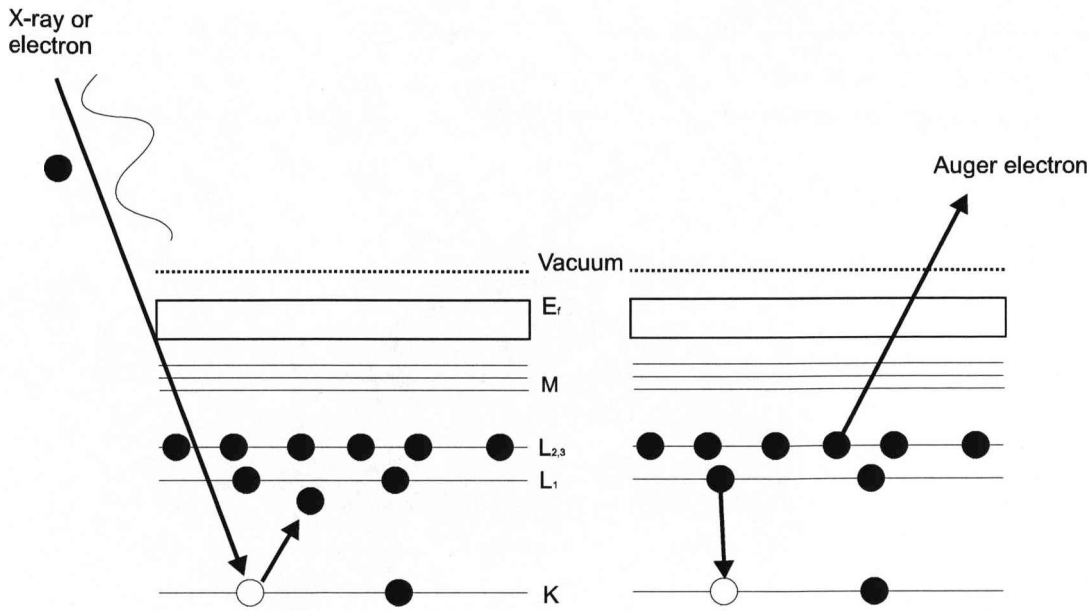

Figure 3.3: Illustration of the Auger process.

fluorescence), or is imparted to a second outer shell electron (termed the Auger electron), which is then ejected from the atom. The Auger process is illustrated in Fig. 3.3. The kinetic energy of the Auger electron is independent of the incident radiation and solely dependent on the binding energies of electrons within the atom. This technique therefore allows the elemental composition of the surface to be identified. The energy of the Auger electron is given by the equation:

$$E_{Augerelectron} = E_{corestate} - (E_{S1} + E_{S2}) \tag{3.2}$$

in which E_{S1} and E_{S2} are the outer state levels.

For light elements with small binding energies the Auger process is more probable than X-ray emission for K-shell initial state holes. For elements with a greater binding energy than calcium the Auger process dominates for initial state holes in other shells. Secondary electrons are also produced. These are electrons which have undergone multiple energy losses by excitation of plasmons and/or interband transitions, and result in a high background of low kinetic energy in the spectra. The Auger peaks are generally quite small and are superimposed on this background. For this reason the differential of the spectrum is usually taken. The height of the differentiated peak is proportional to the area under the undifferentiated peak.

AES was used to check the cleanliness of the sample prior to experiments and to characterise the growth mode, discussed in Sections 2.3 and 3.2.2. The ferromagnetic Fe films were characterised using a Perkin Elmer double pass cylin-

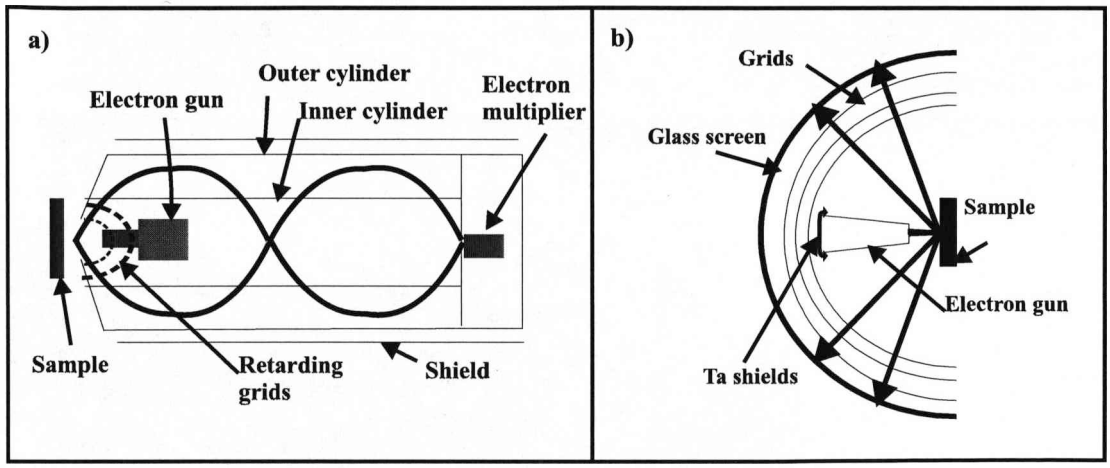

Figure 3.4: A schematic of a) a cylindrical mirror analyser b) a LEED/Auger optics [52].

drical mirror analyser (CMA). The CMA consists of coaxial cylinders which focus particular electron energies at the detector aperture through the application of potentials on the outer and inner cylinders illustrated in Fig. 3.4. The sample cleanliness determined prior to STM experiments was characterised using Auger via a LEED apparatus in retarding field mode. This comprises of a series of concentric spherical retarding grids centered on the sample which filters out inelastically scattered electrons. The electrons are then collected as they impinge on the screen.

3.2.2 Determination of the growth modes using AES

Auger electron spectroscopy can be used to determine the growth mode of the film [53, 54, 55]. A plot of the shape of the Auger signal (AS) versus deposition time can give an indication of the growth mode and hence an indication of the relative strength of the adsorbate-substrate and adsorbate-adsorbate interactions. Illustrated in Fig. 3.5 are a number of schematic AS-t plots for both the adsorbate and substrate signals during the development of films under different growth modes.

Layer-by-layer growth

The formation of a complete adsorbed layer is discernable as a line of data points with a constant gradient. For layer-by-layer growth (Franke-van der Merwe) the data should consist of straight lines with a change of slope after completion of each monolayer with the break points falling on an exponential curve (Fig. 3.5(c)).

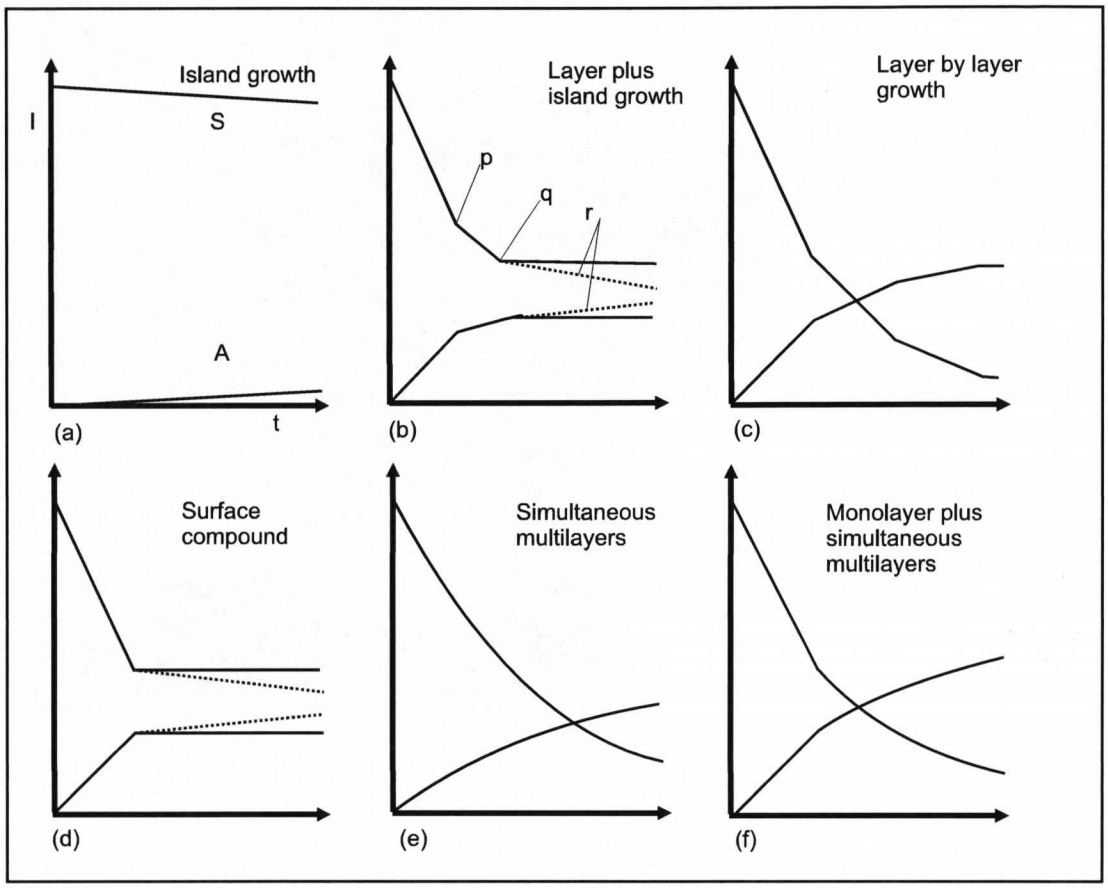

Figure 3.5: AS-t plots (schematic) for the variation of the substrate (S) and adsorbate (A) (condensate) signals during film growth by different modes: (a) Volmer-Weber; (b) Stranski-Krastanov; (this figure also illustrates a pre-monolayer break, p, changing sticking probability at the completion of the first monolayer, q, and variations due to the high densities of small particles, r); (c) Frank van de Merwe; (d) surface compound formation; (e) simultaneous multilayers (exponential variations); (f) monolayer plus simultaneous multilayers. Reprint from [55] and labeled for easy viewing.

The change in the slope after the completion of each monolayer occurs due to the attenuation of the signal from the underlying adsorbate atoms. Each successive adsorbate layer attenuates the signal by the same constant factor. This explains why break points fall on an exponential curve.

For the Franck-van der Merwe (FM) (layer-by-layer) growth [55, 56, 57], the signal from n complete adsorbed layers, $i_A^{(n)}$, is given by

$$i_A^{(n)} = i_A^{\infty}\left[1 - (1 - i_A^1/i_A^{\infty})^n\right] \tag{3.3}$$

where i_A^1 is the signal from the first monolayer and i_A^{∞} is the signal from a thick layer. The attenuation of the signal from the substrate can be described by

$$i_S^{(n)} = \left(\alpha_S^A\right)^n i_S^0 \tag{3.4}$$

where $i_S^{(n)}$ is the signal from the substrate after deposition of n layers, i_S^0 is the signal from the clean substrate and α_S^A is the transmission coefficient for the substrate Auger emission traversing the adsorbate layer.

By ascribing different values of α to different layers the equation can be modified to include non-identical layers. Layers may vary due to changes in density and in structure. Changes in the sticking probability may also occur, especially prior to the completion of the first monolayer, where atoms are more likely to undergo a phase change from the low density dispersed phase to the formation of the dense compact monolayer structure. At this point a 'pre-monolayer' break may be observed in the AS-t plot as shown in Fig. 3.5(d).

The value of α obtained can be related to the inelastic mean free path (IMFP) (λ) of Auger electrons through the expression

$$\lambda = d_m/[(1 - \alpha)cos\beta] \tag{3.5}$$

where d_m is the thickness of the monolayer and β the effective mean acceptance angle of the analyser. The value of cos β is usually taken as 0.74 for both the retarding grid and cylindrical mirror analyser.

3D island growth

Three dimensional island growth (Volmer-Weber mode) results in a much lower emission of adsorbate signal and much larger emission of substrate signal. This is because for the same amount of material, islands or crystallites cover a relatively smaller surface area in comparison to the extended monolayer. The resultant AS-

t plot, shown in Fig. 3.5(a) has a slowly decreasing substrate signal and slowly increasing adsorbate signal until the curve plateaus. AES is not well suited for examining this mode since the signals vary very slowly with deposition quantity. Also there is no monolayer break which can be used for calibration purposes. For isotropic particle growth the signal would follow a $t^{2/3}$ dependance [58].

Layer plus island growth

For the intermediate case of layer plus island growth (Stranski-Krastanov) the formation of a straight line and break is observed, indicative of the completion of the first complete layer, shown in Fig. 3.5(b). After this the trend resembles that observed for 3D island growth, the gradient of which depends on the density of the small particles.

Simultaneous multilayer growth

For simultaneous multilayer growth the surface mobility is negligible. Atoms impinging on the surface stick where they land. As a result of limited surface mobility, there is a rounding of breaks for monolayer coverages, as shown in Fig. 3.5(e). All the breaks that would occur for simple layer-by-layer growth disappear and the signal levels for a given quantity of adsorbate are significantly different. The following equations apply for the growth of the first (equation 3.6) and nth layers (equation 3.7).

$$\theta_1 = 1 - \exp(Jt) \tag{3.6}$$

$$\theta_n = 1 - [1 + Jt + ... + (Jt)^{n-1}/(n-1)!] \exp(-Jt) \tag{3.7}$$

The data points are found to fall on an exponential curve [54, 59],

$$i_A = i_A^{\infty}[1 - \exp -(1 - \alpha_A^A)Jt] \tag{3.8}$$

$$i_S = i_S^0 \exp[-1(1 - \alpha_S^A)Jt] \tag{3.9}$$

where θ is the coverage and J the flux in monolayers per unit time.

Layer plus simultaneous multilayer growth

The formation of a complete monolayer followed by the simultaneous multilayer growth is also possible, the resultant AS-t plot is shown in Fig. 3.5(f). This is intermediate to the two limiting cases of layer-by-layer growth, where surface diffusion is rapid, and simultaneous multilayer growth where diffusion is severely limited. This intermediate case arises when there is a difference in the mobility of the adsorbate atoms impinging on themselves and on the substrate. Diffusion of the adsorbates on the substrate is rapid and allows for the formation of a complete layer after which the mobility decreases to near zero leading to the formation of simultaneous mulitlayers. The result is an AS-t plot with features corresponding to both scenarios.

Alloy formation

The last possible growth mode is surface compound formation where surface atoms diffuse upwards into the adsorbate layer to form a surface alloy. This is the result of a reaction between the surface and adsorbate atoms.

This occurs after the completion of one monolayer, observed as a break point of the AS-t plot. The diffusion of substrate atoms upwards into the adsorbate layer may occur over time. Thus after deposition it may be necessary to take AES spectra at regular time intervals to check for any diffusion.

As a result of intermixing a plateau in the adsorbate and substrate signals should be observed when the main contribution for the substrate falls to zero, and the substrate signal corresponds to surface substrate atoms only (Fig. 3.5(d)).

Dynamic effects can occur also if the adsorbate atoms diffuse into the bulk. This may be hard to observe. One way of doing so would be to take AES after the deposition of a very thin film and at regular intervals thereafter looking for a gradual increase in the substrate signal and a decrease in the adsorbate signal.

3.3 Low Energy Electron Diffraction

William Henry Bragg and William Lawrence Bragg were the first to use a diffraction technique to determine atomic structure. Using X-ray diffraction they determined crystal structures, such as diamond and in the process formalised the interactions of the photons with the crystal via Bragg's law. Both father and son were awarded the Nobel prize in 1915 for their contributions to solving crystal structures.

The theory of electron diffraction was devised by Louis de Broglie in 1924,

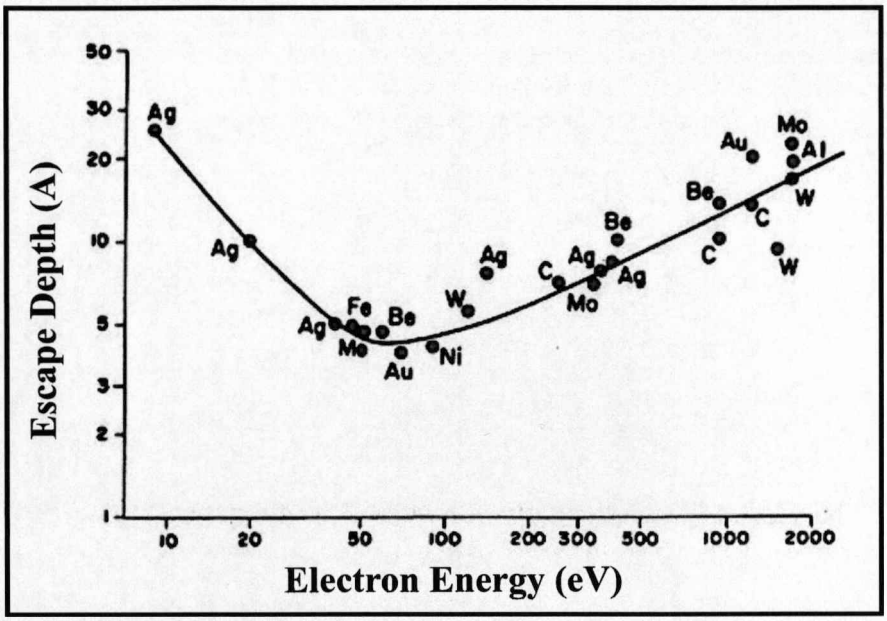

Figure 3.6: Escape depth of electron against energy curve [62].

who asserted that all particles present wave-particle duality. This duality was not observed until Davisson and Germer, working at Bell Laboratories accidently produced Ni(111) microfacets, which lead to the observation of an electron diffraction pattern. The results were published in Nature and in Physical Review in 1927 [60, 61]. One month after, Thompson and Reid published results using electrons with a higher kinetic energy. These experiments revealed the wave property of electrons and opened up the possibility of observing surface atomic order through the use of electrons.

To use electrons to probe surfaces, electrons energies of 1000 eV and less are required as this provides a much larger atomic scattering-cross section and much lower attenuation length in the substrate. The universal curve Fig. 3.6 shows the dependancy of kinetic energy on the escape depth. Two competing physical processes, inelastic and elastic scattering, result in a minimum at near 40 eV, where electrons are almost completely surface sensitive.

Diffraction is observed when the Bragg law is satisfied,

$$n\lambda = 2d\sin\theta \tag{3.10}$$

where λ is the wavelength and $n = (h^2 + k^2 + l^2)^{1/2}$. The scattered beam will have a wavevector $\mathbf{K}'$ [63]. The wavevector is a measure of momentum;

$$|\,\mathbf{K}\,| = 2\pi/\lambda \tag{3.11}$$

In three dimensions conservation of energy then gives

$$\mathbf{K} + \triangle\mathbf{K} = \mathbf{K}' \tag{3.12}$$

Here $\triangle\mathbf{K}$ measures the change in the wavevector and is called the scattering wave vector. The amplitude of the incident and diffracted wavevectors are the same.

$$|\,\mathbf{K}\,| = |\,\mathbf{K}'\,| \tag{3.13}$$

where $\mathbf{K}$ and $\mathbf{K}'$ are respectively the incident and diffracted wavevectors.

$$\triangle\mathbf{K} = \mathbf{G} \tag{3.14}$$

$$\mathbf{K}' = \mathbf{K} + \mathbf{g}_{hkl} \tag{3.15}$$

where the reciprocal lattice vector $\mathbf{g}_{hkl}$ is given by

$$\mathbf{g}_{hkl} = h\mathbf{a}^* + k\mathbf{b}^* + l\mathbf{c}^* \tag{3.16}$$

with $\mathbf{a}^*$, $\mathbf{b}^*$ and $\mathbf{c}^*$ being the primitive translation vectors of the reciprocal lattice.

As $\triangle\mathbf{K} = \mathbf{G}$, or $\mathbf{K} + \mathbf{G} = \mathbf{K}'$, the diffraction condition is written as [10]

$$2\mathbf{k} \cdot \mathbf{G} + G^2 = 0 \tag{3.17}$$

This is the central result of the theory of elastic scattering of waves in a periodic lattice. If $\mathbf{G}$ is a reciprocal lattice vector, so is $-\mathbf{G}$, and with this substitute we can write Eqn. 3.17 as

$$2\mathbf{k} \cdot \mathbf{G} = G^2 \tag{3.18}$$

This is another statement of the Bragg condition.

An Ewald sphere construction (or sphere of reflection) can be used to describe the diffraction of a beam of electrons impinging on an ordered array of atoms, if the diffraction is limited to the surface only. The Ewald sphere is a sphere of radius $1/\lambda$ which passes through the origin (O) of reciprocal space. As the wavelength changes the radius of the sphere changes. Diffraction occurs when the Ewald sphere cuts the reciprocal lattice rods. The incident direction is along the radius of the sphere to the intercepting lattice rod (IO). The diffraction condition is satisfied when the diffraction vector OH = IH - IO. If other reciprocal lattice

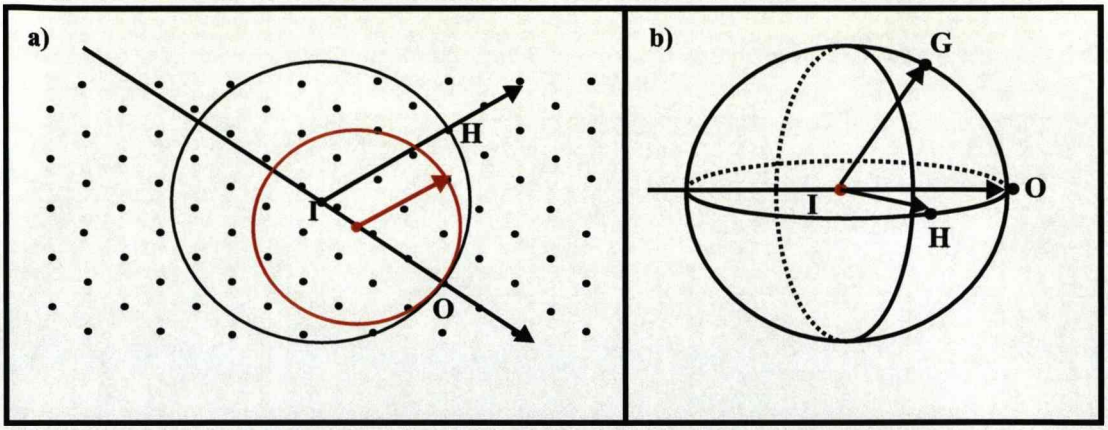

Figure 3.7: a) A schematic to show an Ewald sphere (shown in 2D) for two wavelengths (radius $1/\lambda$), in reciprocal space, b) The Ewald sphere in 3D.

nodes i.e. G, lie on the Ewald sphere, there will also be a reflection along IG. This construction is known as the Ewald sphere construction, illustrated in Fig. 3.7. Quasicrystals can be thought of as having an infinite unit cell and hence reciprocal space is infinity dense. However only the more intense reflections will appear as diffraction spots.

3.4 Scanning Tunneling Microscopy

3.4.1 Scanning

Scanning Tunneling Microscopy (STM) can be used to produce a 2D plot of the joint local density of states at a surface (LDOS) and of the tip. The LDOS is a measure of the electronic structure resulting from the atomic arrangement. This plot can then be used to obtain information about the surface topography.

Scanning tunneling microscopy was invented in 1981 by Gerd Binning and Heinrich Röhrer at IBM Zurich, who five years later were awarded the Nobel prize in physics for its invention. STM was the first instrument used to obtain atomic resolution from a surface.

Atomic resolution can be obtained through the use of an atomically sharp, conducting tip. The tip is brought into close contact with a conducting sample under an applied voltage. At a tip/sample separation of 10 $\AA$, the wavefunctions of the sample and the tip start to overlap. The wavefunction is related to the probability of finding an electron. Therefore as the wavefunctions overlap the probability of electrons tunneling across the barrier increases shown in Fig. 3.8. The tunneling current varies exponentially with tip/sample separation.

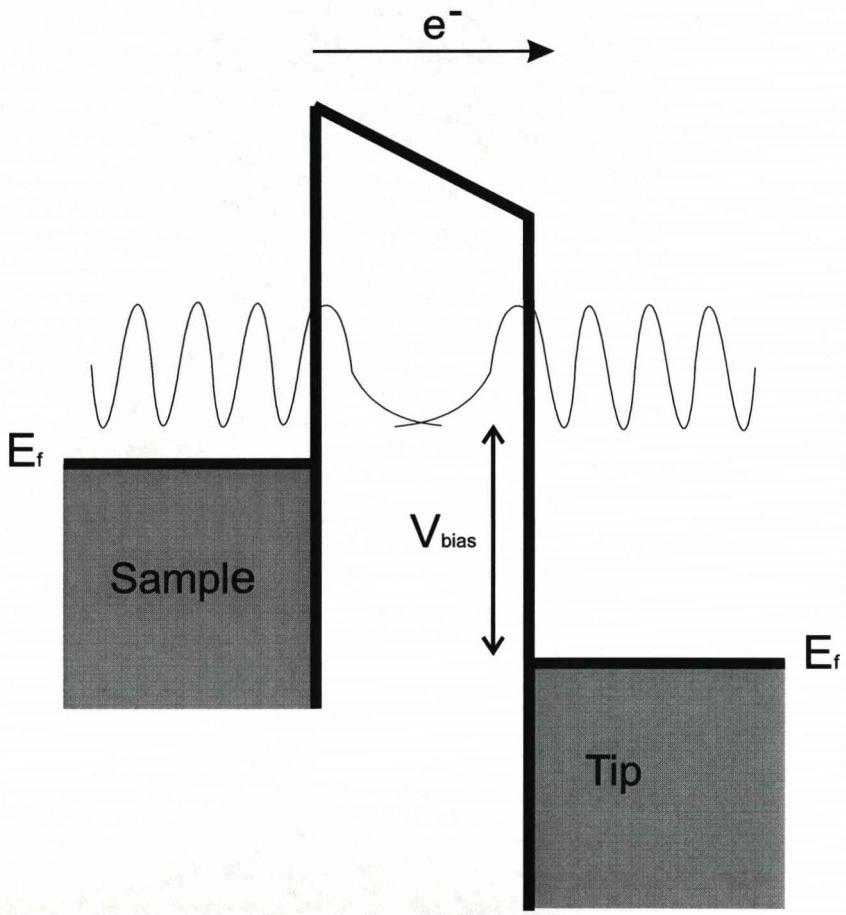

Figure 3.8: Tunneling of electrons from the sample to tip (and vice versa) occurs only when the wavefunctions of the sample and tip overlap.

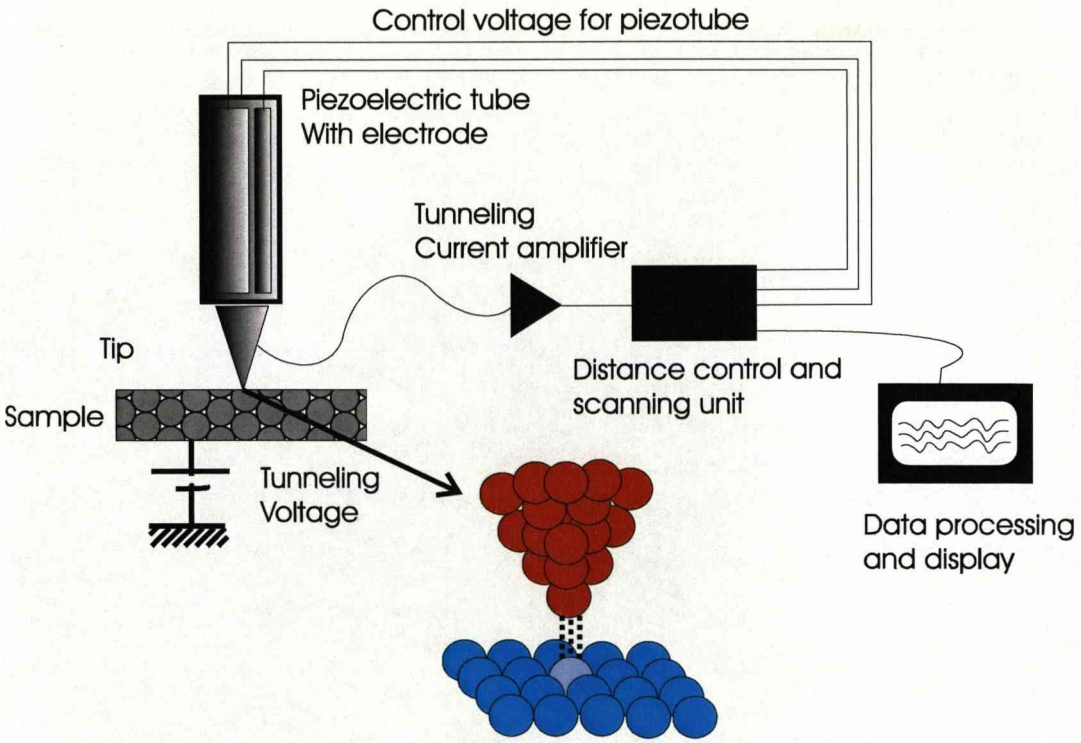

Figure 3.9: A schematic of a scanning tunneling microscope.

$$J_T \propto e^{A\phi^{0.5}S} \tag{3.19}$$

Where J_T is the current, ϕ is the average barrier height, S the distance between the tip and sample, and A is a constant equal to 1.025 $\text{Å}^{-1}\text{eV}^{(-1/2)}$ for vacuum tunneling [64].

Two modes of operation can be employed to produce a 2D image of the surface, constant height mode and constant current mode. During constant height mode, the tip/sample separation is kept constant and the tunneling current measured. This then maps out the topography of the surface. This mode makes scanning extremely fast, however a smooth, flat sample is required. Quasicrystals surfaces comprise of steps and terraces which makes the probablity of a tip crash more likely. As a result constant current mode is the preferred scanning mode. This reduces the risk of a tip crash by ensuring a constant tunneling current is maintained by adjustment of the tip/sample separation. The motion of the scanner constitutes the data set which when linked to a computer reveals the local surface topography, illustrated in Fig. 3.9. The tunneling current is dependent on the electron local density of states at the surface. This is the number of filled or unfilled electron states near the Fermi level, with an energy range determined by the bias voltage.

The tip is mounted on a piezoelectric drive. Piezoelectric materials are polycrystalline ceramics. Each crystal in these materials possesses its own electric dipole moment. The aligning of these dipole moments allows for a change in the dimensions of the ceramic in response to an applied voltage. A tube scanner is employed in the VT STM system. The tube is constructed from a lead zirconate titanate ceramic (PZT), metallised on the outer and inner surfaces. The tube is polled in the radial direction. The outside metal coating is sectioned into four quadrants. The inner metal coating is connected to the z electrode, and the two neighboring quadrants are connected to the varying x, y voltages, respectfully. The remaining two quadrants are connected to a certain dc voltage to improve linearity. The tip is attached to the center of one of the dc quadrants [64].

The z electrode allows the tip to approach the surface, while the x and y electrodes allow the tip to raster scan across the surface. The tip is brought into close contact with the surface through a feedback loop, allowing the tip to approach the surface until a tunneling current is detected.

A photograph of the STM head is shown in Fig. 3.10. The apparatus consists of a pre-amplifier, which is connected to the tip and allows the current to be measured. Four springs keep the STM in suspension and allow the stage to be retracted prior to scanning to allow for the damping system to be brought into position. Damping of external vibrations is maintained through a series of copper fins placed between magnets. These eddy-current damping systems are used to attenuate any vertical and rotational motion of the suspended instrument.

3.4.2 Tip preparation

An atomically sharp tip is required in order to obtain atomic resolution of the surface. If the tip is not atomically sharp a number of artifacts may occur whilst imaging. Such artifacts include double or multiple tips (illustrated in Fig. 3.11, or shadowing. If the tip is not sharp then tip convolution will occur, this makes features appear larger than they actually are. The structure of the tip plays a major role in determining the spatial resolution of the surface.

STM tips can be made from different materials. In this work a W tip was used. Tungsten wire, 0.5 mm in diameter was electrochemically etched to produce a sharp tip. A sharp tip can be produced by cramping it firmly in a tip holder, then suspending it over a stainless steel plate and inserting through a hole in the plate. The tip holder is connected to the negative electrode and plate to the positive electrode. A solution of hydroxide pellets dissolved in water is used to provide the electrolyte by filling the gap between the plate and the wire with the solution. The solution must constantly be replenished. The surface tension of the

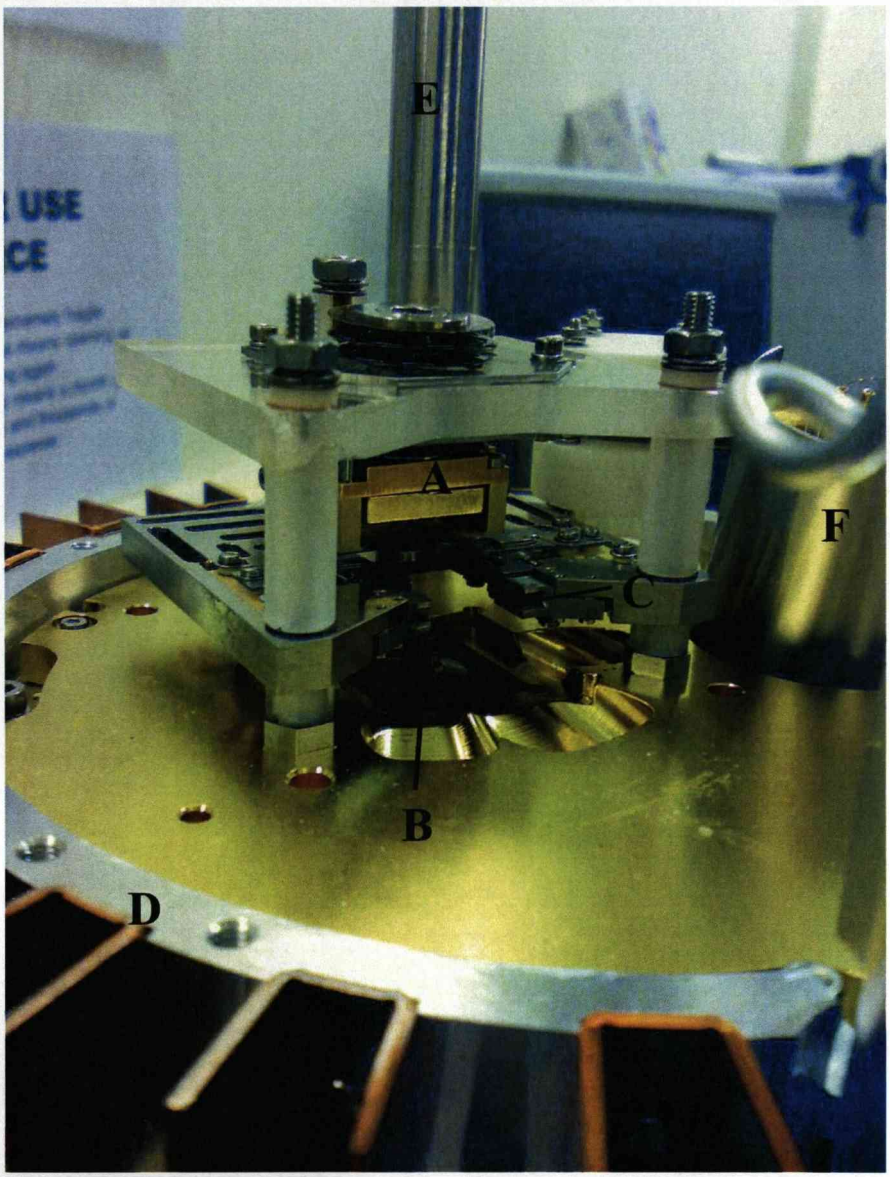

Figure 3.10: A photograph taken of the Omicron variable temperature STM head; (a) Cooling plate; (b) Tip; (c) Sample holder; (d) Copper fins; (e) Spring and (f) Electronics.

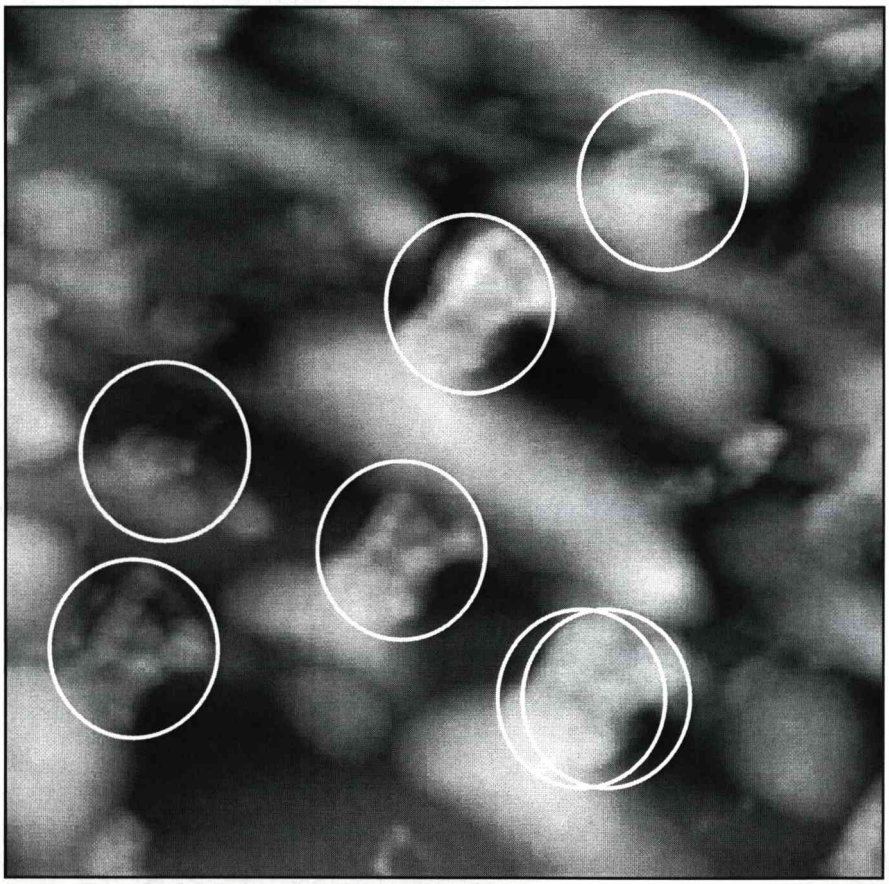

Figure 3.11: An example of a multiple tip, where the tip is imaging the same object twice.

solution ensures the electrolyte remains suspended across the hole. A bias voltage of approximately 7V is applied. This allows for the electrochemical etching of the tungsten wire to produce an atomically sharp tip.

Further preparation of the tip may be required whilst scanning to sharpen the tip and remove any contamination adsorbed the end of the tip which may affect the quality of the STM image. The tip can be sharpened by applying voltage pulses of up to 10V or increasing the scanning speed for short periods of time. The tip can be sputtered or annealed to remove large amounts of contamination. As a last resort the tip can be z-pulsed, which involves crashing the tip into the surface.

3.5 Scanning Tunneling Spectroscopy (STS)

STS has its origins in some of the earliest STM work of Binning *et al*, who found evidence for voltage-dependent changes in the appearance of some atoms within the Si(111)-(7x7) unit cell and correctly noted that such effects might arise from tunneling through discrete electronic states of the sample. The clear differences in the apparent height of many of the atoms observed when imaging over a range of potentials, arise from the energy-depended changes in the density of states of the sample.

Spectroscopic information can be obtained through a number of means, the simplest method is voltage-dependant STM imaging. Where STM is taken over a range of applied voltages and the results compared. This however, is a time consuming technique. The method used in the Pb/AlPdMn experiment (section 4) allows local I-V measurements to be obtained over a wide range of voltages, simultaneously while scanning. Both data sets can be obtained simultaneously by slowly scanning the tip and allowing the sample-and-hold circuit to interrupt the feedback loop for a few microseconds, to maintain tip position while the voltage is ramped for the I-V curve. By rapidly acquiring the I-V curves while slowly scanning, both the electronic structure characteristic of the surface and the surface topography can be measured at each location over a 2D raster scan. STS can be used to probe the electronic structure of the surface atoms, identifying occupied and unoccupied energy levels.

The I-V spectra taken from a quasicrystal shows a distinct feature termed the pseudo-gap. This is a decrease in the density of states at the Fermi level (shown in Section 4, Fig. 4.4(a)).

Chapter 4

Pb deposition onto AlPdMn in UHV condition

Over the past decade, the Al-Pd-Mn quasicrystal has been the subject of intense studies, summarised in Section 2.2. The quasicrystal structure (bulk and surface) is now well understood but key questions remain unanswered; is the reduction in the electronic density of states at the Fermi level (pseudo-gap) due to the chemical complexity or to the quasiperiodicity of the surface. To address this issue, one route is first to use an aperiodic substrate as a template to grow a mono-element thin film and then probe its electronic structure *in situ* by surface sensitive techniques.

A two-dimensional quasiperiodic Pb monolayer has been successfully grown on the Al-Pd-Mn surface. The results are presented below.

4.1 Experimental details

In this study we have applied the techniques of STM and STS, to the study of the Pb/*i*-Al-Pd-Mn system. The experiments were performed in the VT-STM system. The sample preparation and experimental details are discussed in section 3.1. Lead was evaporated by e-beam bombardment of material held in a crucible, using a flux set to achieve a deposition rate of 2.5 x 10^{-3} MLE s^{-1} under a base pressure of 1.5×10^{-10} mbar.

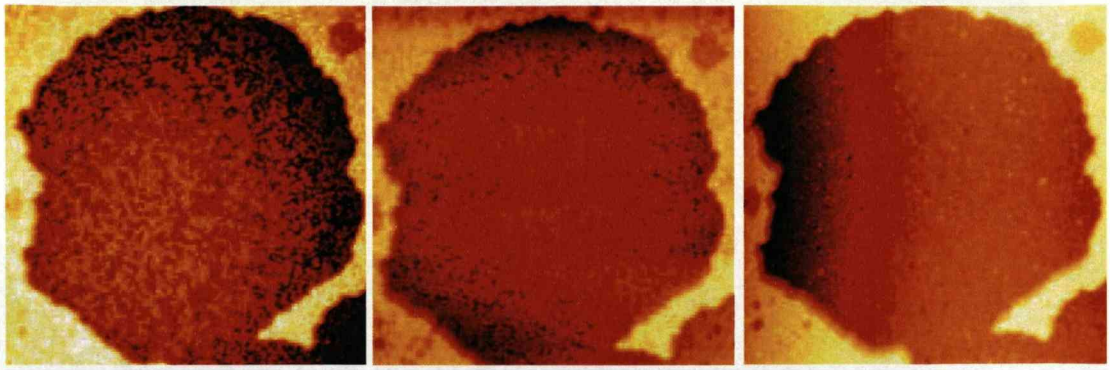

Figure 4.1: 150 nm × 150 nm STM image of the surface after the deposition of (a) 0.3 MLE, (b) 0.7 MLE and (c) 1 MLE of Pb.

4.2 Results

Figure 4.1 shows the adsorption of Pb on the surface of Al-Pd-Mn at increasing coverages up to 1 MLE. The Pb was deposited *in situ*, enabling the same part of the surface to be scanned at different coverages. Upon adsorption the Pb atoms diffuse across the surface and form islands. At increasing coverage the 2D islands form as an interconnecting network of islands until a fully complete monolayer is observed, after which the sticking probability of the Pb is reduced to zero and the formation of multilayers through STM is not observed.

Figure 4.2(a) shows an STM images of the near complete Pb film. The self-similar aperiodic pattern can easily be observed. The pentagonal islands are the most striking features, with additional "glue" atoms filling the interstices within the network. To make the aperiodicity of the surface clearer the image has been filtered using a Fast Fourier transform and a P1 type Penrose tiling superimposed (Fig. 4.2(b)). Figure 4.3 shows a high resolution 15 nm x 15 nm STM image of the clean surface and the 1ML Pb film. An FFT of each has been inserted to show order. It should be noted that the insert in Fig. 4.3(b) has been enlarged to make the rings more visible to the reader, it therefore cannot be directly compared with the FFT taken from the clean surface and is included only to show order. The features from both surfaces compare well, the inflated nature of the pentagonal features from the Pb film are easily comparable with those from the clean surface. This is confirmed through the application of a FFT of the STM images. The distance between consecutive rings in reciprocal space of the film are τ^{-1} scaled in comparison to the clean surface, confirming the inflation of the film observed in real space.

STS measurements were also collected on the annealed Pb monolayer and on the Al-Pd-Mn surface, see Fig 4.4. Annealing does not change the structure of the film, it only reduces the number of structural defects. I(V) curves were col-

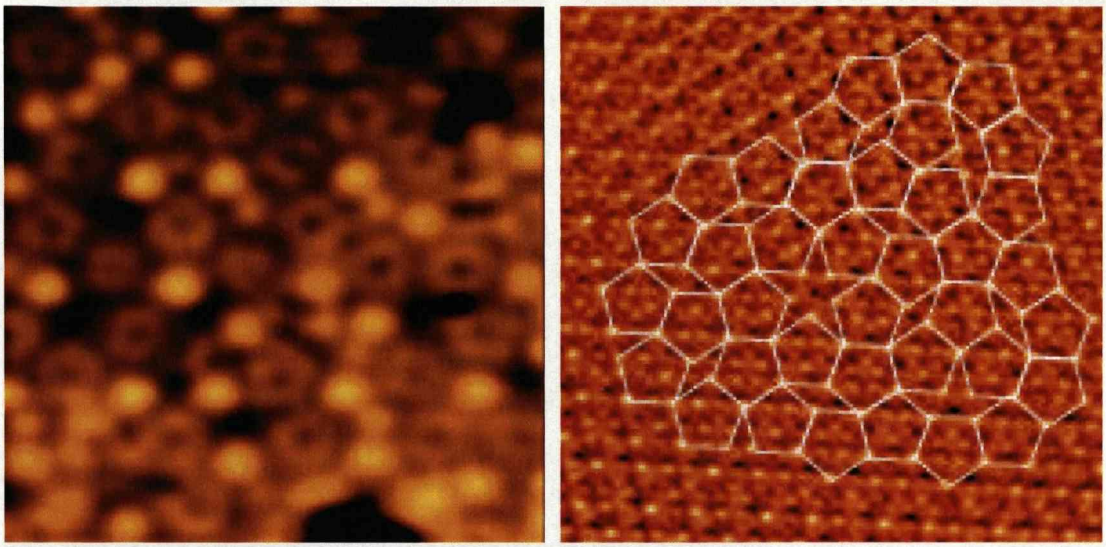

Figure 4.2: STM image of the near complete (0.8 ML) and complete Pb film at (a) 17 nm × 17 nm; and (b) 40 nm × 40 nm enhanced using an FFT filter, superimposed with a Penrose tiling.

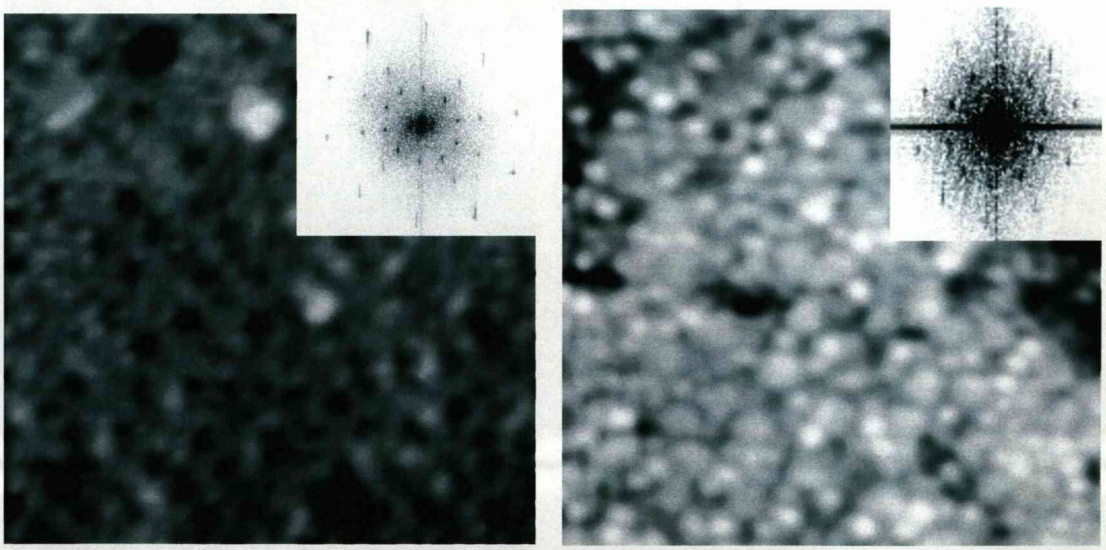

Figure 4.3: 15 nm × 15 nm STM image of (a) the clean surface of Al-Pd-Mn and (b) 0.8 ML Pb film, both including FFT inserts.

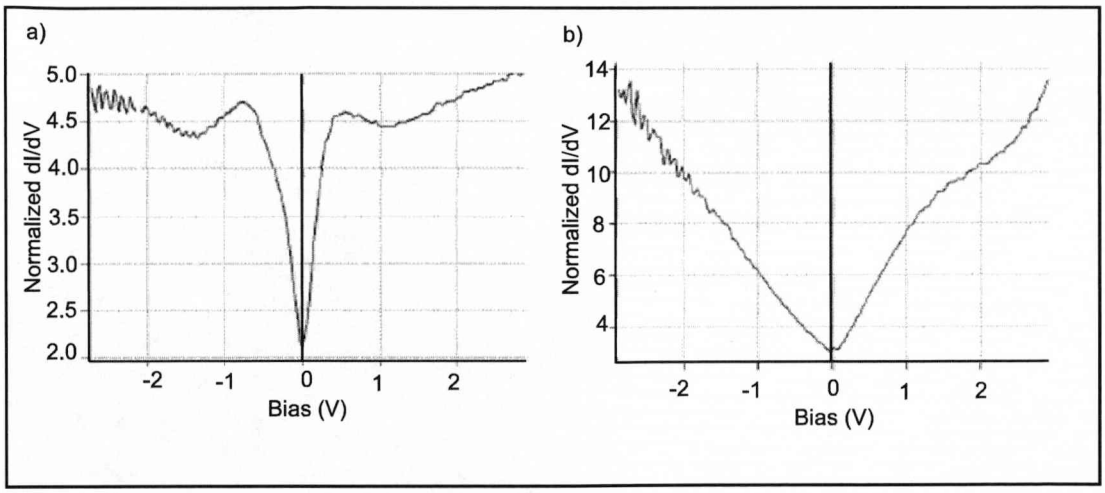

Figure 4.4: STS spectra taken between +3 and -3 eV for (a) the clean surface and (b) Pb film.

lected in a grid-like manner on different atomic local configurations. Normalised dI/dV spectra represent on average over 10^4 I(V) curves before being differentiated numerically. A pseudo-gap is observed in the DOS at the fermi level for the Pb as shown in Fig 4.4(b). These results indicate that the formation of the pseudo-gap is due to the aperiodicity of the film and not its chemical complexity. The pseudo-gap appears larger on the Pb film than on the clean surface. The STS spectra for Pb(111) does not show a decrease in density of states at the Fermi level [65].

4.3 Further work

The results discussed were obtained in collaboration with J. Ledieu and V. Fournée from CNRS, Nancy, who went on to extensively investigate the properties of the film using other techniques such as LEED, Auger and UPS. They observed the growth behavior of Pb on Al-Pd-Mn to be highly reproducible over a temperatures rang from 57 K to 653 K and by varying the deposition rate over orders of magnitude leading to identical results.

Complimentary to LEED, Auger and UPS they also carried out more STM imaging of the film and obtained high resolution images of the Pb film which can be used to explain how the aperioidic Pb evolves (Fig. 4.5). This image shows the formation of pentagonal islands, each identical in size and facing the same orientation on successive terraces. These islands form an interconnecting network, the small pentagons islands being the basic building block of this film. At higher coverages the pentagon islands converge at these vertices to form even

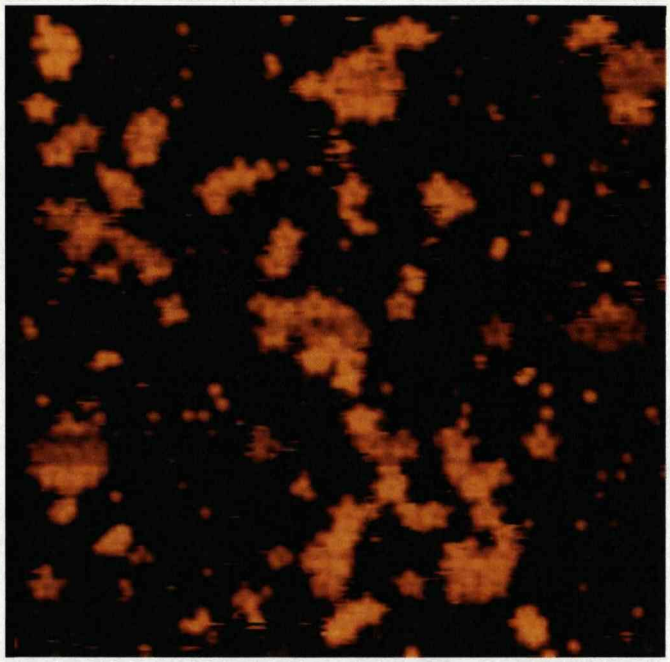

Figure 4.5: 17 nm ×17 nm STM image after the deposition of 0.2 MLE of Pb. Taken by J Ledieu and V Fournée, CNRS Nancy.

larger pentagon islands.

Low energy electron diffraction was used to confirm the Pb layer is inflated by a factor τ with respect to the clean surface. The AES results taken during the evolution of the Pb film confirm the observation made by STM, that the sticking probability of the Pb is reduced to zero after the completion of the first monolayer therefore preventing the formation of the second layer. UPS was used as a complimentary technique to STS to probe the electronic structure of the film. Ledieu *et al* conclude from these results that the decrease in spectral intensity at the Fermi level in the DOS for a quasicrystal, corresponding to the presence of a psuedo-gap [66] occurs due to the quasiperiodic ordering of the atoms and not the chemical complexity [67].

4.4 Discussion

Similar pentagonal islands have been observed at low coverage by Cai *at al* [32]. These islands, termed starfish were seen when dosing Al onto the Al-Cu-Fe quasicrystal. The starfish islands exhibit a comparable size and orientation however they do not develop into a quasiperiodic structure. The formation of Al and Pb clusters are obtained regardless of deposition rate. This is characteristic of an heterogenous nucleation process at specific quasilattice trap sites [32][68]. The

roughening of the Al film is explained by a possible combination of a high interfacial energy of the system and a lower surface energy of the substrate compared with the adatoms. Aluminium adsorbates landing on the already formed starfish are stabilised at that position while Al adatoms adsorbed onto the Al-Cu-Fe surface will diffuse across the terraces, after which they are either trapped at a specific nucleation site or if all the sites are occupied, diffuse uphill and adsorb on the starfish.

In the case of Pb, two phenomena may explain the two-dimensional aperiodic growth mode. First, the surface energy of Pb (0.3 JM^{-2}) is a lot lower than Al (1.2 JM^{-2}) [69], the main constituent of the top most layer of the quasicrystal. Second, our observations show that adatoms hitting the clean surface stick while adatoms landing on the already adsorbed monolayer Pb film tend to diffuse down hill or bounce back into the gas phase.

The decrease in sticking coefficient after one monolayer can only be attributed at this stage to the incoming Pb adatoms not losing enough of their kinetic energy to the Pb monolayer through lattice phonon excitations. A shallow potential well of impinging Pb adatoms on the Pb monolayer could account for a short stay time and rapid desorption. This however implies an adsorption process with weak van der Waals type bonding, with binding energies of typical rare gas species adsorbed onto metal surfaces. Alternatively, Pb adatoms in a shallow precursor state with an activation energy for chemisorption higher than the desorption energy may explain the non-sticking behaviour. However a physisorption process for Pb on a Pb monolayer is not applicable in this case and a high phonon frequency is the only reasonable explanation to our observation.

4.5 Conclusion

A quasiperiodic two-dimensional single element Pb film has been grown successfully on the 5-fold surface of the Al-Pd-Mn quasicrystal. The skeleton of this film corresponds to a network of pentagonal islands adsorbed quasiperiodically on the substrate. Only 1 ML of Pb is permitted to adsorb due to energy constraints. The drastic decrease in the sticking coefficient is attributed to high surface phonon frequencies. This system of reduced complexity allows for the first time the determination of the origin of the pseudo-gap and its correlation to the quasiperiodic structure.

Chapter 5

Fe deposition onto Al-Pd-Mn in UHV condition

5.1 Introduction

As discussed earlier in Section 2.4.2, one area of interest is the growth of magnetic films on quasicrystal surfaces. Magnetism in bulk quasicrystals has been studied extensively, but strong magnetic effects are not observed [70]. In an icosahedral quasicrystal, such as $Al_{70}Pd_{21}Mn_9$, the magnetic effects are dispersed in a non-magnetic framework which leads to very effective reduction of magnetic interactions. On the other hand, there have been several theoretical studies of quasiperiodic magnetic systems which predict unusual magnetic structures [41, 42, 43]. Growth of monolayers and thin films of magnetic elements on quasicrystal surfaces offer the possibility of forming such systems, provided that the magnetic elements order quasiperiodically on the surface.

Iron was subsequently deposited on the surface of Al-Pd-Mn. The results are presented below.

5.2 Experimental details

In the study we have applied the technique of scanning tunnelling microscopy (STM), in conjunction with LEED and AES, to the study of the Fe/*i*-Al-Pd-Mn system. STM provides spatial information complementary to that obtained by Weisskopf *et al.* using SEI [44] (Section 2.4.2). The sample preparation and experimental details are discussed in Section 3.1.

STM was carried out in the VT-STM system under a pressure of 1.5×10^{-10} mbar. The deposition rate during the STM experiments was $5.5 \pm 0.8 \times10^{-3}$ MLE s^{-1}, and the error on the coverages is estimated to be $\pm16\%$. The error is the standard deviation of a number of measurements taken over a large area. LEED was used to monitor surface order. Auger measurements were performed using the same evaporation source in the SPALEED system system under a base pressure of 2×10^{-10} mbar, using a Perkin Elmer double pass cylindrical mirror analyser. The deposition rate in these AES experiments was determined using the calibrated source and adjusted for the different sample/source distances in both systems, assuming the deposition rate to be inversely related to the square of the distance from the tip of the evaporant rod to the substrate. For the AES study the deposition rate was calculated to be $2.5 \pm 0.3\times10^{-3}$ MLE s^{-1}.

5.3 Results

5.3.1 STM and LEED

Figure 5.1(a) shows a high resolution STM image of the clean surface, demonstrating that large flat terraces were present. The inset shows a Fast Fourier Transform (FFT) of this image which shows three rings of ten spots. The spots are indicative of 5-fold symmetry from a well-ordered surface [8]. The bulk and surface structure are described in Section 2.2.

Figure 5.1(b-d) shows the development of the growth process at sub-MLE coverages of Fe. At a coverage of 0.13 MLE, shown in Fig. 5.1(b), islands of average apparent diameter 1.35 ± 0.25 nm are formed. Further deposition increases the density of these islands, until they appear to merge and form a nearly continuous overlayer at about 0.7 MLE. At these sub-monolayer coverages, the apparent height of the islands is of order 0.16 ± 0.03 nm, consistent with single atom height. However the formation of a second layer is observed to begin just prior to the completion of the first monolayer.

Figure 5.2(a-c) shows the continuation of the growth process above single MLE coverage. At a coverage of 1.3 MLE (Fig. 5.2(a)), the second layer is forming as an interconnected group of islands. This trend continues at 2.6 MLE (Fig. 5.2(b)), although the simultaneous growth of the fourth layer has already begun at this coverage. No LEED pattern was observed in the film up to this point. At higher coverages there is a transition to the growth of multilayer islands - so-called 'wedding cake' structures [71, 72]. This is shown in Fig. 5.2(c) for a coverage of 4 MLE.

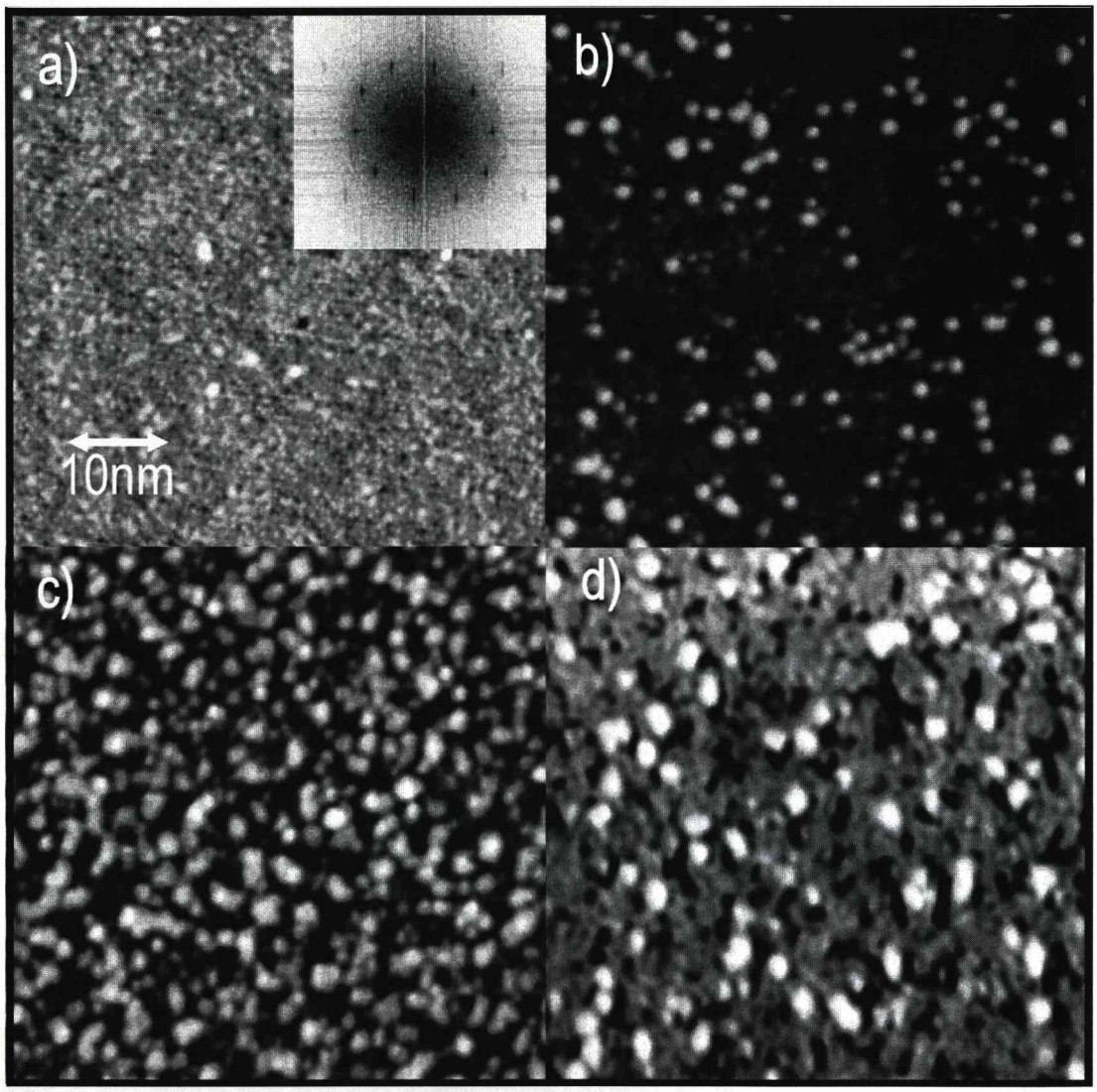

Figure 5.1: 50 nm x 50 nm room temperature STM images of (a): the clean five-fold surface of Al-Pd-Mn. The inset shows the fast Fourier transform of this image. (b-d): the surface after the deposition of 0.13 MLE, 0.3 MLE, and 0.7 MLE of Fe respectively.

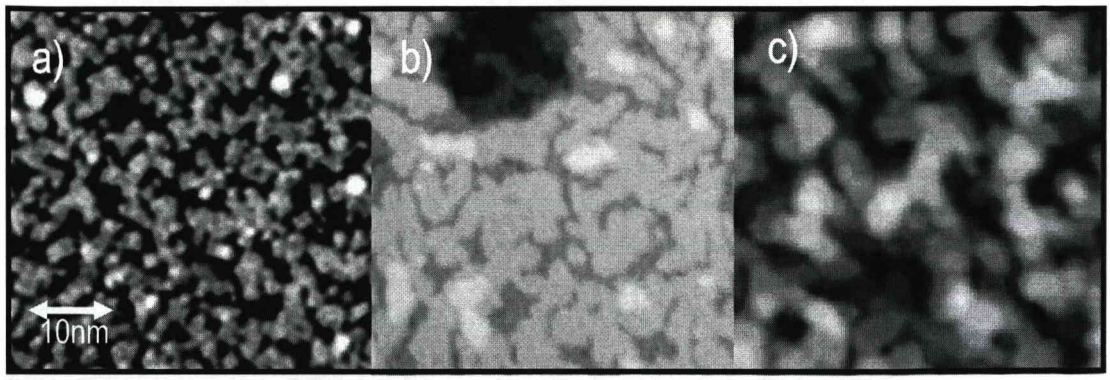

Figure 5.2: (a)-(c): 50 nm × 50 nm STM images of the surface after Fe deposition of 1.3 MLE, 2.6 MLE and 4 MLE.

Figure 5.3: Surface after deposition of 5.4 MLE of Fe: (a) STM image, 100nm ×100 nm; (b) Enhancement of boxed 50 nm × 50 nm section of (a) using a Sobel edge detection filter; (c) LEED pattern obtained at a beam energy of 140 eV.

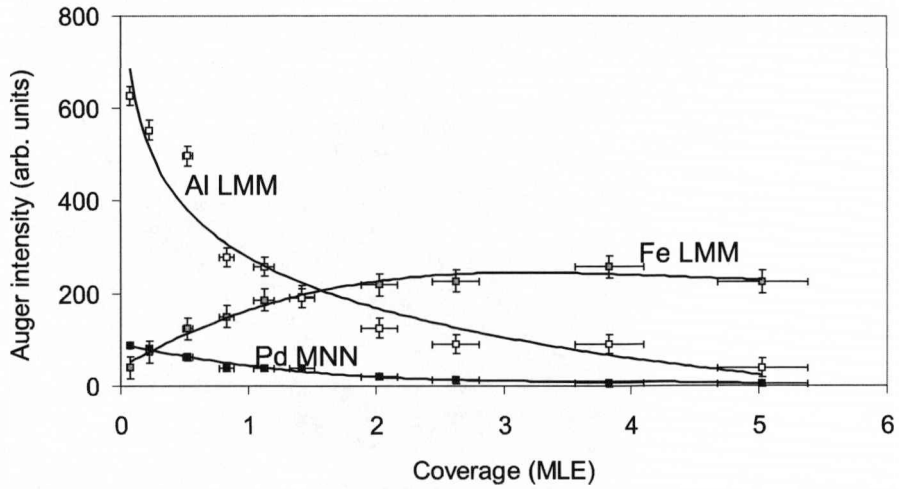

Figure 5.4: A plot of the Al LMM (68 eV), Pd MNN (330 eV) and Fe LMM (651 eV) Auger signals as a function of increasing coverage. The substrate signals are fitted with exponentials while the Fe signal is fitted with a logarithmic function - see text for details.

The multilayer islands have a well-defined wedding-cake structure. Fig. 5.3(a) shows a 100 nm x 100 nm overview image of this structure at a coverage of 5.3 MLE. The islands are more ordered, evidenced by a preference for straight edges. Fig. 5.3(b) shows the boxed area of Fig. 5.3(a) (50 nm $\times$ 50 nm) after image processing using a Sobel edge detection analysis routine [73]. This procedure enhances the step edges making it easier to detect layer boundaries and hence to measure step heights. A monatomic step height of 0.21 $\pm$ 0.02 nm was measured using both line profile and histogram analyses of several images. An average island area of 113 nm^2 was measured using a thresholding analysis. Fig. 5.3(c) shows the LEED pattern observed at this coverage at a beam energy of 140 eV. A single ring of ten spots is observed which is consistent with five cubic orientations rotated by 72° from each other. The average step height and the LEED pattern are consistent with the presence of an Fe(110) surface.

5.3.2 AES

The growth process was also characterised using AES. Fig. 5.4 shows the magnitude of the peak-to-peak Auger signal for the Al LMM (68 eV), Pd MNN (330 eV) and Fe LMM (651 eV) peaks as a function of Fe coverage. The Mn LMM peaks are too weak to be accurately measured due to the low amount of Mn in

the bulk, and the fact that the two topmost layers are known to be Al-rich [25].

There is a large amount of surface science literature on the interpretation of growth curves using AES as described in Section 3.2.2. The various known growth modes display qualitative features which can be compared with the data in Fig. 5.4. On this basis the Auger data rule out Volmer-Weber (VW) (island) or Stranski-Krastonov (SK) (single layer plus islands) growth. Surface compound formation (see Fig. 2 of ref. [55]) is also inconsistent with the data, indicating that Fe does not intermix with the substrate. This is the most important conclusion from the AES analysis.

The remaining growth modes are Franck-van der Merwe (FM) (layer-by-layer) growth, simultaneous monolayers (SM) and monolayer plus simultaneous multilayers (MSM). In order for these growth modes to be uniquely distinguished with AES, a high density of data points is needed. This is because for FM growth the data should consist of straight lines with a change of slope after completion of each monolayer with the break points falling on an exponential curve. For SM growth all points should fall on an exponential curve. For MSM growth, a straight line is found followed by an exponential curve. Unfortunately our data does not have a sufficiently number of data points to make these distinctions, as the time required for the AES measurement after each deposition meant that only a small number of measurements could be made before contamination ensued. However the STM data rule out monolayer plus simultaneous multilayer (MSM) and simultaneous multilayers (SM) growth for the first three monolayers.

Therefore the data for the first three monolayers were analysed for the Franck-van der Merwe (FM) (layer-by-layer) growth [55, 56, 57] using the Eqn. 3.3 and 3.4. The values for $i_A^{(n)}$ and $i_S^{(n)}$ were found by fitting trend-lines to the data which are shown in Fig. 5.4. For the substrate Al and Pd signals, the best fit curves were exponentials. This is not surprising, as in any case the break-points are expected to follow this trend [55]. For the adsorbate Fe signal the best fit curve was logarithmic rather than exponential; this may be because of a different inelastic mean free path for the higher energy Fe LMM Auger electrons [55].

These fits allow the values of the Auger intensities after completion of the first three layers to be estimated. The value of the Auger intensity i_A^∞ was estimated as the saturated value from Fig. 5.4. Then, applying Eqn. 3.3, we find that the calculated and measured signals for i_A^2 and i_A^3 are in agreement within experimental error. Using Eqn. 3.4 and the values i_S^n from Fig. 5.4 for both Al and Pd, we find transmission coefficients $\alpha_S^A = 0.35 \pm 0.03$ for Al and $\alpha_S^A = 0.48 \pm 0.05$ for Pd.

5.4 Discussion

The AES, STM and LEED data presented above suggest a complex growth scenario for Fe adsorption on this substrate. Growth of the first layer takes place by the formation of small clusters which eventually coalese into an almost complete monolayer. The second and third layers form through the coalescence of larger islands rather than clusters, indicative of the difference in surface energy of the clean quasicrystal surface and the quasicrystal surface with monolayers of Fe adsorbed. The layers appear to be disordered, as no LEED pattern is observed. The growth mode up to this point is layer-by-layer, although the growth of each subsequent layer starts just before completion of the underlying layer. Above this coverage, there is a transition to a multilayer island growth mode. The islands themselves are consistent with the (110) bcc structure and are rotated by 72° from each other, suggesting a strong influence of the substrate in their alignment.

The formation of multilayer islands rather than a layer-by-layer growth mode has been observed in the homoepitaxy of Fe on Fe(100) [71, 72] and can be explained by a consideration of energy barriers in the system. Island formation occurs when the energy barrier to the diffusion of atoms downwards over step edges (the Ehrlich-Schwoebel barrier [74]) exceeds the surface diffusion barrier on a flat surface. Atoms landing on an incomplete layer recoil and are more likely to meet one another, increasing the probability for the nucleation of daughter islands onto incomplete layers, leading to the formation of the 'wedding cake' structure.

There are several points of agreement with the previous work on this system by Weisskopf and co-workers [44]. In particular, the initial loss of order followed by the appearance of the LEED pattern characteristic of (110) bcc Fe above 3 MLE is common to both studies. The deduction of the formation of multilayer islands at around this coverage is also a common feature. However on the point of whether intermixing takes place these studies are not in agreement. In their model, Fe first intermixes with the substrate. At higher coverages it was proposed that Al diffuses to the surface forming an Al-Fe alloy whose composition is uncertain. The evidence cited for these deductions are Auger data of the Fe signal showing a smaller increase during deposition than was observed for Fe on polycrystalline Cu, and the observation that the Pd and Mn AES signals do not decrease during initial Fe evaporation. In the current study the Al and Pd signals are clearly observed to decrease rapidly with increasing Fe adsorption, a behaviour inconsistent with intermixing at any coverage.

Some of the differences deduced in these studies could be attributable to differences in substrate and overlayer preparation. The *i*-Al-Pd-Mn surfaces used

by Weisskopf and co-workers in the Fe study [44] and in other studies [37, 38] are annealed to temperatures of 700-800 K after sputtering. In our STM experiments, annealing at temperatures below 870 K produces surfaces which are rather rough and clustered in morphology, but which are still atomically ordered and hence produce good LEED patterns [75]. It would be unsurprising if the behaviour of adsorbed species on such surfaces were different to that observed on surfaces annealed at higher temperatures and which are verified to be flat using STM. Furthermore, SEI probes a depth of some 2 nm, and as such is relatively insensitive to such differences in morphology. A further difference in preparation procedures is that in this study, Fe deposition was undertaken at room temperature ($\sim$ 300K), while in the study of Weisskopf and co-workers, the substrate was kept at $\sim$340 K. This small difference in temperature could be enough to induce interdiffusion of Fe and Al.

The lack of intermixing is also contrary to what is observed in studies of Fe adsorption on Al single crystal surfaces, where initial intermixing of Fe and Al is found. On Al(110) such intermixing was found up to 9 ML Fe deposition [76]. On Al(100) several studies have shown that initially alloying takes place yielding a disordered structure, and that at higher coverages of a few MLE, poorly ordered Fe(001) structures are formed [76, 77, 78]. Our result suggests that the quasicrystal surface, although Al rich, does not behave in the same way as single crystal Al surfaces. A quantitative technique with depth-dependent compositional capability such as medium energy ion scattering would be ideally suited to a study of this complex system [39].

5.5 Conclusions

STM, LEED and AES results indicate that at 300 K Fe initially adsorbs in disordered layers on the quasicrystal substrate. At coverages in excess of 3 MLE, it forms multilayer islands, oriented at angles of 72° to each other, which are consistent with a bcc (110) structure. No quasiperiodic order was observed.

Chapter 6

Fe deposition onto Al-Ni-Co under UHV conditions

6.1 Introduction

Iron was also deposited on to the surface of the decagonal $Al_{72}Ni_{11}Co_{17}$ quasicrystal. The structure of which is very different to the icosahedral quasicrystal as discussed in Section 2.2, thus offering an alternative quasicrystalline substrate for comparison of adsorption as demonstrated recently for the case of Si [26, 31]. The results are presented below.

6.2 Experimental details

We have applied the techniques of scanning tunneling microscopy (STM), low energy electron diffraction (LEED, Auger Electron Spectroscopy (AES) and X-ray magnetic circular dichroism (XMCD), to the study the adsorption of Fe on the 10-fold surface of the d-$Al_{72}Ni_{11}Co_{17}$ quasicrystal. The results are presented below and compared with the Fe/i-Al-Pd-Mn system. The sample preparation and experimental details for the standard surface science techniques are discussed in Section 3.1.

The XMCD measurements were undertaken in the ID8 beamline at the European Synchrotron Radiation Facility (ESRF) by J.A. Smerdon (University of Liverpool), S. Dhesi (Diamond), J. Ledieu (CNRS Nancy) and P. Bencok (ESRF). The beamline is equipped with a low temperature 7 T superconducting magnet, a spin-polarized photoemission spectrometer and a rapid field flipping chamber.

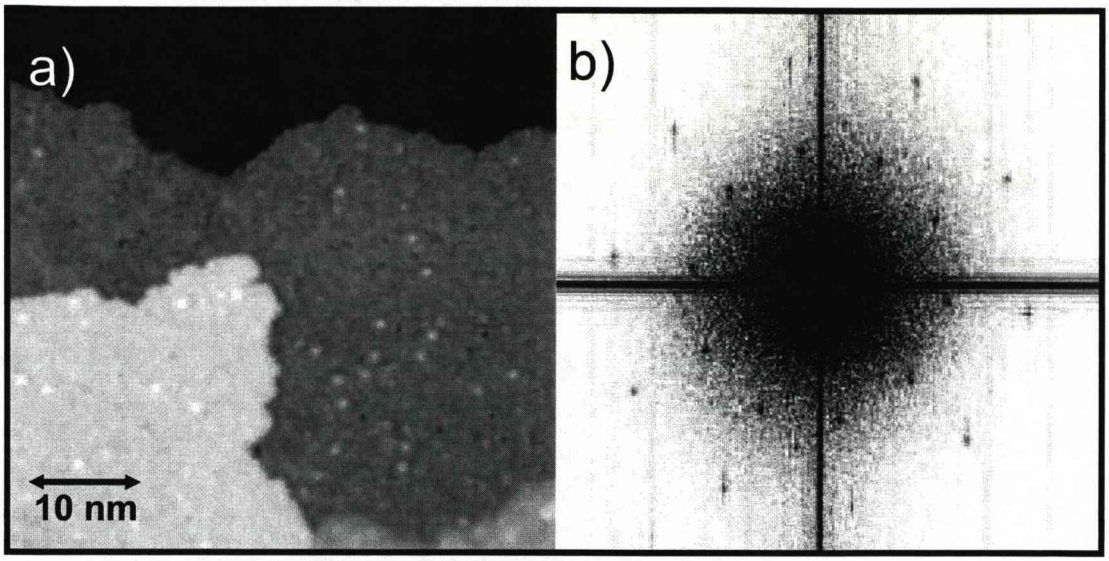

Figure 6.1: Left: 50 nm × 50 nm STM image of the clean surface of *d*-Al-Ni-Co. A quadratic compensation was applied to the image and the contrast was enhanced resulting in the apparent exclusion of the terrace at the top. Right: An FFT of the main image.

The photon energy is tunable in the range of 0.4 - 1.6 KeV, with an energy resolution close to $d\mathrm{E}/\mathrm{E} = 5\times10^{-4}$ at 850 eV. Iron was deposited at room temperature from a rod source using an Omicron EFM-3 electron beam evaporator, with coverage calibrated using a quartz crystal microbalance. These results are included as they allow an insight into the magnetic properties of the film/surface interface.

6.3 Results

6.3.1 STM and LEED

The starting surface in this experiment displayed large flat terraces, shown in Fig. 6.1(a). Fig. 6.1(b) shows a Fast Fourier Transform (FFT) taken from this image. The sharpness of the spots indicates a well-ordered substrate.

Figure 6.2(a)-(c) shows the growth process at submonolayer coverages of Fe. At the lowest coverage observed, Fe adsorbs onto the substrate in clusters of average apparent diameter 1.4 ± 0.5 nm. Further deposition increases the density of these clusters, until they join and form an interconnecting array at a coverage of 0.8 MLE. Figure 6.2(d)-(f) shows the continuation of the growth process up to a coverage of 6 MLE. At 1.2 MLE the first layer is fully complete. A faint LEED pattern identical to that of the clean surface is visible at a beam energy of 76

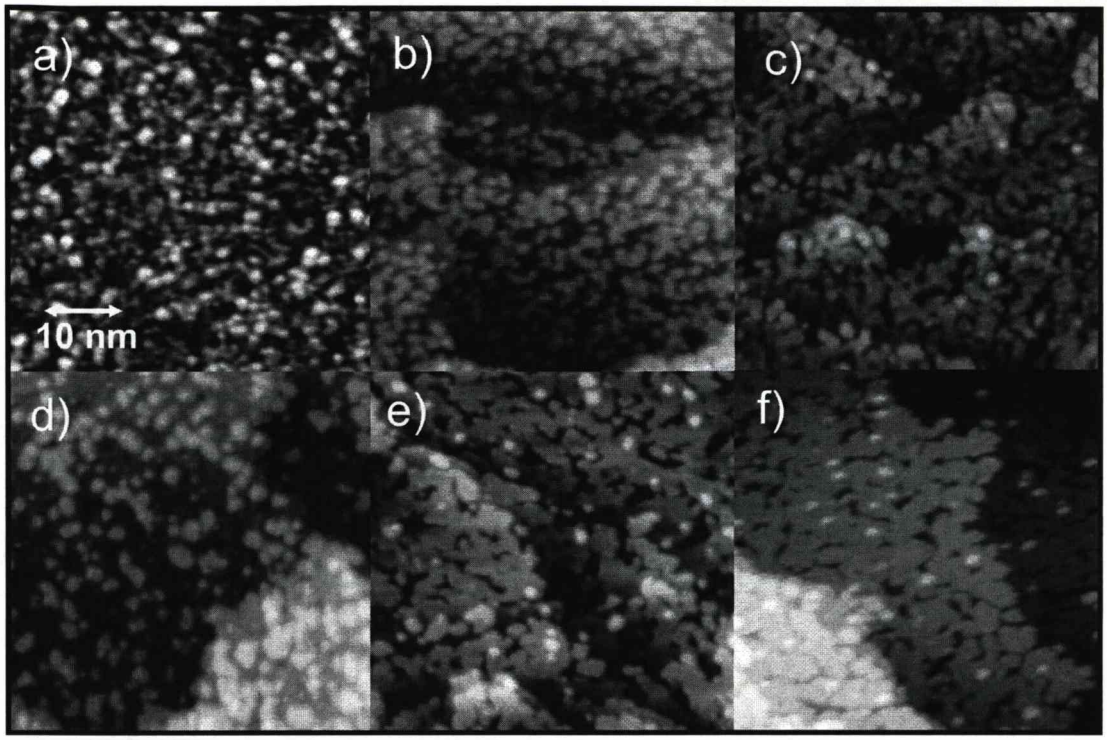

Figure 6.2: 50 nm x 50 nm STM images of the surface after the deposition of (a) 0.13 MLE, (b) 0.4 MLE, (c) 0.8 MLE, (d) 1.2 MLE, (e) 2.3 MLE and (f) 6 MLE of Fe.

eV. The growth mode during this phase is predominantly layer by layer, with the formation of the second layer occurring as clusters merge together. At 2.3 MLE (Fig. 6.2(e)) a nearly complete second layer is formed as the third layer begins to develop. This pattern of growth continues up to a coverage of 6 MLE (Fig. 6.2(f)), where no LEED pattern is observed.

As film growth continues up to 9.2 MLE, there is a transition from layer-by-layer growth to multilayer island growth. These islands have a more angular appearance (Fig.6.3(a-b)), with large flat bases approximately 8 nm in lateral extent. These form the foundation of subsequent increasingly smaller layers to produce an interconnected terraced structure, consisting of up to four tiers. A monatomic step height of 0.20 $\pm$ 0.01 nm was measured using a line profile analysis. The islands align along five-fold directions as shown by LEED (Fig. 6.3(c)); the LEED pattern can be interpreted as resulting from five cubic domains rotated by 72°. Atomic resolution of these islands was not achieved using STM.

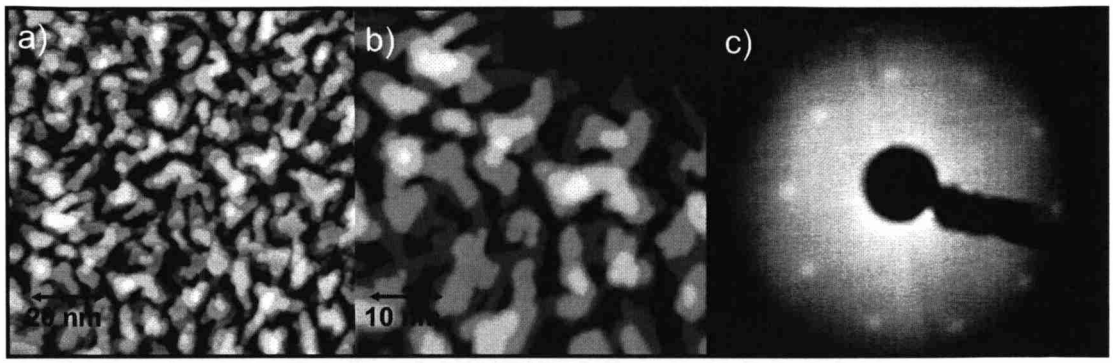

Figure 6.3: (a) 100 nm × 100 nm and (b) 50 nm × 50 nm STM images of the surface after the adsorption of 9 MLE of Fe on *d*-Al-Ni-Co; (c) LEED pattern taken with a beam energy of 120 eV.

6.3.2 AES

The growth process was also characterised using AES in a separate experiment. Figure 6.4 shows the magnitude of the peak to peak Auger signal for the Al LMM (68 eV), Co LMM (775 eV) and Fe LMM (651 eV) transitions as a function of Fe coverage. The Ni LMM (716 ev) peak is included in the figure for completeness. Trend lines are added as a visual aid as discussed below.

As discussed in Section 3.2.2 it has been shown that the AES data can be qualitatively compared with the expected shapes for various growth modes. Fig. 6.4 shows that after an initial decrease, the Al and Co Auger intensities do not decay further but remain at a constant value, and the Fe signal initially increases sharply but then also plateaus. This behaviour is indicative of intermixing leading to the formation of a surface alloy [55]. The results are comparable to those of previous studies when surface alloying has been inferred, e.g. for Pb deposited on Au [79].

The completion of the first monolayer is clearly observed as a break in the AES plot for all elements present. The linear rise/fall in the adsorbate/substrate signal indicates a constant sticking probability up to the development of a monolayer. During the formation of subsequent layers, adsorbed Fe intermixes with the substrate. After the monolayer break it is not possible to observe further line breaks corresponding to the completion of layers as there isn't a high enough density of data points. Such breaks are a result of the bulk signal attenuating at a constant rate with each forming layer until the bulk Auger signals become negligible and the concentration of surface substrate atoms and adsorbate atoms appears constant. This occurs at about 3 MLE. This is indicated by a plateau in the trend lines shown. Thereafter, no change is seen up to a coverage of 11 MLE, which was the highest coverage measured in this experiment. The data are

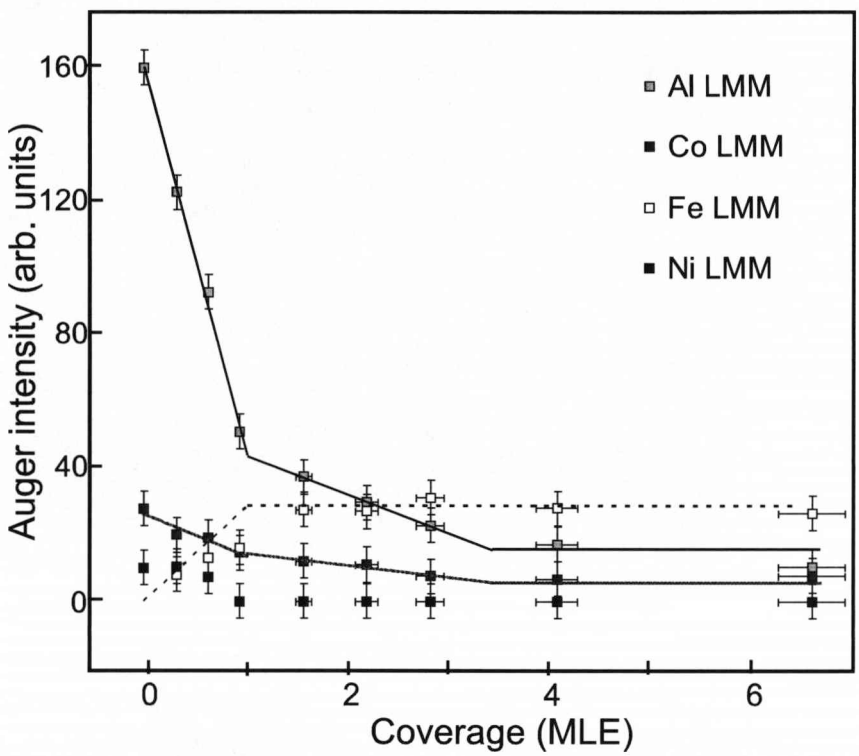

Figure 6.4: A plot of the Al LMM (68 eV) Fe LMM (651 eV), Ni LMM (705 eV) and Co LMM (775 eV) Auger peak intensity as a function of increasing coverage in MLE as defined in the text. Trend lines are added as a visual aid.

shown only up to 6 MLE in Fig. 6.4, to emphasise the changes taking place in the low coverage regime.

6.4 Magnetic Property

The technique of XMCD was employed as a probe of the magnetic properties of the deposited film [80]. This experiment was performed prior to the characterisation of Fe/Al-Ni-Co by standard surface science techniques. The results discussed, form part of J. Smerdons thesis [81] and are included for completeness. Circularly polarised radiation is characterised by a helicity vector which points either along the x-ray propagation direction **k** or along -**k**. Therefore at normal incidence ($\theta = 0°$) the radiation probes only out-of-plane magnetization; at $\theta = 60°$, which is the closest angle to grazing incidence possible with the experimental setup, predominantly in-plane magnetization is probed. The technique is element-specific, and an in-depth analysis can reveal details of the spin and orbital contributions to the magnetic moment. In this study however the technique is used only to extract qualitative comparisons of in-plane and out-of-plane magnetization.

For a thin film, the internuclear axes are preferentially oriented in the plane of the sample. The dominant magnetic exchange interaction causes dipole moments to align parallel. Therefore, the dipole-dipole energy is minimised when atomic moments align along the inter-nuclear axes leading to an in-plane direction for the magnetic moment [80]. In this experiment a larger dichroic response is found for the in-plane measurements of the Fe dichroic response (not shown). Hysteresis curves taken using the Fe XMCD signal for 3 MLE of Fe deposited on *d*-Al-Ni-Co at 5K verify that this is the case: a greater hysteresis is observed for the in-plane case (Fig. 6.5 (left)) than for out-of-plane (Fig. 6.5 (right)). This is consistent with the larger dichroic response observed, suggesting that the film locks into a state of magnetic order more readily for an inducing field parallel to the surface. Hardly any hysteresis is observed for the out-of-plane case implying the film exhibits highly anisotropic magnetisation characteristics.

There have been several studies of the magnetism of bulk *d*-Al-Ni-Co performed on single grain samples. Magnetization is described by the equation

$$M = \chi_0 H + M_0. \tag{6.1}$$

Markert and coworkers [15] found a weak ferromagnetic component of the magnetization $M_0(H)$ and a weak susceptibility $\chi_0 = \Delta M/\Delta H$. The magnetization

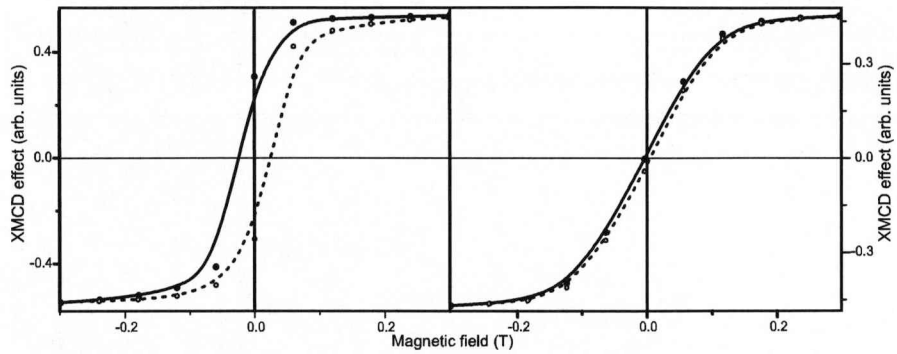

Figure 6.5: In-plane (left) and out-of-plane (right) hysteresis curves for 3 MLE of Fe deposited on *d*-Al-Ni-Co at 5 K. The points represent the peak of the Fe XMCD intensity normalised to the pre-edge intensity.

was found to be slightly anisotropic in- and out-of-plane (i.e. perpendicular and parallel to the ten-fold axis). Yamada *et al.* also reported a small ferromagnetic component and a weak diamagnetic susceptibility [14]. Jeglič and Dolinšik concluded from a nuclear magnetic resonance study that Co is in a nonmagnetic state in this material [11]. Our measurements of the Co XMCD signal from the clean surface of *d*-Al-Ni-Co are consistent with these previous studies. The dichroic response, shown in Fig. 6.6 (top) for the in-plane geometry, is vanishingly small. A similar result was obtained for the Ni signal (not shown).

When the same measurement is performed after the deposition of 3 MLE of Fe, a sizable response is found for Co (Fig. 6.6(bottom)). Similar results were found for the Ni signal. There are two possible contributions to this signal: (i) that, which has an in-plane magnetisation, induces a magnetization in the Co and Ni atoms at the interface; or (ii) that Fe induces a magnetization in Co and Ni atoms which have intermixed with the deposited material. The second explanation is certainly consistent with the Auger results described in Section 6.3.2 above. Contributions from both of these sources cannot be ruled out.

6.5 Discussion

The structure of the Fe film observed on the ten-fold surface may be compared to that observed on the 5-fold surface of *i*-Al-Pd-Mn [82]. A similar growth mode was observed in each case; the formation of a disordered layer-by-layer film, followed by a transition to island growth. Nanosized 'wedding cake' like islands are observed in both cases which have roughly the same dimensions, are aligned preferentially along five directions, have a monatomic step height and

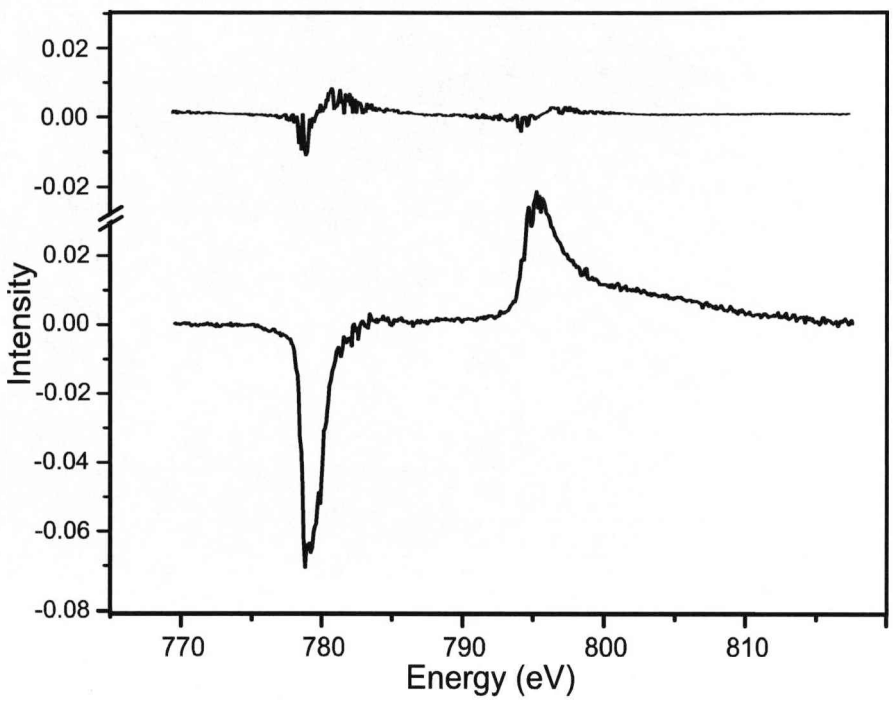

Figure 6.6: Top: The Co dichroic response of the clean Al-Ni-Co surface for the in-plane (θ=60°) geometry, at an applied field of 2 T at 300 K. Bottom: The Co dichroic response of the surface after deposition of 3 MLE of Fe; other parameters are as before.

produce identical LEED patterns. While the films are structurally similar, they are chemically very different. The formation of a pure Fe film is observed for Fe/Al-Pd-Mn, where substrate Auger signals decay exponentially indicating the formation of Fe islands. For Fe/Al-Ni-Co the formation of a surface alloy is observed, up to the maximum coverage studied (11 MLE).

The transition from layer-by-layer growth which occurs at about 9 MLE reflects a change in energetics in the system. This happens when the energy barrier to diffusion down step edges (the Ehrlich-Schwoebel barrier [74]) exceeds the surface diffusion barrier on the flat surface. Perhaps most surprising is that the resulting islands preferentially align along five directions. While it is was not possible to correlate these directions with high symmetry directions of the substrate due to the necessity to move the sample from the STM to the LEED system, it is reasonable to assume that this preferential alignment stems from the influence of the substrate persisting up to these coverages. A study using a depth-dependent structural and compositional technique such as medium energy ion scattering [40, 83, 84] could help clarify this point and also help determine the exact composition of the intermixed film.

These observation of the growth of a multilayer intermixed film indicates that in this system a quasiperiodic single-element system is not realised. Taken in conjunction with similar results for Fe on *i*-Al-Pd-Mn [44], Ni on *i*-Al-Pd-Mn [82, 37] and the observation of a quasiperiodically modulated periodic row structure for Co on *i*-Al-Pd-Mn and *d*-Al-Ni-Co [39], this is further evidence that the ferromagnetic transition elements do not produce quasiperiodic 2d or 3d overlayer systems.

6.6 Conclusions

STM, LEED and AES measurements of Fe deposited on *d*-Al-Ni-Co indicate that a disordered film forms up to a coverage of 9 MLE after which multilayered, interconnecting polycrystalline islands are observed. Intermixing of Fe with substrate elements is observed in the film, and after approximately 3 MLE, the relative concentration of elements remains constant. The XMCD results are in agreement with this picture; Fe has a predominantly in-plane magnetization, and Co and Ni both display magnetic moments consistent with their incorporation in the intermixed film, although a contribution from induced magnetism at the interface is not excluded.

Chapter 7

Electrochemical deposition of Cu onto AlPdMn

7.1 Introduction

Electrochemical deposition involves the adsorption of atoms, ions or molecules contained in a solution onto a surface through the application of a voltage across the solution/sample interface. Cyclic Voltammetry is employed to follow the change in current in an electrochemical cell with varying voltage. Changes in the shape of this plot reflect charge flowing across the interface arising for example from the oxidation or reduction process. Amperometry involves the instantaneous change of potential, whilst measuring the charge transfer, allowing for deposition rates to be calculated and under certain conditions the growth mode to be established. The simplicity of this deposition process coupled with the ability to mass produce are examples of why electrochemical deposition (or electroplating) is used to produce thin films on an industrial scale.

At present the main techniques used to explore the properties of thin film deposition onto quasicrystal surfaces are based in ultra high vacuum. This is a costly procedure and limits the ability to produce thin films on a large scale. If the properties of thin film grown onto quasicrystal surfaces were to be exploited by industry, the films must be able to be mass produced. Electrochemical deposition is a standard method of producing films on an industrial scale. This study provides the first steps in comparing films produced under UHV conditions with those formed under electrochemical conditions.

Previous to this study Cu was deposited onto the 5-fold surface of AlPdMn

in UHV conditions, where it was observed the that Cu formed a one dimensional pseudomorphic film, discussed earlier in Section 2.4.1. The motivation behind this exploratory investigation was to establish whether Cu could be electrochemically deposited onto a quasicrystal surface for comparison with a film produced under UHV conditions.

7.2 Background

7.2.1 Electrochemical deposition

Electrochemical deposition is the process of depositing a thin layer of metal onto a substrate through the application of a potential. This potential is applied across the substrate/solution interface to allow electrons to pass from the working electrode (substrate) to ions in the solution. Molecules in the solution accept electrons and become reduced to the working electrode surface. This process is known as reduction. The opposite case is known as oxidation, where an electron is removed from a molecule at the surface. The deposition of copper requires the acceptance of 2 electrons [85].

$$Cu^{2+} + 2e^{-} \leftrightarrow Cu \tag{7.1}$$

In a barrier representation of electron transfer at electrochemical interfaces application of a potential acts to alter the Fermi level; increasing the potential (through the application of a negative potential) increases the Fermi level. If the electrons in the metal have a higher energy than those in LUMO (lowest unoccupied molecular orbital) then electron transfer becomes thermodynamically favourable and reduction occurs [85]. If the electrode potential is made more positive electron transfer will be more favourable in the opposite direction, and electrons will transfer back across the interface allowing the Cu ions to redissolve into the solution. This process is illustrated in Fig. 7.1.

7.3 Experimental methods

7.3.1 The electrochemical cell

The sample was polished (as discussed in Section 3.1.6) then placed in the solution and extracted to produce a meniscus, containing solution to the polished face

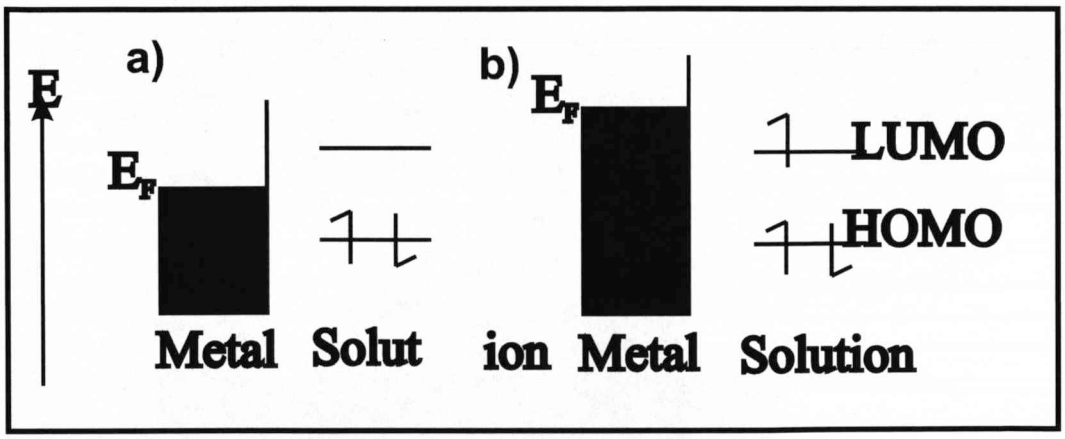

Figure 7.1: Electron transfer and energy levels a)electrode potential insufficient to drive the reduction of O and b) at a reduced potential the electrode process becomes more thermodynamicall favourable [85].

of the crystal only. The solution consists of 0.001M Cu^{2+} salt and 0.1M of electrochemically inert electrolyte. This inert electrolyte maintains electroneutrality ensuring the electric field does not build up as electrolysis proceeds, allowing the complex mass transport effects which arise from migration to be neglected. Calculations show that approximately 100 times the concentration of background electrolyte relative to reactant is required if the measured current is not perturbed significantly (less than one percent) from its value where no migration takes place [85]. Argon is used to degas the cell and provide an inert atmosphere.

Figure 7.2 shows a schematic of the electrochemical glass cell used consisting of three electrodes. The first is the working electrode (WE), which in this case is the Al-Pd-Mn crystal. Current flowing across this interface is to be measured. The second is the reference electrode. This reference electrode (RE) maintains a fixed potential across its interface with the solution, allowing the measurement of the potential across the WE/solution interface. However the passage of large currents through the reference electrode may change its chemical composition, therefore altering the potential at the solution/RE interface. To overcome this problem a third electrode known as the counter electrode (CE) is introduced, and controlled by electronics to ensure current only flows between the RE and WE and the potential of the CE is held relative to a stable RE. The Luggin probe acts to separate the CE from the WE and RE and prevents any products from electrolysis that occurs on the CE surface from entering the RE chamber [85].

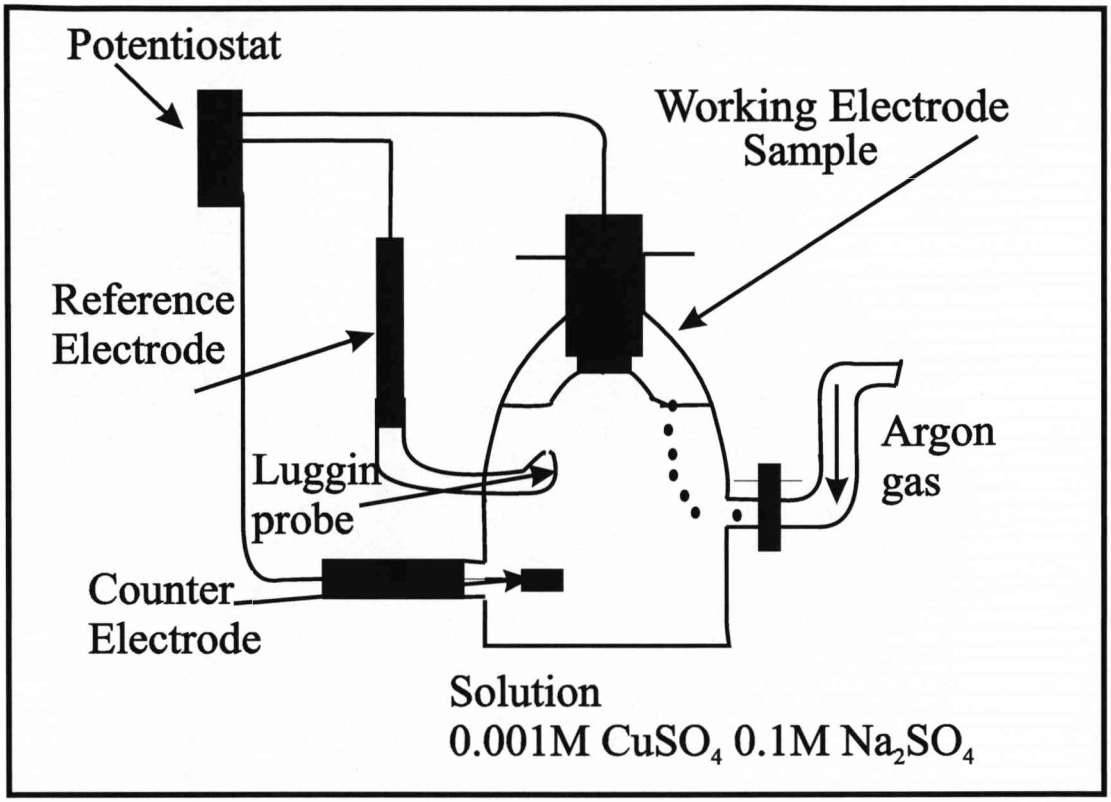

Figure 7.2: A schematic of the electrochemical cell.

7.3.2 Cyclic Voltammetry

The potential at the WE is controlled and current flow through the electrode is measured. Cycling between two potentials cycles the redox reaction. The transfer of electrons can be in either direction. Sweeping from positive to negative, a molecule in the solution accepts electrons from the electrode and becomes reduced. Then sweeping back, electrons can be removed from the molecule and the atoms and become oxidised.

This technique is quick and easy to perform and gives a great deal of information about the system. Information such as the oxidation and reduction potentials, the type of reaction (reversible/irreversible), and whether any coupled chemical reactions occur on the surface, can be obtained. A coupled chemical reaction is a chemical reaction that takes place on the surface once electrolysis has occurred. The products formed at the surface may also be active, the reduction of which will occur at a different potential, resulting in multiple oxidation/reduction peaks in the CV.

7.3.3 The Nernst Equation

The Nernst equation can be used to estimate the potential at which the reduction of species occurs at the working electrode surface. When the applied potential is equal to the equilibrium potential of the cell, no current will flow across the sample/solution interface. For the case of a reversible reaction, reduction becomes thermodynamically viable when small overpotentials are applied. Reduction occurs near the equilibrium potential of the cell, which can be calculated by the Nerst equation as follows

$$E = E^{\circ} - (RT \div (nF)) \log(Q) \tag{7.2}$$

For simple processes e.g. [o]+e^-=[R] the charge (Q) can be simplified to

$$Q = ([O] \div [R]) \tag{7.3}$$

where the equilibrium potential (E) of the electrode results from the standard electrode potential (E°) of the reaction and concentrations of O and R at the electrode surface, which under equilibrium conditions are the same as their bulk values. [O] is the concentration of Cu ions and [R] the concentration of Cu atoms at the interface. The standard electrode potential for Cu is 0.34V for a standard hydrogen electrode. To convert this to the potential for Cu deposition through a Calomel electrode a factor of 0.244V is added, therefore 0.096V is required for 1M of solution. As only 1mM is used for these experiments ($Q = 1/1 \times 10^{-3}$) the equilibrium potential of the cell is 0.008 V.

7.3.4 Amperometry

This technique involves the instantaneous stepping between a potential at which reduction doesn't occur (for the purpose of this experiment the potential is held at the oxidation potential to ensure all Cu is removed from the surface) and a second potential where the conversion of Cu ions in the solution to Cu at the electrode interface takes place. This technique provides an quantitative measure of the amount of charge transfer. This can be used to determine under favourable circumstances the number of layers of Cu deposited.

Immediately following the step a large current is detected which then falls steadily with time. This large step arises since the magnitude of the current is controlled by the rate of diffusion of the Cu ions to the surface. The concentration gradients shortly after the step are large, hence the large current. This then falls as the depletion of the electroactive material occurs. The 'diffusion layer' increases

as fresh electrolyte has further and further to travel through the diffusion layer until the electrode interface is reached.

7.3.5 Sample preparation

The working electrode consisted of a thin copper wire glued onto the back of the Al-Pd-Mn sample with conductive silver glue, encapsulated with a two part superepoxy glue to protect the contact glue from wear. The sample was polished by hand, as discussed in Section 3.1.6.

A saturated calomel electrode was used to maintain a constant potential of +0.246 V between the reference electrode and the working electrode. The counter electrode comprises of a $1cm^2$ platinum mesh. The electrochemical cell and reference electrode were cleaned using an acid solution of 50 percent sulphuric acid 50 percent hydrochloric acid, then rinsed thoroughly with ultra pure water.

A solution of 0.001M $CuSO_4$ $5H_2O$, 0.1M Na_2SO_4 was prepared. The base electrolyte 0.1M Na_2SO_4 remains electrochemically inactive in the potential range used for this experiment. The base electrolyte is responsible for migration in the cell and results in diffusion only conditions. The solution was degassed using Argon for 30 minutes prior to the experiment. The crystal was then submerged into the solution under a constant potential of 0 V, to minimise any changes to the surface structure. This was carried out in an Argon atmosphere to remove O_2 and CO_2 from the cell. The crystal was then slightly retracted to produce a meniscus to maintain the solution on the polished face of the crystal only.

7.4 Results and discussion

7.4.1 Cyclic Voltammetry performed in the absence of Cu

To ensure no reactions result from the base electrolyte the experiment was first performed in the absence of Cu. The cyclic voltammogram, shown below confirms the solution is chemically inert between the potentials of -700 mV and 200 mV, confirming the absence of any chemical reactions between the buffer solution and surface, as shown in Figure 7.3. There are however peaks at about -200 mV (anodic) and -400mV (cathodic) marked Al and B1 on the Voltammogram. The origin of these peaks are not known, but consideration has to be given to them since they occur in a potential region of relevance for Cu deposition and dissolution.

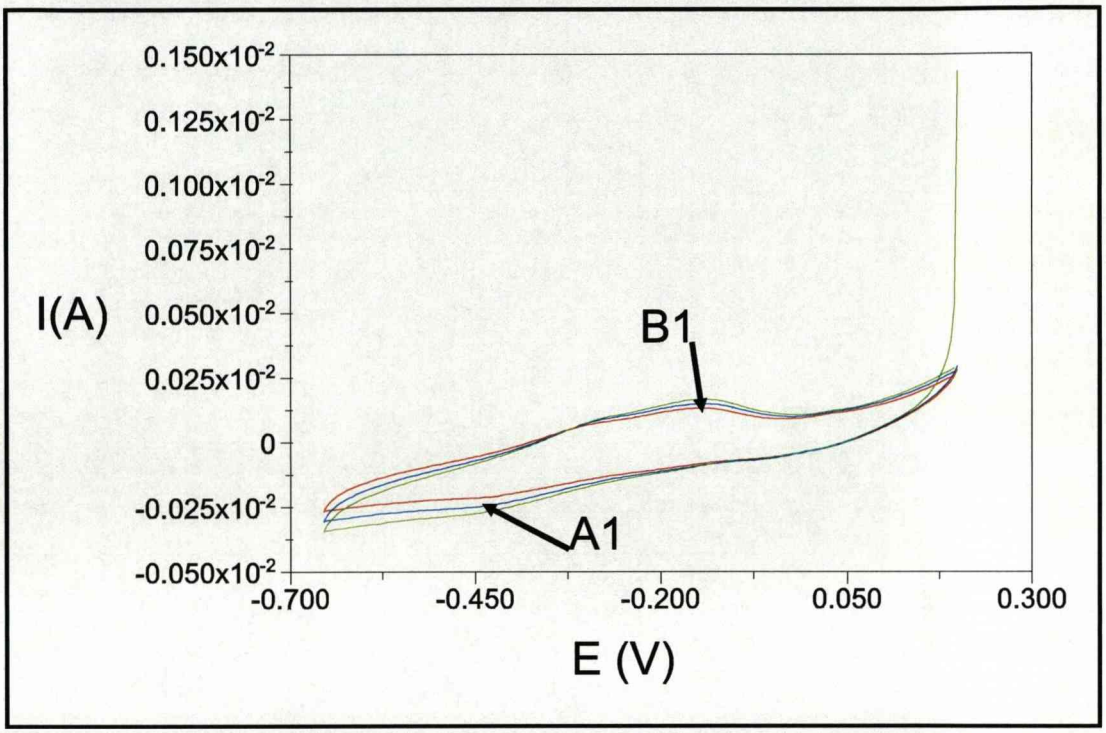

Figure 7.3: Cyclic voltammogram taken between 150 mV and -650 mV in a buffer solution of solution of 0.1M Na_2SO_4. Scan rate = $0.005 vs^{-1}$, Step potential = 0.005v

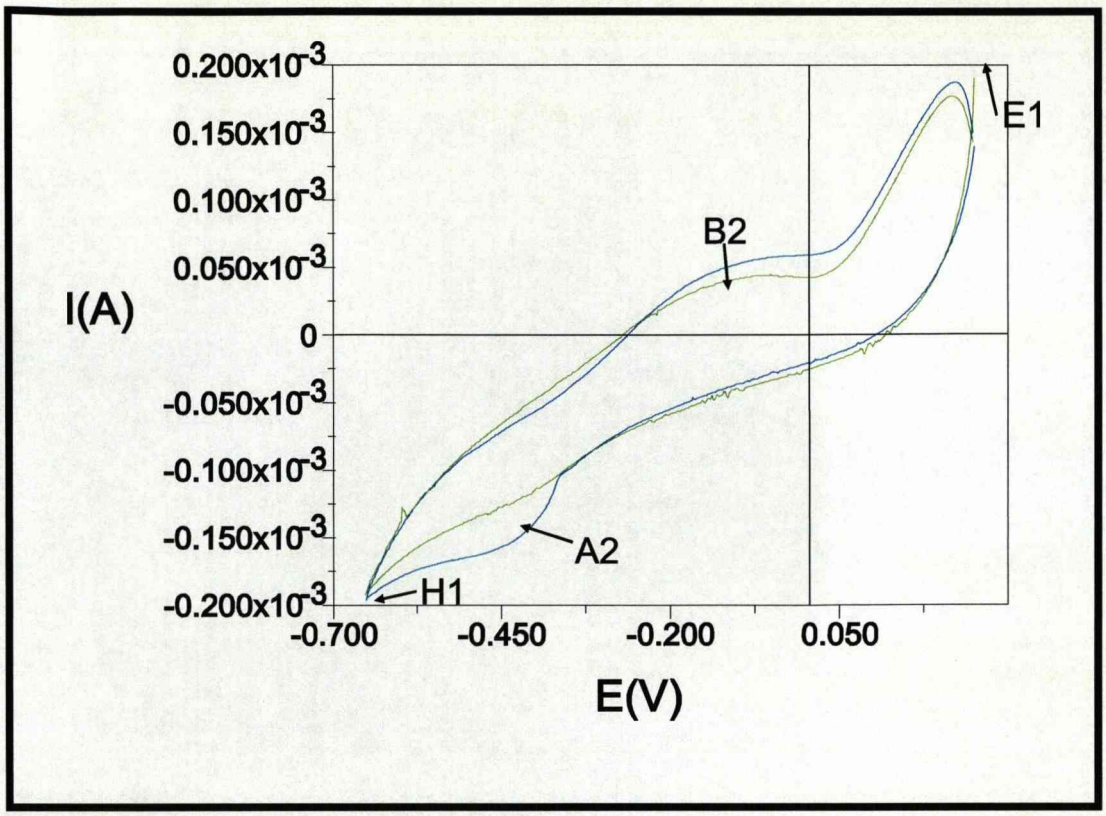

Figure 7.4: Cyclic voltammagram scanning between 150 mV to -650 mV in a Cu solution of solution of 0.001M $CuSO_4$ $5H_2O$, 0.1M Na_2SO_4. Scan rate = $0.02Vs^{(}-1)$, Step potential = 0.002 v.

7.4.2 Cyclic Voltammetry performed in the presence of Cu

Cyclic voltammetry (CV) was then performed in the chemically active Cu solution to determine the oxidation and reduction potentials of Cu onto AlPdMn, see Fig. 7.4. Hydrogen evolution occurs at potentials less than -700 mV (peak H1 in Fig. 7.4) and etching occurs at potentials greater than 300 mV(peak E1).

Peaks A2 and B2 may in part arise from copper-deposition and dissolution. However they lie close in potential and are of similar current magnitude to peak A1 and B1 for the buffer solution so on the basis of the voltammogram no conclusive assignment can be made. A more pronounced reduction peak is observed during the second scan, however it must be noted that the total cathodic current is the area under the scan in one direction (below I=0) plus the area under the scan in the returning direction. The different shape of the scans may be a result of a change in the surface structure or composition - remaining Cu atoms may increase the rate of Cu deposition. This change can also be observed in the proceeding four scans Figure 7.5, during which a slight shift in the oxidation

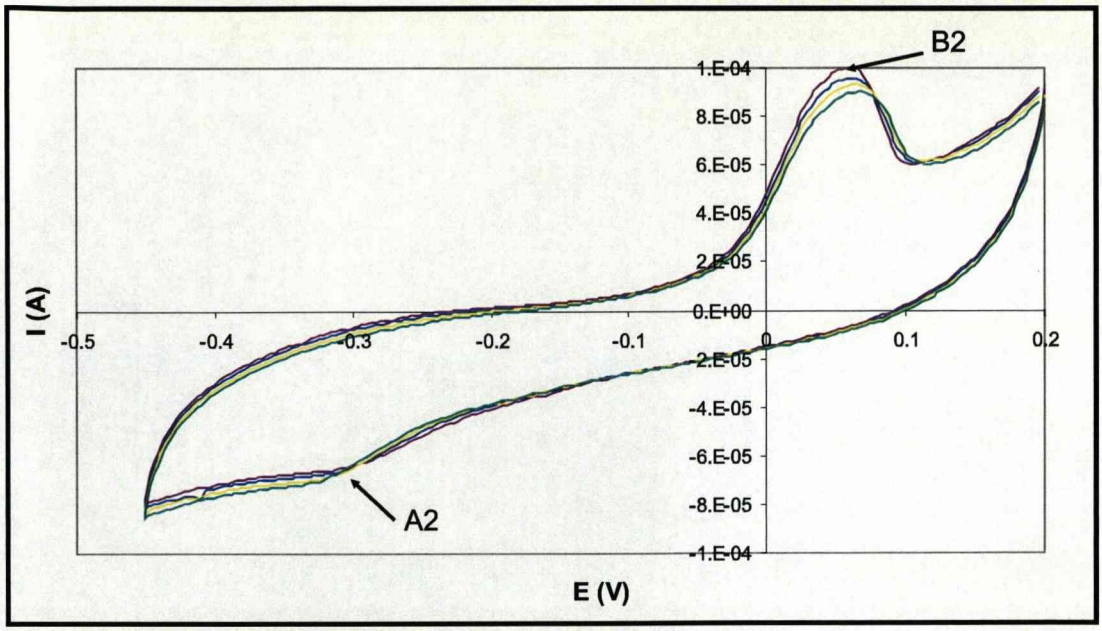

Figure 7.5: Cyclic voltammagram showing four scans taken between 200 mV and -650 mV. Scan rate = 0.02 Vs^{-1}, Step potential = 0.002v. Taken in a solution of 0.001M $CuSO_4$ $5H_2O$, 0.1M Na_2SO_4.

and reduction peak is observed. It is also noted that peak B2 becomes more pronounced and this peak may arise from dissolution of the copper film ($Cu \longrightarrow Cu^{2+}$). However some doubts still remain to its assignment due to its proximity to peak B1 in the buffer solution Fig. 7.3.

It can be seen in Figure 7.6(a) that the scan rate has a large influence in the resolution of the reduction peak. It was found that a reduction in the scan speed increases the prominence of this peak. The practicality of reducing the scan speed to just 0.001 Vs^{-1} however is that scanning takes a few hours. In practice a scan speed of 0.02 Vs^{-1} was adequate to produce satisfactory voltammograms. The step potential; the difference in voltage between consecutive scan points, did not bear any effect on the shape of the voltammogram 7.6(b).

7.4.3 Current Transient

Current transients were performed with the presumption that peak A2 arises from Cu deposition and peak B2 arises from dissolution. Using the assumption and the results obtained through cyclic voltammetry it was possible to determine the most suitable potentials for the amperometry experiments, which allow for deposition and no hydrogen evolution, i.e. -650 mV to -300 mV, and oxidation without any oxygen evolution, 50 mV to 300 mV. The crystal was submerged into the solution under a constant potential of 0V. The potential was then set

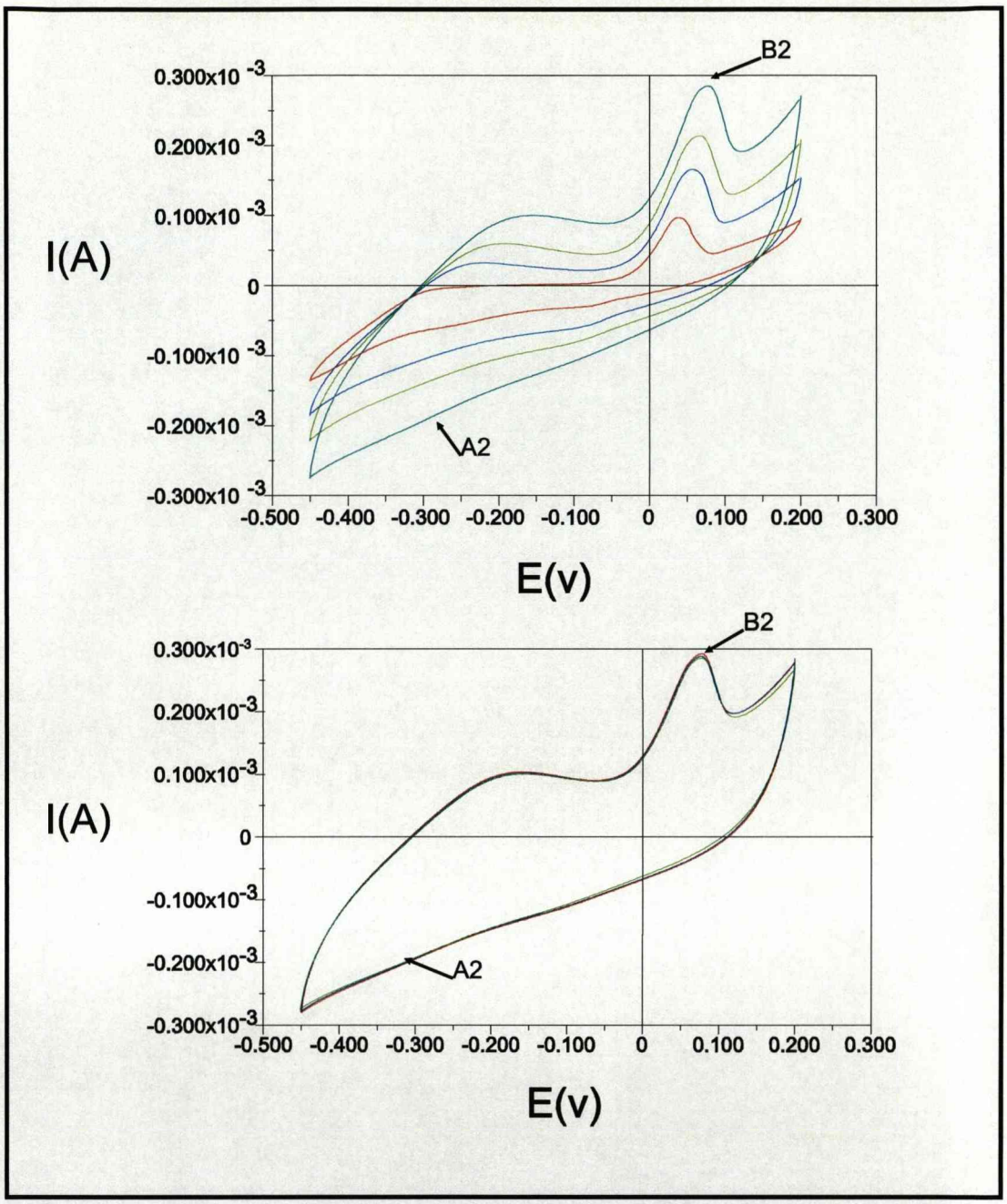

Figure 7.6: Cyclic voltammetry taken of Cu/AlPdMn with varying scan rates and step potentials. a) Scan rate (from the outside inwards) = 0.02 Vs^{-1} (aqua), 0.01 Vs^{-1} (green), 0.005 Vs^{-1} (blue), 0.001 Vs^{-1} (red). Step potential = 0.002 V (with the exception of 0.02 Vs^{-1}, Step potential = 0.0005 V). b) Scan rate = 0.02 Vs^{-1}, Step potential = 0.002 V, 0.001 V, 0.0005 V. Taken in a solution of 0.001M $CuSO_4$ $5H_2O$, 0.1M Na_2SO_4.

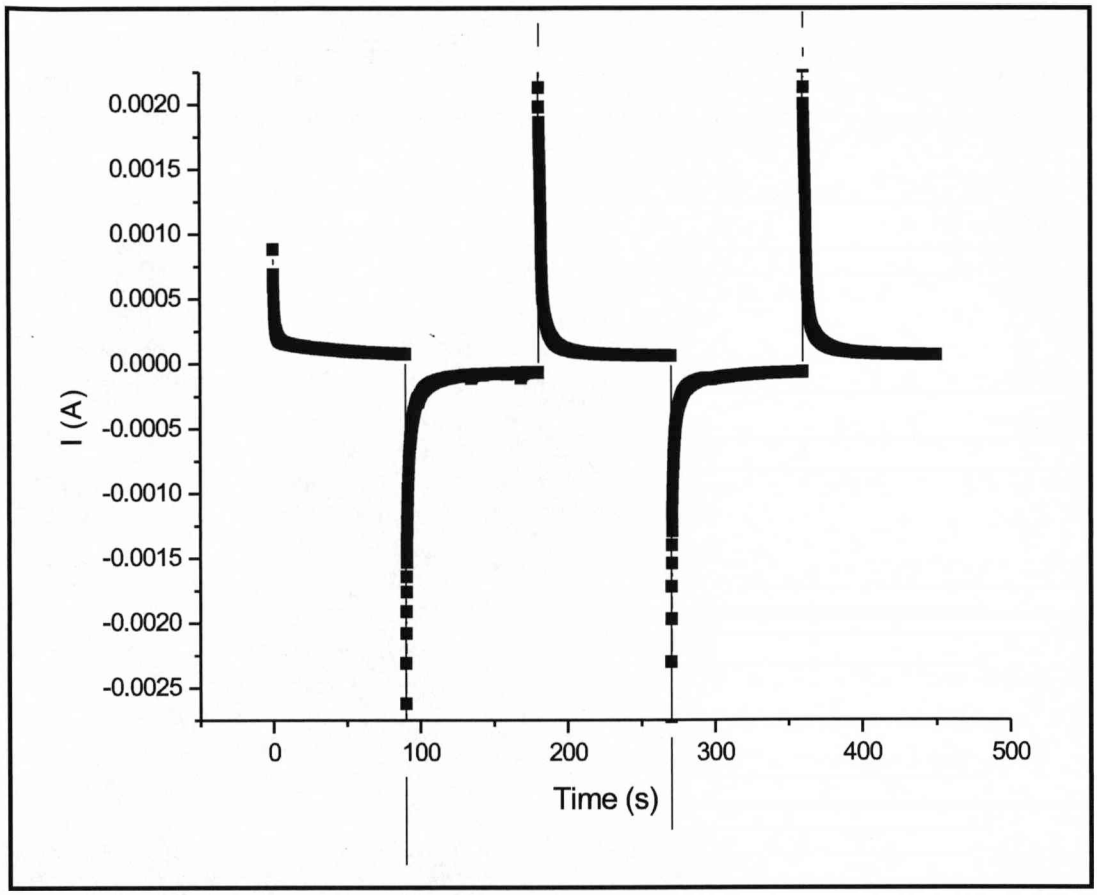

Figure 7.7: Current Transient for Cu/AlPdMn. Periodically alternating between the oxidation and reduction potentials of 200 mV and -550 mV. Solution containing 0.001M $CuSO_4$ $5H_2O$, 0.1M Na_2SO_4.

to 0.2 V for a period of 90 seconds, before being instantaneously switched to the reduction potential of -0.55 V for 90 seconds, as shown in Fig. 7.7.

The current was recorded over a period of 90 seconds at intervals of 0.1 s. Integration of this curve gives the charge transfer, which can be used to determine the number of Cu atoms adsorbed onto the surface. This assumes that all the current flowing arises from the copper deposition. A charge transfer of 7.70×10^{-5} C is needed to deposit roughly one monolayer of Cu (molar volume of Cu is 7.11 cm^3, two electrons are transferred per atoms). This can be used to determine the number of atoms/layers adsorbed.

As shown in Fig. 7.8 approximately 24 layers of copper were deposited at a potential of -550 mV. The copper was then removed from the surface by applying a potential of 200mV for a period of 90 seconds, the total number of layers removed was approximately 21. For consistency the Cu was deposited again at a potential of 550mV for 90 seconds, as can be seen less copper is deposited during the second cycle. After 90 seconds a total of 22 layers were deposited.

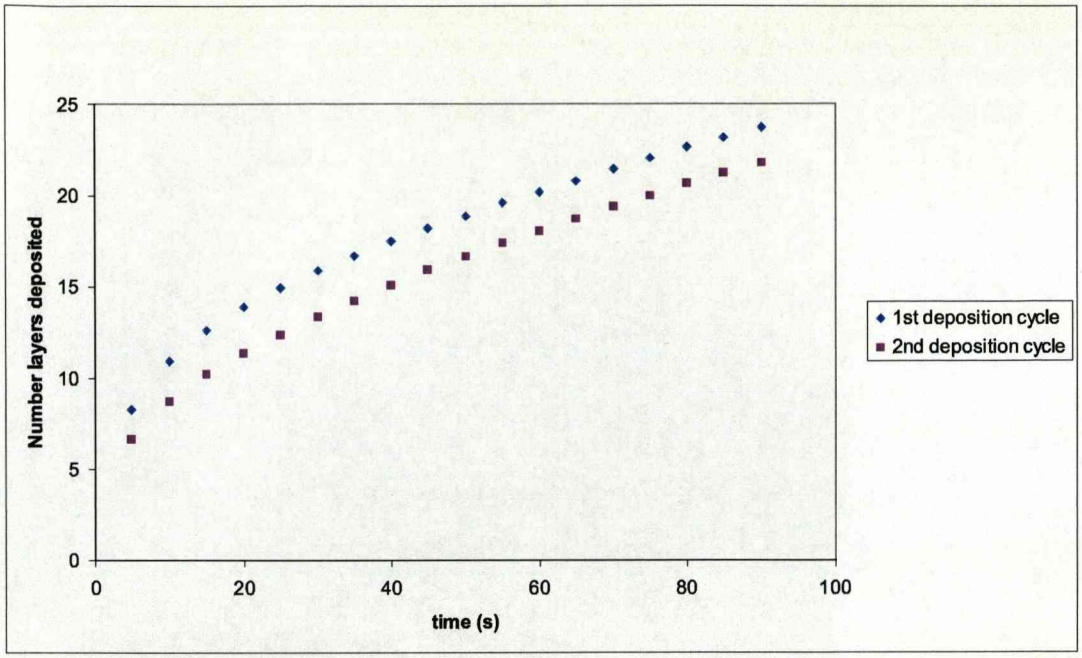

Figure 7.8: A plot to show the number of Cu layers deposited on the surface of Al-Pd-Mn against time, at a potential of -550 mV. Solution containing 0.001M $CuSO_4$ $5H_2O$, 0.1M Na_2SO_4

The rate of deposition is rapid to begin with, with 10 layers being deposited in the first 10 seconds, after which the rate of deposition begins to decrease. This is due to the depletion of electrolyte at the substrate/solution interface. As this depletion layer extends into the solution, the fresh $Cu^{2+}(aq)$ required has further to travel to the electrode surface. The rate of deposition thus depends on the transport of fresh electrolyte through the solution, which will steadily decrease as the depletion layer extends. As expected the results show Cu does remain on the surface after each cycle. Therefore the crystal must be repolished between scans in order to obtain a good calibration as to the number of layers deposited at varying reduction potentials. This was not the case for this experiment. Even so a general pattern emerges; the number of layers deposited is roughly proportional to the potential (Fig. 7.9).

These plots characterise the deposition and are useful for future in-situ STM studies. Difficultly may arise when depositing less than 2 layers, as the time scale required is very small. This may be resolved through further studies by increasing the potential to greater than -300 mV.

Amperometry was then performed to try to produce a curve showing the rising transient. The rising transient can be fitted and used to determine if the growth mode is instantaneous or progressive. The rising transient in this case was not and therefore the growth mode could not be determined.

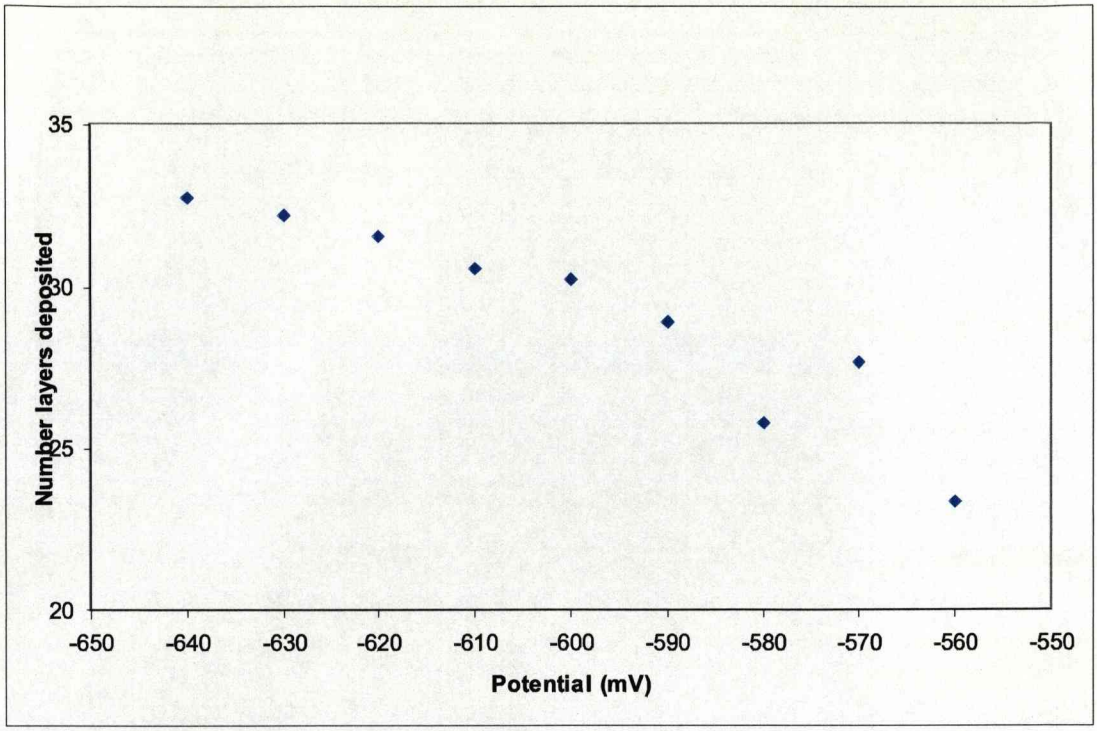

Figure 7.9: A graph showing the number of layers of Cu deposited on Al-Pd-Mn after 90s at various potentials in a solution of 0.001M $CuSO_4$ $5H_2O$, 0.1M Na_2SO_4. Under the assumption that there is 100% current efficiency for Cu deposition.

7.5 Conclusions

These exploratory results indicate that Cu may be electrochemically deposited onto the surface of Al-Pd-Mn under electrochemical conditions, using a solution of 0.001M $CuSO_4$ $5H_2O$, 0.1M Na_2SO_4. The cyclic voltammogram shows a stable region between -650 mV and 300 mV which is void of oxygen and hydrogen evolution. Reduction of $Cu^{2+} \longrightarrow Cu$ occurs at potentials below -300 mV and oxidation of $Cu \longrightarrow Cu^{2+}$ at potentials exceeding 50 mV. The results indicate a change in the surface composition with increasing cycles.

No UPD of Cu was observed. This indicates that the interaction between the metal/bulk metal is stronger than the interaction between the electrode/deposited metal for this system. The stronger the interaction between the electrode and the deposited metal the increased likelihood of producing a pseudomorphic film. Therefore the production of a two dimensional aperiodic Cu film under these conditions is extremely unlikely. Further structural characterisation is require to find out if the structure adopts the same one dimensional pseudomorphic array as observed under UHV conditions.

7.6 Future Work

It has been established that the sample must be repolished after every scan. Therefore it makes sense to repeat the amperometry measurements, repolishing for each potential to obtain a more accurate data set to allow for number of monolayers deposited with respect to time and potential to be calibrated.

The next stage would be to perform in-situ STM measurements to characterise the surface of the alloy in the presence of the electrolyte under a potential of 0V, and the Cu film at various thicknesses. This would allow for a comparative study between electrochemical deposition and deposition in UHV. The one major drawback to this procedure is the preparation of the crystal. In order to achieve atomic resolution the crystal has to be prepared using a sputtering and annealing procedure in UHV conditions. To complete a comprehensive comparison one needs to prepare the crystal in UHV to obtain the flat terrace phase, then transfer the sample into an electrochemical cell, where the film maybe deposited. This can be done a number of ways. The first would be to build an electrochemical cell onto the chamber and allow for the sample to be transferred directly into the cell under UHV conditions. The second would be to cap the crystal, with an element that can easily be electrochemically removed and would not interact with the deposition of Cu in the cell.

Chapter 8

Conclusions

The work undertaken in this thesis primarily had the goal of investigating the fundamentals of aperiodicity. This was achieved by producing a quasicrystalline film composed of one element, through the deposition of Pb on the 5-fold surface of Al-Pd-Mn. The results show the formation of the psuedogap at the Fermi level in quasicrystals is in fact due to the aperiodicity of the system and not its chemical complexity.

The next goal was to try and investigate the effect aperiodicity on a truly magnetic system. It was hoped by depositing Fe on the 5-fold surface of Al-Pd-Mn and 10-fold surface of Al-Ni-Co an aperiodic film could be formed. For both systems the formation of a single-element quasicrystal was not realsied. Instead the formation of a periodic structure aligned along the high symmetry axes was observed. Taken in conjunction with similar results for Ni on *i*-Al-Pd-Mn [37] and the observation of a quasiperiodically modulated periodic row structure for Co on *i*-Al-Pd-Mn and *d*-Al-Ni-Co, it appears that the ferromagnetic transition elements do not produce quasiperiodic 2d or 3d overlayer systems.

A preliminary investigation into the electrochemical deposition of thin films onto quasicrystal surfaces was also investigated. Currently the characterisation of surfaces and thin films is best done under UHV conditions, as this provides a clean environment for the systems to be studied. This however is a costly process, and if such a system was to one day be exploited by industry a cheaper alternative would be beneficial. As a result a preliminary investigation of the electrochemical deposition of Cu onto Al-Pd-Mn was carried out. The results indicate that Cu may be deposited onto the surface of Al-Pd-Mn under such conditions. Further work is needed to enable a comparative study of Cu deposition onto the surface of Al-Pd-Mn under UHV and electrochemical conditions.

Chapter 9

Appendix

9.1 List of Publications

Iron deposition on the ten-fold surface of the decagonal Al-Ni-Co quasicrystal
L.H. Wearing, J.A. Smerdon, L. Leung, S. Dhesi, J. Ledieu, P. Bencok, I. Fisher, C.J. Jenks, R. McGrath, accepted for publication, J.Phys. Condensed Matter.

Iron deposition on the five-fold surface of the icosahedral Al-Pd-Mn quasicrystal
L. Wearing, J.A. Smerdon, L. Leung, T.A. Lograsso, A.R. Ross, R. McGrath, Surf. Sci, **601**, 16, 3450, (2007).

Self assembly, structure, and electronic properties of a quasiperiodic lead monolayer
J. Ledieu, L. Leung, L.H. Wearing, R. McGrath, T.A. Lograsso, D. Wu, V. Fournée, Phys. Rev. B, **77**, 073409, (2008).

Adsorption of cobalt on the ten-fold surface of d-$Al_{72}Ni_{11}Co_{17}$ and on the five-fold surface of i-$Al_{70}Pd_{21}Mn_9$
J.A. Smerdon, J. Ledieu, J.T. Hoeft, D.E. Reid, L.H. Wearing, R.D. Diehl, T.A. Lograsso, A.R. Ross, R. McGrath.
Phil. Mag 68 (6-8); 841-847.(2006)

9.2 Presentations

Oral Presentations

The search for a magnetic aperiodic overlayer
Interdisciplinary Surface Science Conference (ISSC16), St Andrews 2007.

Iron deposition onto quasicrystal surfaces
Condensed matter physics group, University of Liverpool, Dec 2006.

Electrochemical deposition of Copper onto quasicrystal surfaces
Complex Metallic Alloys Network of Excellence, VIL-D topical meeting, Berlin 2006.

Poster Presentations

Deposition of magnetic thin films on to Quasicrystal surfaces
European Conference of Surface Science (ECOSS), Paris 2006.

Deposition onto quasicrystal surfaces
Surface Science Summer School, University of Nottingham 2005.

'Forbidden Beauty'
Royal Society summer exhibition, London 2004. Milton Keynes Science Festival, 2005.

Bibliography

[1] D. Shechtman, I. Blech, D. Gratias, and J. W. Cahn, Phys. Rev. Lett. **53**, 1951 (1984).

[2] L. Pauling, Nature **317**, 512 (1985).

[3] B. Dubost, J.M. Lang, M. Tanaka, P. Sainfort, and M. Audier, Nature **324**, 48 (1986).

[4] P. A. Thiel, Prog. Surf. Sci. **75**, 69 (2004).

[5] C. J. Jenks, J. W. Burnett, D. W. Delaney, T. A. Lograsso, and P. A. Thiel, Applied Surface Science **157**, 23 (2000).

[6] N. Ferralis, K. Pussi, E.J. Cox, M. Gierer, J. Ledieu, I.R. Fisher, C.J. Jenks, M. Lindroos, R. McGrath, and R.D. Diehl, Phys. Rev. B **69**, 153404 (2004).

[7] R. McGrath, J. Ledieu, and R. D. Diehl, Prog. Surf. Sci. **75**, 131 (2004).

[8] Z. Papadopolos, G. Kasner, R. D. Diehl, J. Ledieu, E. J. Cox, N. V. Richardson, Q. Chen, T. A. Lograsso, A. R. Ross, and R. McGrath, Phys. Rev. B **66**, 184207 (2002).

[9] R. McGrath, J. Ledieu, E. J. Cox, and R. D. Diehl, J. Phys.:Condensed Matter **14**, R119 (2002).

[10] C. Kittel, *Introduction to Solid State Physics*, 7 ed. (John Wiley and Sons, Inc, New York, 1996).

[11] P. Jeglič and J. Dolinšek, Phys. Rev. B **71**, (2005).

[12] T. J. Sato, H. Takakura, A. P. Tsai, and K. Shibata, Phys. Rev. B **81**, 2364 (1998).

[13] C. Benoit, B. Ouladdiaf, and D. Schmitt, Phys. Rev. Lett. **78**, 4637 (1997).

[14] Y. Yamada, Y. Yokoyama, K. Matono, K. Fukaura, and H. Sunada, J. Appl. Phys. **38**, 52 (1999).

[15] J. T. Markert and J. L. Cobb, J. Appl. Phys. **76**, 6110 (1994).

[16] V. Fournée and P. A. Thiel, J. Phys. D: Appl. Phys. **38**, R83 (2004).

[17] H. R. Sharma, M. Shimoda, and A. P. Tsai, Adv. Phys **56**, 403 (2007).

[18] J. E. Inglesfield, Prog. Surf. Sci. **20**, 105 (1985).

[19] O. Zaharko, C. Meneghini, A. Cervellino, and E. Fischer, Eur. Phys. J. B **19**, 207 (2001).

[20] D. Gratias, F. Puyraimond, M. Quiquandon, and A. Katz, Phys. Rev. B **63**, 024202 (2000).

[21] J.M. Dubois, P. Plaindoux, E. Belin-Ferré, N. Tamura, and D.J. Sordelet, Proceedings of the 6th. International Conference on Quasicrystals 451 (1998).

[22] V. Elser, Phil. Mag. B **73**, 641 (1996).

[23] P. Kramer, Z. Papadopolos, M. Schlottmann, and D. Zeidler, J. Phys. A. Math. Gen **27**, 4505 (1994).

[24] M. Krajci and J. Hafner, Phil. Mag. **86**, 825 (2006).

[25] M. Gierer, M. A. Van Hove, A. I. Goldman, Z. Shen, S. L. Chang, C. J. Jenks, C. M. Zhang, and P. A. Thiel, Phys. Rev. Lett. **78**, 467 (1997).

[26] J. Ledieu, P. Unsworth, T. A. Lograsso, A. R. Ross, and R. McGrath, Phys. Rev. B **73**, (2006).

[27] M. Ohring, *The Material Science of Thin Films* (Academic Press, San Diego, 2002).

[28] J. Ledieu, C. A. Muryn, G. Thornton, R. D. Diehl, T. A. Lograsso, D. W. Delaney, and R. McGrath, Surf. Sci. **472**, 89 (2001).

[29] J. Ledieu, J. T. Hoeft, D. Reid, J.A. Smerdon, R. D. Diehl, T. A. Lograsso, A. R. Ross, and R. McGrath, Phys. Rev. Lett. **92**, 135507 (2004).

[30] J. Ledieu, J. T. Hoeft, D. E. Reid, J. A. Smerdon, R. D. Diehl, N. Ferralis, T. A. Lograsso, A. R. Ross, and R. McGrath, Phys. Rev. B **72**, (2005).

[31] L. Leung, J. Ledieu, P. Unsworth, T. A. Lograsso, A. R. Ross, and R. McGrath, Surf. Sci. **600**, 4752 (2006).

[32] T. Cai, J. Ledieu, R. McGrath, V. Fournée, T. Lograsso, A. Ross, and P. Thiel, Surf. Sci. **526**, 115 (2003).

[33] K. J. Franke, H. R. Sharma, W. Theis, P. Gille, P. Ebert, and K. H. Rieder, Phys. Rev. Lett. **89**, 156104 (2002).

[34] H. R. Sharma, M. Shimoda, A. R. Ross, T. A. Lograsso, and A. P. Tsai, Physical Review B **72**, (2005).

[35] E. Y. Vedmedenko, H. P. Oepen, and J. Kirschner, Phys. Rev. Lett. **90**, (2003).

[36] P. Schiffer, Nature **420**, 35 (2002).

[37] Y. Weisskopf, M. Erbudak, J. N. Longchamp, and T. Michlmayr, Surf. Sci. **600**, 2594 (2006).

[38] Y. Weisskopf, S. Burkardt, M. Erbudak, and J. N. Longchamp, Surf. Sci. **601**, 544 (2007).

[39] J Smerdon, J Ledieu, J.T. Hoeft, D.E. Reid, L.H. Wearing, R.D. Diehl, T.A. Lograsso, A.R. Ross, and R. McGrath, Phil. Mag. **86**, 841 (2006).

[40] J. A. Smerdon, J. Ledieu, R. McGrath, T. C. Q. Noakes, P. Bailey, M. Draxler, C. F. McConville, T. A. Lograsso, and A. R. Ross, Phys. Rev. B **74**, (2006).

[41] E. Y. Vedmedenko, U. Grimm, and R. Wiesendanger, Phys. Rev. Lett. **93**, (2004).

[42] E. Y. Vedmedenko, Mod. Phys. Lett. B **19**, 1367 (2005).

[43] E. Y. Vedmedenko, U. Grimm, and R. Wiesendanger, Phil. Mag. **86**, 733 (2006).

[44] Y. Weisskopf, R. Lüscher, and M. Erbudak, Surf. Sci. **578**, 35 (2005).

[45] J. B. Campbell, *Introduction to Remote Sensing* (Taylor and Francis, London, 1996).

[46] L Holland, W Steckelmacher, and J Yarwood, *Vacuum Manual* (Spon, London, 1974).

[47] Omicron, *SPA-LEED Instruction Manual Version 1.1* (Omicron, Germany, 1991).

[48] R. A. Laudise, Solid State Physical Electronics Series, Prentice-Hall, Hemel Hempstead .

[49] L Meitner, Zeits. f. Physik **17**, (1922).

[50] L Meitner, Zeits. f. Physik **9**, (1923).

[51] P Auger, Journal De Physique **6**, (1925).

[52] M Prutton, *Introduction to Surface Physics* (Oxford University Press, USA, 1994).

[53] Q Fu and T Wagner, Thin Solid Films 455 (2002).

[54] G. E. Rhead, M. G. Barthes, and C. Argile, Thin Solid Films **82**, 201 (1981).

[55] C. Argile and G. E. Rhead, Surf. Sci. Rep. **10**, 277 (1989).

[56] T. E. Gallon, Surf. Sci. **17**, 486 (1969).

[57] D. C. Jackson, T. E. Gallon, and A. Chambers, Surf. Sci. **36**, 381 (1973).

[58] Q. G Zhu, A. D Zhang, E. D Williams, E Park, and R. L. Park, Surf. Sci. **172**, 433 (1986).

[59] M. G. Barthes and A. Rolland, Thin Solid Films **76**, 45 (1981).

[60] C Davisson and L Germer, Nature **119**, (1927).

[61] C Davisson and L Germer, Phys. Rev. B **119**, 558 (1927).

[62] J. Hudson, *Surface Science* (Butterworth-Heinemann, Stoneham, MA, 1992).

[63] D.P. Woodruff and T.A. Delchar, *Modern Techniques of Surface Science, Second Edition* (Cambrige University Press, Cambridge, 1994).

[64] J Chen, *Introduction to Scanning Tunneling Microscopy* (Oxford University Press, Oxford, 1993).

[65] W. Kaiser, R. Jaklevic, and IBM, J. Res. Dev. **30**, 411 .

[66] Z. M. Stadnik, Mat. Trans. **42**, 920 (2001).

[67] J. Ledieu, R. McGrath, L. Leung, L. Wearing, T. A. Lograsso, A. R. Ross, and V. Fournée, Phys. Rev. B **77**, 073409 (2008).

[68] V. Fournée, T. C. Cai, A. R. Ross, T. A. Lograsso, J. W. Evans, and P. A. Thiel, Phys. Rev. B **67**, (2003).

[69] L. Vitos, A. V. Ruban, H. L. Skriver, and J. Kollar, Surf. Sci. **411**, 186 (1998).

[70] F. Hippert, M. Audier, J.J. Préjean, A. Sulpice, E. Lhotel, V. Simonet, and Y. Calvayrac, Phys. Rev. B **68**, 134402 (2003).

[71] J. A. Stroscio, D. T. Pierce, and R. A. Dragoset, Phys. Rev. Lett. **70**, 3615 (1993).

[72] J. A. Stroscio, D. T. Pierce, M. D. Stiles, A. Zangwill, and L. M. Sander, Phys. Rev. Lett. **75**, 4246 (1995).

[73] R. Gonzalez and R. Woods, (2002).

[74] G. Ehrlich and F.G. Hudda, J. Chem. Phys. **44**, 1039 (1966).

[75] J. Ledieu, A. W. Munz, T. M. Parker, R. McGrath, R. D. Diehl, D. W. Delaney, and T. A. Lograsso, Mat. Res. Soc. Symp. Proc. **553**, 237 (1999).

[76] N. R. Shivaparan, V. Krasemann, V. Shutthanandan, and R. J. Smith, Surf. Sci. **365**, 78 (1996).

[77] G. W. Anderson and P. R. Norton, Surf. Sci. **336**, 262 (1995).

[78] M. Hochstrasser, A. Atrei, B. Bolliger, R. Eismann, M. Erbudak, and D. Pescia, Surf. Rev. Lett. **5**, 1007 (1998).

[79] J. P. Biberian and G. E. Rhead, J. Phys. F: Met. Phys. **3**, 675 (1973).

[80] J. stöhr, Magn. Mat. **200**, 470 (1999).

[81] J. A. Smerdon, *PhD. Thesis. The formation and characterisation of aperiodic ultra-thin films on the surfaces of quaicrystals* (The University of Liverpool, Liverpool, 2006).

[82] L.H. Wearing, J. A. Smerdon, L. Leung, T. A. Lograsso, A. R. Ross, and R. McGrath, Surf. Sci. **601**, 3450 (2007).

[83] T. C. Q. Noakes, P. Bailey, C. F. McConville, C. R. Parkinson, M. Draxler, J. A. Smerdon, J. Ledieu, R. McGrath, A. R. Ross, and T. A. Lograsso, Surf. Sci. **583**, 139 (2005).

[84] T. C. Q. Noakes, P. Bailey, M. Draxler, C. F. McConville, A. R. Ross, T. A. lograsso, L. Leung, J. A. Smerdon, and R. McGrath, J. Phys. Cond. Matt. **18**, 5017 (2006).

[85] A. C. Fisher, *Electrode Dynamics* (Oxford University Press, Oxford, 1996).